THE UNIVERSITY OF CHICAGO

MASTERS OF THEIR OWN FATE: MODELING THE CHEMICAL AND DYNAMIC FEEDBACK MECHANISMS OF PLANET FORMATION

A DISSERTATION SUBMITTED TO
THE FACULTY OF THE DIVISION OF THE PHYSICAL SCIENCES
IN CANDIDACY FOR THE DEGREE OF
DOCTOR OF PHILOSOPHY

DEPARTMENT OF THE GEOPHYSICAL SCIENCES

BY
ERIC ROBERT VAN CLEPPER

CHICAGO, ILLINOIS
AUGUST 2026

ORCID iD: https://orcid.org/0000-0002-5954-6302

“All we have to decide is what to do with the time that is given to us.”

— Gandalf T.A. 3019

TABLE OF CONTENTS

LIST OF FIGURES

LIST OF TABLES

ACKNOWLEDGMENTS

I have many people to thank!

First and foremost, my advisor and mentor Fred Ciesla. Despite the fact that there were many times throughout my PhD that I think neither one of us wanted to be in academia, I'm glad that you were there to guide me through these past 6 years. I am also forever grateful to the rest of my committee: Andy Davis, Leslie Rogers, and Jenny Bergner. You all have helped to shape my research and fuel my curiosity in ways I never could have done otherwise. Finally, a large thank you to all my collaborators – Ted Bergin, Arthur Bosman, and Felipe Alarcón – who have helped fill in the (many) gaps in my knowledge throughout my work.

I also need to thank the entire dogs department but especially all present and former members (officially and unofficially) of the Ciesla group: Megan Barnett, Adina Feinstein, Alya Al-Kibbi, Ashraf Dhahbi, Gijs Mulders, Darryl Seligman, Ellen Price, and Tommy Chi Ho Lau. Academia is a difficult place, but so much easier with friends.

I'd like to thank the maintainers and administrators of the UChicago RCC, without whom these projects quite literally could not have happened. A huge shout out to the maintainers and developers of scientific open source software. I have made use of many different software packages throughout my PhD, but a special acknowledgement should be made to the `numpy` and `matplotlib` teams, who's software I have used almost every day of my grad school career.

And, of course, a very special thank you to my many friends who have supported me and kept me sane throughout this entire process, and their reminders that I am so much more than just a graduate student. To my mom and dad, who have always instilled me a love of science and a desire to learn. And last but not least to my amazing wife, Rachel, who has been by my side through it all. I love you so much.

ABSTRACT

With over 6,000 confirmed exoplanets, numerous high angular resolution protoplanetary disk surveys, and multiple sample return missions from meteorites, the field of planet formation has a wealth of data on different stages of planet formation, yet still no clear pathway to fully connect these data. One of the most striking discoveries of the past decade is the dynamic natures of protoplanetary disks, with evidence of dust growth, drift, and substructures appearing ubiquitous in disks. These substructures include rings, gaps, spiral arms, and azimuthal asymmetries in both the dust and gas emission from the disks, with some such substructures directly linked to the forming planets embedded in the disk. At the same time, isotopic measurements of meteorites and, recently, asteroids, show that parent bodies in our own solar system formed from two spatially distinct reservoirs, that persisted throughout the millions of years of prolonged planetesimal formation.

While this dichotomy has been explained by invoking substructures, it is unclear how these reservoirs might remain separated over the lifetime of the disk while still allowing for some degree of transport of calcium-aluminum-rich inclusions and chondrules. While it is often proposed that ongoing planet formation may affect the remaining solids within a disk through dust growth, fragmentation, stirring, mixing, and pileups, it is not yet clear how the creation of these planet-induced disk substructures influence the composition of the growing planet, nor how they may affect the formation of subsequent planets.

In this thesis, I examine the feedback of planet formation on the protoplanetary disk, and how the composition of both the disk and the planets that grow there influence one another over the disk lifetime. I explore these feedback mechanisms — including planet-induced disk substructures, grain growth and fragmentation, and planetary heating — using a variety of computational techniques to constrain the effects on the composition of embedded planets in self-consistent ways. I compare the results of these computational models with meteorite compositions to place constraints on the Solar Nebula, but also more broadly with detected disks and exoplanets.

First, I present the results of a newly developed chemical model that simultaneously solves the chemical composition of the ice and gas in a protoplanetary disk while accounting for grain growth and ice sequestration. I show that while depleting small grains from the disk by growing larger

pebbles accelerates photon-driven chemistry throughout the disk, the bulk of solids in the midplane retain their inherited composition from the protostellar cloud. As such, early forming solids in the outer disk, including some meteorite parent bodies in our solar system, were impacted by chemical processing during the protoplanetary disk phase less than previously recognized. The new CANDY model (Chemistry ANd DYnamics) is freely available on github[1] and is distributed under an open source MIT License.

Second, I examine the extent of radial mixing in a protoplanetary disk containing a growing giant planet. These results are presented within the context of the observed meteorite isotopic dichotomy, for which it has been proposed that Jupiter acted as a physical barrier between the inner and outer solar nebula, preventing mixing of carbonaceous and non-carbonaceous material. While a massive giant planet is capable of halting the inward drift of large pebbles in the disk, I show that small dust is capable of filtering past the embedded planet, and the efficiency of this passing varies as the planet grows in mass. Further, the planet can affect transport and mixing at more distant regions in the disk. As such, the extent of radial mixing in the solar nebula evolves dramatically over time, varying with time and location, leading to a complex means of exchange across different spatial reservoirs. The particle tracking algorithm used in the model presented in this chapter is also available for download online via github[2].

Finally, I examine how the stirring of small dust by a growing giant planet may act to enrich the atmospheres of the planet with volatile ices after it reached its pebble isolation mass, a point where accretion of solids is expected to stall or significantly slow. As giant planets accrete gas from the disk, they stir small dust to upper layers of the disk where temperatures are higher than the disk midplane. If these small grains are abundant as a result of particle fragmentation outside the disk gap carved by the planet, then this may be a promising mechanism to enrich these atmospheres in carbon, oxygen, and nitrogen, explaining observed enrichments in both Jupiter and directly imaged giant exoplanets.

1. https://github.com/ervc/newcandy

2. https://github.com/ervc/cpartrace

CHAPTER 1
INTRODUCTION

During the 21st century, our understanding of planets and planet formation has drastically changed. Since the first confirmed detections of planets orbiting other stars in the 1990s (A. Wolszczan & D. A. Frail, 1992; M. Mayor & D. Queloz, 1995), the number of known exoplanets has grown to over 6,000 as of 2026[1]. Surprisingly, many of these planets are unlike anything known in our Solar System, including, for example, hot Jupiters, super-Earths, sub-Neptunes, and water worlds. As observational techniques have developed, astronomers have characterized the atmospheres of some of these exoplanets, once again observing a wide variety of atmospheric compositions unlike any planets in our Solar System (see, e.g., N. Madhusudhan, 2019, for recent a review).

Despite these many observations, astronomers have yet to find a truly Earth-like planet, much less an unambiguous signature of life on another planet. The question arises: *What makes Earth unique in its ability to host life and how did the formation of our Solar System shape the composition of the Earth?*

One way to attempt to answer this question is to examine the environment in which these planets form, the protoplanetary disk. By combining cosmochemical knowledge of the Solar System with astronomical data of extra-solar disks, a more cohesive picture of planet formation can be made. In this thesis, I outline novel approaches including a combination of physical and chemical numerical modeling techniques to better understand this planet formation process, directly comparing models of Solar System formation with observations of other disks and the planets within.

1.1 Planet Formation Theory

Planets form within a protoplanetary disk surrounding a young star. Despite the fact that all planets form within these disks, planets can show a wide diversity of sizes, orbits, and compositions; both between different planetary systems and within a single system. Thus, we must look to processes within the protoplanetary disk to understand the nature of the planets forming within. Here, I briefly review the theoretical framework of our current understanding of planet formation, from

1. https://exoplanetarchive.ipac.caltech.edu/

dust and gas to planetesimals and planets.

1.1.1 Disk Physical Evolution

The planet formation processes begins with the formation of the host star. As a star forms form the gravitational collapse of the interstellar medium (ISM), conservation of angular momentum results in the formation of an accretion disk around the young stellar object. This disk is also known as the protoplanetary disk (PPD) as this is the location where planet formation occurs. PPDs have average lifetimes on the order of $\sim 1 - 10$ Myr (K. E. Haisch et al., 2001; E. E. Mamajek et al., 2009). Over this time, solids in the disk grow into planetesimals and planets, while gas is left gravitationally bound to giant planets or is removed from the disk by accreting onto the star or removal to space via photoevaporation and stellar winds (I. Pascucci et al., 2025; B. Tabone et al., 2025).

PPDs initially form from a gas and dust mixture reflecting the ISM composition, about 1% solids by mass. These solids are a combination of small, sub-micron refractory dust grains (J. S. Mathis et al., 1977; T. Birnstiel, 2024) and ice mantles made up of more volatile molecules containing carbon, oxygen, nitrogen, and sulfur (though the exact composition of these ices will depend on the local conditions of the ISM, see, e.g. D. Bockelée-Morvan et al., 2000; A. C. A. Boogert et al., 2015; S. Krijt et al., 2023; M. L. R. Van 'T Hoff et al., 2023). Once in the disk, if the relative velocity between particle collisions is sufficiently low, they may stick together to grow into larger dust conglomerates, or pebbles, and settle to the midplane. The relative velocity between grains typically increases with grain size, setting an upper limit on the size grains can grow to before collisions lead to fragmentation or bouncing (neither fragmentation nor growth) (A. Zsom et al., 2010; T. Birnstiel et al., 2012, e.g.). The exact velocity at which collisions no longer lead to growth will depend on the dust composition (C. Güttler et al., 2010), but typical values of this fragmentation velocity place upper limits on pebble size on the order of mm - cm (J. Drążkowska et al., 2023).

In addition to this limit on solid size due to collisions, dust grains and pebbles are also constantly drifting radially inwards through the disk. This is due to the fact that the surrounding gas is supported radially via gas pressure, leading to a slightly sub-Keplerian orbital velocity. The solids, on the other hand, do not feel this pressure support and orbit at Keplerian velocity. As a result, the dust grains feel a constant headwind from the surrounding gas. This gas drag slows the dust grains and leads to a net radial velocity inwards (S. J. Weidenschilling, 1977). The resulting inward radial velocity is a function of the grain size and pressure gradient of the gas, with radial velocities increasing with grain size up to about cm in size (S. J. Weidenschilling, 1977; T. Takeuchi & D. N. C. Lin, 2002; J. Drążkowska et al., 2023). As a result, even in the absence of the fragmentation barrier discussed previously, the time for grains to drift to the inner edge of the disk is shorter than the timescale needed for further growth. This size where radial drift is more efficient than growth is known as the "drift barrier" and provides another an upper limit on the size to which dust grains may grow (T. Birnstiel et al., 2012).

As a combination of these fragmentation and drift barriers, it is impossible to grow solids past a few cm in size in a typical protoplanetary disk through collisional growth of dust aggregates. There are several proposed solutions to this problem, such as the gravitational instability (A. Toomre, 1964; A. P. Boss, 1997; R. R. Rafikov, 2005), streaming instability (A. N. Youdin & J. Goodman, 2005; A. Johansen et al., 2007), and vortex dust trapping (P. Barge & J. Sommeria, 1995; S. Inaba & P. Barge, 2006). These processes have different mechanisms, but in general allow a large number of small grains to to form a single, larger kilometer-sized planetesimal by locally reducing relative velocities between grains, avoiding the fragmentation limit and skipping over the drift limit.

Another possible solution to overcome the drift barrier is the creation of local pressure maxima. Because the source of radial drift is the gas pressure gradient, inwards drift will halt and dust grains will concentrate in regions of the disk where the disk pressure has a local maxima, also known as a "pressure bump" or "pressure trap" (P. Pinilla et al., 2012; C. P. Dullemond et al., 2018). There are many possible origins of these pressure traps that may lead to either radial or azimuthal concentrations of dust (see recent reviews by J. Bae et al., 2023; T. Birnstiel, 2024). One example is the creation of local pressure maxima due to tidal interactions between the disk and an embedded giant planet. When a planet becomes massive enough it carves a gap in the disk, lowering the disk surface density at the orbital radius of the planet (R. R. Rafikov, 2002). At the edges of this gap, the local pressure gradient becomes zero, trapping dust grains in a dust ring exterior to the planet's orbit (P. Pinilla et al., 2012; C. P. Dullemond et al., 2018). The critical mass for a planet to do this, known as the pebble isolation mass, is $\sim 30 M_{\oplus}$ for typical disk conditions (M. Lambrechts et al., 2014; B. Bitsch et al., 2018). In this way, the formation of a giant planet may trigger subsequent planet formation in the disk by concentrating dust grains in pressure maxima (e.g. L. E. J. Eriksson et al., 2020; D. Carrera et al., 2021; T. C. H. Lau et al., 2022, 2024; H. Zhao et al., 2025).

1.1.2 Disk Chemical Evolution

Protoplanetary disks are chemically active, with temperature and density gradients throughout the disk leading to both gas phase and grain surface reactions. The disk is also subject to interstellar irradiation including cosmic rays, X-rays, and UV photons, which all penetrate different regions of the disk (E. A. Bergin, 2009). The composition of the disk is approximately 99% hydrogen and helium by mass; elements with higher mass than helium are often referred to collectively as metals, with the mass fraction of these heavier elements defining the disk metallicity. The metal composition of the disk is split between refractory species, making up the solid dust grains, and volatile species which may be present as ice mantles on the grain surfaces or in the gas phase depending on local temperature and pressure in the disk.

As a consequence of these differing chemical environments, the volatile composition of the disk's gas and solid phase varies both radially and vertically throughout the disk. Snowlines, for example, are locations in the disk where specific molecules transition between solid to gas. In addition to these phase change reactions, gas and grain surface chemistry can create or destroy more complex macromolecular species, which are not typically found in the ISM (see Figure 3 of K. I. Öberg et al., 2023, and references therin). These different molecules will have unique binding energies to the surface of the grains, creating their own snowlines. As a result, the elemental composition of the refractory solids, volatile ices, and gas may evolve over time as disk chemistry and conditions vary. Because planets form within this disk, it is assumed that their composition should reflect the composition of the disk at which they form (K. I. Öberg et al., 2011).

From this, a simplified model of planet formation can be created, where in solids grow from dust to planetesimals to create planetary cores. These cores may continue to grow and evolve after the disk dispersal to become terrestrial planets, inheriting the composition of the solid planetesimals from which they formed. If these cores grow massive enough to carve a gap in their disk (i.e. the pebble isolation mass), they begin runaway growth (J. B. Pollack et al., 1996) and accrete gas from the disk to form a gas atmosphere. The composition of the solid core and gaseous atmosphere are set by the disk composition at the formation location (K. I. Öberg et al., 2011). Observations of exoplanets, protoplanetary disks, and meteorite records, however, all point to a more complex picture that cannot be explained by this simple story.

1.2 Observed Planet Formation Constraints

1.2.1 Astronomical Observations

By comparing observed spectra of planetary atmospheres with models, the composition of planetary atmospheres can be inferred (e.g. N. Madhusudhan, 2019; T. Currie et al., 2023). Such techniques provide powerful insights to the composition of other planets, allowing for large scale surveys of planetary oxidation states, metallicities, and the potential for life-relevant molecular tracers (JWST Transiting Exoplanet Community Early Release Science Team et al., 2023; E. Nasedkin et al., 2024; Y. Chachan et al., 2025). While planet formation theory suggests that the atmospheres of these planets should reflect the composition of the gaseous disk, recent observations point to an increased metallicity in giant planets relative to what is expected in the disk where they form (C.-C. Hsu et al., 2024; E. Nasedkin et al., 2024; E. A. Bergin et al., 2024; W. O. Balmer et al., 2025; J. D. Lothringer et al., 2025). Similar to giant exoplanets, measurements of Jupiter's atmosphere taken during the Juno mission revealed an excess of volatile metals (carbon, oxygen, and nitrogen) relative to the Sun, pointing to a similarly elevated metallicity in our solar system as in other extrasolar systems (S. K. Atreya et al., 2020; C. Li et al., 2020).

Exoplanet observations can tell us about these planets today, but they have evolved over millions to billions of years. As a result, observed compositions may be altered by later planetary evolution, such as exchange with the planet mantle or atmospheric chemistry and loss. Given this planetary evolution, how can we connect planets' current day composition with the environments in which they formed? One method is to observe protoplanetary disks themselves. A major recent advancement in the observations of disks came in 2015 when the Atacama large millimeter/submillimeter array first observed the HL tau disk at high resolution (ALMA Partnership et al., 2015). For the first time, the disk structure was resolved showing distinct rings and gaps in the distribution of solid dust. In the follow up DSHARP survey (Disk Substructure at High Angular Resolution Project),

S. M. Andrews et al. (2018) showed that many different types of substructures – rings, gaps, spirals, and asymmetries – are not only present, but common in disks surveyed.

In addition to observations of the dust continuum (thermal emission from solid grains), ALMA can also observe molecular line emission, enabling observers to determine the molecular composition of the gas in disks. The MAPS survey (Molecules with ALMA at Planet-forming Scales, K. I. Öberg et al., 2021) showed that in addition to substructures in the dust, gaseous molecules showed similar variety of rings, gaps, and asymmetries. Interestingly, while both the dust continuum and molecular emission show ring and gap substructures in some disks, these do not necessarily align with one another (C. J. Law et al., 2021) pointing to a complex interplay between the chemical emission and solid dynamics.

The origin of these substructures may, in some cases, be the result of ongoing giant planet formation. As discussed earlier, giant planets can carve a gap in the disk, concentrating dust into an outer ring and creating a gap at the orbit of the planet. These giant planets also create large scale gas velocity perturbations, both in the accretion flows onto the planet and within the planet-induced spiral arms in the disk (W. Kley, 1999; W. Kley et al., 2001, see Section 1.3 for further discussion of these planet-induced gas kinematics). In these cases, the doppler shift of specific molecular tracers can be used to detect velocity perturbations in the gas as a result of gravitational interactions with the embedded planet. While these signatures have not been found in all gaps seen by ALMA, they have been used to confirm the presence of embedded giant planets in some disks (C. Pinte et al., 2018; R. Teague et al., 2019), with the recent exoALMA survey probing for further kinematic signals in molecular line emission (R. Teague et al., 2025).

While ALMA has been revolutionary for the understanding of disk structure, substructure, and composition, the spatial resolution of even the highest resolution surveys is limited to about 10 au (S. M. Andrews et al., 2018; K. I. Öberg et al., 2021; R. Teague et al., 2025). This means that observations of disk structure and composition using ALMA are limited to large-scale structures in the outer disk. While this is in part a technical limitation on angular resolution, the inner disk is also much hotter, and thus primarily emits in infrared wavelengths, rather than the millimeter and sub-millimeter observed with ALMA. To resolve the composition and structure of the inner disk, where terrestrial planet formation is thought to occur, instruments will not only need higher resolution, but also to observe in the shorter infrared wavelengths.

Fortunately, the recently launched James Webb Space Telescope (JWST) is equipped to observe in the near-infrared, allowing for the measurement of emission and absorption spectra from the inner regions of these disks. Although spatial resolution is still limited, spectroscopy of the inner disk allows for characterization of both the gas in the inner disk and the composition of the ice and grains themselves (see, e.g., J. B. Bergner et al., 2026). These observations have revealed that some disks show warm and hot water emission from the inner disk (G. Perotti et al., 2023). Interestingly, this water emission appears to correlate with large scale substructures observed with ALMA, pointing to a connection between disk structure, dynamics, and composition (A. Banzatti et al., 2025). By combining observations across wavelengths and spatial scales, we can begin to connect these observational snapshots of disks with models of planet formation to form a more cohesive picture of planet formation.

1.2.2 Solar System Observations

In addition to observing PPDs, which can provide insight into planet formation around other stars, meteorites provide clues to the formation of our own solar system. Meteorites and their parent bodies, asteroids, are the remains of planetesimals formed in the first few million years of our Solar System (A. Krot et al., 2009; J. N. Connelly et al., 2012; M. Bizzarro et al., 2025). By analyzing these remnants of the early Solar System, we can infer the conditions of the beginning of our own protoplanetary disk.

Meteorites can be split into two broad categories, chondrites and achondrites, which come from undifferentiated and partially or fully differentiated parent bodies respectively. The undifferentiated chondrites are made up of a combination of chondrules, refractory inclusions, and matrix, each of which reflect the composition of the disk in the time and place in which they individually formed. Refractory inclusions, such as calcium-aluminum-rich inclusions (CAIs), are believed to be the first solids to solidify in our Solar System, setting the "Time Zero" of the Solar System (A. Davis & F. Richter, 2007; J. N. Connelly et al., 2012; G. MacPherson et al., 2012). Chondrules, small silicate-rich spherules, and meteorite parent bodies then formed 2-4 Myr after the first CAIs condensed (R. H. Hewins et al., 2005; J. N. Connelly et al., 2012; A. M. Davis, 2022).

The composition of these different meteorite components – their isotopic ratios, mineralogy, and bulk elemental composition – can inform us as to the condition in the disk when and where these different components formed. One striking difference that has been observed is in oxygen isotopic ratios between CAIs, bulk meteorites, and hydrated minerals in chondrules (K. D. McKeegan et al., 2011, and references therein). While bulk meteorites tend to have oxygen isotopic ratios within $\pm 10‰$ of Earth, CAIs are depleted in heavier ^{17}O and ^{18}O relative to ^{16}O by up to $60‰$. Hydrated minerals, on the other hand, can be enriched in isotopically heavy oxygen by up to $180‰$ (N. Sakamoto et al., 2007). This indicates a wide range of oxygen isotopic signatures throughout the disk and points to an active chemical environment in the disk and, likely, pre-solar cloud to create these distinct isotopic signatures (R. N. Clayton, 2002; H. Yurimoto & K. Kuramoto, 2004; J. R. Lyons & E. D. Young, 2005; J.-E. Lee et al., 2008; A. N. Krot et al., 2010).

In addition to the isotopic variations in oxygen observed between CAIs, chondrules, and included water, measurements of isotopic ratios of various refractory isotopes have revealed two distinct trends, with carbonaceous meteorites (CC) showing a distinct excess in r-process isotopes relative to the non-carbonaceous meteorites (NC) (P. H. Warren, 2011; G. Budde et al., 2016). Given this difference between meteorite types is nucleosynthetic in origin, and thus cannot be explained by disk chemistry, it is suggested that this isotopic dichotomy is the result of a difference in the composition of infalling material to the disk (J. A. Nanne et al., 2019; G. A. Brennecka et al., 2020). The nebular gas was then preserved as distinct spatial reservoirs with different compositions a result of Jupiter's formation creating a gap in the disk, with NC material in the inner disk and CC material in the outer disk (T. S. Kruijer et al., 2017, 2020). It was only after these meteorite parent bodies had formed and the dispersal of the gaseous disk that gravitational interactions with the gas giant planets mixed these two populations together, implanting CC parent bodies interior to Jupiter's orbit along side the NC parent bodies in the current day asteroid belt (K. J. Walsh et al., 2012; S. N. Raymond & A. Izidoro, 2017).

This dichotomy between meteorite parent bodies points to a long-lived separation between spatial reservoirs in the early solar nebula. Because achondrite parent bodies were differentiated, it is believed that they must have formed early while ^{26}Al, a short-lived radioactive isotope, was still present in the solar nebula to act as a heat source for differentiation (T. S. Kruijer et al., 2014;

A. M. Davis, 2022). Despite this early formation, within ∼1 Myr after CAI formation (T. S. Kruijer et al., 2014), show the same nucleosynthetic isotopic dichotomy as chondrites which formed much later, 2-4 Myr after CAIs (N. T. Kita & T. Ushikubo, 2012; T. S. Kruijer et al., 2017).

Despite this long lived and apparently early separation, there is also evidence for widespread mixing in the early solar nebula. Given their high condensation temperature, CAIs are inferred to have condensed near the young sun in the inner disk (G. J. MacPherson et al., 2005). Despite this, CAIs are predominantly found in CC parent bodies (e.g., E. T. Dunham et al., 2023), which are thought to have formed in the outer disk due to their elevated water and volatile content (T. Kleine et al., 2020). This fact points to wide spread outward transport of CAIs early in the disk's lifetime, from their condensation location near the protosun to the outer disk, into the CC reservoir including cometary parent bodies (M. E. Zolensky et al., 2006; F. J. Ciesla, 2007; L. Yang & F. J. Ciesla, 2012).

In addition to this early transport of CAIs in the solar nebula, individual inclusions also appear to have crossed the NC/CC boundary. While CAIs are primarily found in outer disk CC parent bodies, some smaller CAIs have also been discovered in NC chondrites (e.g. A. Bischoff & K. Keil, 1983; R. W. Hinton & A. Bischoff, 1984; T. Haugbølle et al., 2019; E. T. Dunham et al., 2023). This may be explained by a pileup of CAIs in the outer disk with selective filtering of the smaller grains (T. Haugbølle et al., 2019, and discussed in Chapter 3). Conversely, there has also been evidence for NC-like chondrules in CC parent bodies (D. L. Schrader et al., 2020; E. Van Kooten et al., 2021; D. L. Schrader & J. Davidson, 2022). Together, these inclusions point to some degree of mixing in the solar nebula including mixing both inwards and outwards across the NC/CC barrier.

1.3 Planet Formation Models

Computational models can be used to predict the evolution of both the chemistry and dynamics of disks over their lifetime, connecting these theories of planet formation to the observations of planets, disks, and meteorites today.

One common way of simulating PPD evolution is with the use of hydrodynamic simulations. Where simple, axisymmetric disks can be described analytically (D. Lynden-Bell & J. E. Pringle, 1974), the formation of a planet inherently breaks this symmetry, relying on numeric simulations

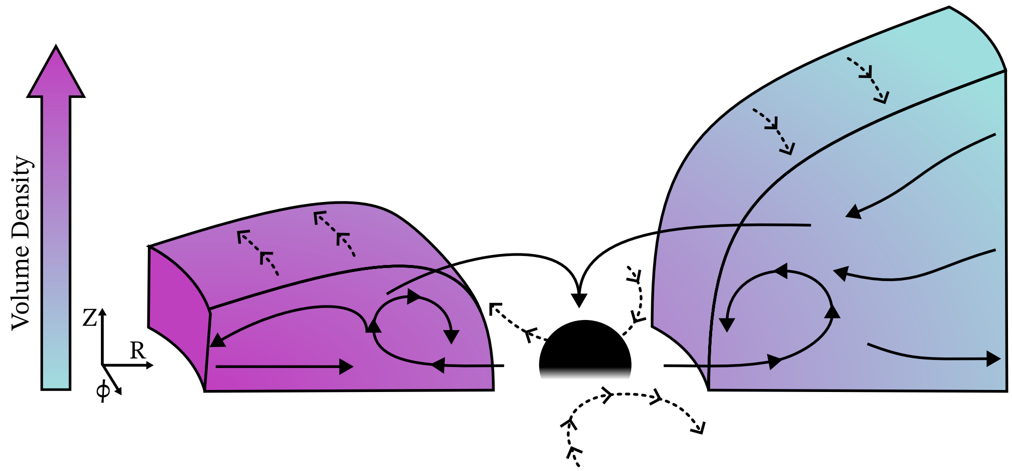

Figure 1.1: Cartoon slice of a protoplanetary disk showing three-dimensional gas advection around an embedded giant planet. Solid lines demonstrate typical gas advection patterns in the $R-Z$ plane, with meridional flows driving gas away from the planet at the midplane and vertically upwards. Gas tends to be accreted onto the planet from higher elevations near the poles of the planet. Dashed arrows show the azimuthal rotation of the gas relative to the planet, with horseshoe filtering flows passing the planet. Gas flows are simplified from E. R. Van Clepper et al. (2025b).

to analyze planet-disk interactions. While 1D (radial) numerical simulations can approximate the depth and width of the gap formed around a planet (T. Takeuchi et al., 1996), 2D ($R-\phi$) simulations reveal that planets can not only carve a gap in the disk, but also create global spiral arms (W. Kley, 1999; J. Bae & Z. Zhu, 2018) and vortices at the gap edges (M. De Val-Borro et al., 2007). In 3D simulations, planets create meridional flows in the disk, driving gas advection vertically away from the midplane near the planet as shown in Figure 1.1 (W. Kley et al., 2001; A. Morbidelli et al., 2014; J. Szulágyi et al., 2014; E. Lega et al., 2024). Each of these dynamic effects of planet growth can feedback onto dust transport and growth throughout the disk as local changes in disk density and velocity affect dust aerodynamics.

One finding of these higher dimensional models is the prevalence of "filtering" of small dust through gaps created by giant planets (P. Weber et al., 2018; T. Haugbølle et al., 2019; S. M. Stammler et al., 2023). While filtering has been characterized in 2D models, it is still unclear to what extent the 3D meridional flows might facilitate, or hinder, this filtering effect. Recent observations have provided some evidence that filtering may indeed be common in disks, with some dust traps being "leaky" rather than hard barriers to inward drift (A. Banzatti et al., 2025; N. T. Kurtovic et al., 2025; A. Sierra et al., 2025). Despite these observations, a theoretical modeling framework to characterize this leakiness remains elusive (A. Houge et al., 2026). In addition to filtering, planets also vertically stir both gas and dust away from the midplane (J. Bi et al., 2021). This not only lofts grains to higher temperature regions where ice may sublimate, but feeds back on temperature and irradiation structure of the disk as this dust is the primary source of opacity in the disk.

These dynamic models are often complimented by chemical models, which typically solve a network of astrochemical rate equations to determine the evolution of molecular abundances over the lifetime of the disk. While observations can be used to determine the molecular composition at the surface of disks and cosmochemical measurements of meteorites reveal the composition of solids at the midplane, chemical models must be used to connect these two reservoirs and show how they change over the lifetime of the disk. Disk chemical models must consider not only the evolving temperature and density structure, but also UV, X-ray, and cosmic ray radiation fields (see K. I. Öberg et al., 2023, for a recent review). All of these factors can drastically affect the composition of the disk with UV and temperature particularly sensitive to the dust distribution in the disk.

This is because small dust can act as the primary source of opacity in the disk, limiting the optical depth of UV-photons to the surface. As a result, a disk where solids are mostly settled near the midplane will have much deeper penetration of UV-photons and thus a higher proportion of photo-processed material in the gas than a disk with solids distributed vertically away from the midplane. Additionally, as discussed previously, dust grains contain an ice mantle and drift radially through the disk. As they do so, they cross snowlines in the disk, sublimating ice phase volatiles into the gas (J. N. Cuzzi & K. J. Zahnle, 2004; R. A. Booth & J. D. Ilee, 2019; K. Zhang et al., 2020). This ice may otherwise be sequestered into larger pebbles, as dust grains grow and settle, removing oxygen-rich ice from the upper layers of the disk (S. Krijt et al., 2018).

Given the connection between disk chemistry and structure, and the dramatic effects planet formation has on the structure of the disk, it is a natural question to ask: *How does the chemistry of the disk respond to planet formation?*. Dust growth, settling, transport, and stirring all feedback into the local environment and composition of the disk. Despite this, chemical and dynamic models are often handled separately. Typical chemical models assume a constant disk structure over 1 Myr, although some chemical models may include vertical mixing and radial diffusion (Y. Aikawa & E.

Herbst, 2001; D. Semenov & D. Wiebe, 2011; K. Furuya & Y. Aikawa, 2014). Dust transport, in particular, can have important feedback effects on the gas composition, through settling and ice sequestration in addition to pebble drift and sublimation across snowlines (as discussed previously). Recently, models have begun to include temperature effects from an accreting embedded planet (F. Alarcón et al., 2020; F. Alarcón & E. A. Bergin, 2024; H. J. Petrovic et al., 2024; A. Krieger et al., 2025; A. J. Cridland et al., 2025), however these often assume a constant temperature structure and may or may not include dust transport. A self-consistent handling of the chemistry and dynamics as a consequence of planet growth has yet to be modeled.

1.3.1 A Holistic View of Planet Formation

Putting together theoretical models of planet formation with constraints from both astronomical and cosmochemical observations allows for a fully comprehensive model of planet formation, placing our Solar System in the context of planet formation broadly. From astronomical observations, we know that disks have active chemistry, with chemical observations showing ice and gas compositions differing based on location and over the disk lifetime. These observations have also shown that dust substructures, including rings and gaps, are common, and some may indicate ongoing giant planet formation.

While astronomical observations can inform gas phase composition and large scale disk structures, meteoritic measurements tell us about the timing of planet formation and the degree of mixing and processing in planetesimals. Detailed isotopic analysis of meteorites have revealed a seemingly contradictory picture, where CAIs and chondrules appear to have mixed through the solar nebula despite, on the whole, meteorites appearing to have formed in spatially distinct reservoirs over the lifetime of the disk.

Combining these constraints allows for a more complete picture of planet formation, accounting for both the evolving disk, ongoing planet formation, and how these may feedback on each other. Planets reflect the composition of the disk when and where they form, but the act of planet growth fundamentally changes this disk composition. In order to connect planetary compositions back to their formation history in the disk, the evolving chemistry of the disk, including feedback from planet formation, must be accounted for.

1.4 Chapter Summaries

Given the overarching goal of connecting planet formation observations to evolved planetary systems, the complicated relationship between chemistry and dynamics must be considered in a self-consistent manner. In this thesis, I lay out my work connecting the physics and chemistry of disks and how they are both affected by and feed back onto forming planets.

In Chapter 2, I describe a novel approach to coupled physical and chemical modeling using a newly developed software, `CANDY`. Using this approach I examine the feedback of dust growth and settling with UV-photon driven chemistry in the surface of the disk. I show that through a combination of both physical sequestering and chemical destruction, gaseous CO abundances may be lowered by 1-2 orders of magnitude, consistent with disk observations. The work in this chapter is published in E. R. Van Clepper et al. (2022).

In Chapter 3, I present results of 3D Monte Carlo particle tracking simulations in the context of the proposed role of Jupiter to physically separate the inner and outer NC and CC reservoirs. I show that as a giant planet grows its 3D gas advection can actually increase the degree of mixing for small solids, challenging the assumption that Jupiter acted as a barrier of distinct isotopic reservoirs. This work is published in E. R. Van Clepper et al. (2025b).

In Chapter 4, the 3D stirring of these small dust grains is explored in more detail, accounting for heating from the embedded planet and central star. I show that as grains are lofted in the planet-induced meridional flows, they are exposed to increased temperatures, processing ice present on grain surfaces. If this ice sublimates, it may be accreted into the atmosphere of the giant planet, increasing the volatile content of the giant planet atmosphere. I call this effect the dust recycling and icy volatile enhancement (DRIVE) effect, which may explain enhanced metallicities in observed giant planets. The results in this chapter have been published in E. R. Van Clepper et al. (2025a).

In Chapter 5, I summarize these results and argue for a more holistic view of planet formation, accounting for the ongoing evolution of the physics and chemistry within PPDs and how these influence on another. I briefly discuss future work and implications for the ice processing in leaky dust traps around giant planets.

CHAPTER 2

CHEMICAL FEEDBACK OF PEBBLE GROWTH USING CANDY: IMPACTS ON CO DEPLETION AND C/O RATIOS

This chapter has been published as the following:

Van Clepper, E., Bergner, J. B., Bosman A. D., Bergin, E., & Ciesla, F. J. 2022, "Chemical Feedback of Pebble Growth: Impacts on CO depletion and C/O ratios", *The Astrophysical Journal*, **927**, 206, doi: 10.3847/1538-4357/ac511b.

2.1 Chapter Abstract

Observations of protoplanetary disks have revealed them to be complex and dynamic, with vertical and radial transport of gas and dust occurring simultaneously with chemistry and planet formation. Previous models of protoplanetary disks focused primarily on chemical evolution of gas and dust in a static disk, or dynamical evolution of solids in a chemically passive disk. In this paper, we present a new 1D Chemistry ANd DYnamics (CANDY) model for modelling pebble growth and chemistry simultaneously. Gas and small dust particles are allowed to diffuse vertically, connecting chemistry at all elevations of the disk. Pebbles are assumed to form from the dust present around the midplane, inheriting the composition of ices at this location. We present the results of this CANDY model after 1 Myr of disk evolution around a $1M_{\odot}$ star at various locations both inside and outside of the CO snowline. We find that for a turbulent disk ($\alpha = 10^{-3}$), CO is depleted from the surface layers of the disk by roughly 1-2 orders of magnitude, consistent with observations of protoplanetary disks. This is achieved by a combination of ice sequestration and decreasing UV opacity, both driven by pebble growth. Further, we find the selective removal of ice species via pebble growth and sequestration can increase gas phase C/O ratios to values of approximately unity. However, our model is unable to produce C/O values of ∼1.5-2.0 inferred from protoplanetary disk observations, implying selective sequestration of ice is not sufficient to explain C/O ratios > 1.

2.2 Introduction

Planets form in the cold, dense midplanes of accretion disks around nascent stars. Recent observations of protoplanetary disks have provided a wealth of constraints on the physical and chemical processes associated with planet formation. Interferometric observatories, such as the Atacama Large Millimeter/submillimeter Array (ALMA), have probed the chemical compositions of the gaseous disks (K. I. Öberg et al., 2021) and physical structures of the small dust (S. M. Andrews et al., 2018) at high angular resolution. Such observations have revealed that the chemical inventories in disks are markedly different from those seen in molecular clouds, indicating significant processing in the solids and gas that eventually are incorporated into planets. Notably, the CO abundance observed across protoplanetary disks is consistently found to be a factor of 10–100 lower than the canonical interstellar medium (ISM) value of $\sim 10^{-4}$ (C. Favre et al., 2013; K. R. Schwarz et al., 2016; A. Miotello et al., 2017; K. Zhang et al., 2019, 2021). Additionally, the bright emission of hydrocarbons in disks points to significantly elevated gas-phase C/O ratios (>1) compared to the interstellar value ($\sim$0.4; E. A. Bergin, 2016; L. I. Cleeves et al., 2018; A. Miotello et al., 2019; A. D. Bosman et al., 2021a). Understanding the origin of these chemical patterns is critical to understanding what sets compositions of incipient planetesimals and planets that are forming in these disks.

Protoplanetary disks are dynamic objects, within which a variety of chemical and physical processes are at work to transform the raw materials inherited from molecular clouds into the building blocks of planets. The process of planet formation begins with the coagulation of dust grains, and their subsequent redistribution throughout the disk via settling and radial drift. This leads to constantly changing physical conditions within the disk (e.g. density, temperature, UV fields), which in turn drives an evolving disk volatile chemistry (e.g. J. B. Bergner et al., 2020). Thus, planet forming environments are characterized by co-evolving dynamics, physics, and chemistry.

Various models have attempted to explain the low observed CO abundances in disks, generally invoking either physical or chemical processes. Physical models of CO removal consider sequestration of CO ice around the midplane: as small dust grains grow into larger pebbles, they settle to the midplane and trap the ice reservoirs in larger bodies (M. Kama et al., 2016; S. Krijt et al., 2020).

Such models can explain a factor of ∼10 decrease in the gas-phase CO abundance over ∼3 Myr timescales. Chemical models of CO removal account for the processing of CO into larger, less volatile organics in the photon-dominated and warm molecular layers of the upper disk (L. Reboussin et al., 2015; C. Eistrup et al., 2017; K. R. Schwarz et al., 2018). These models can also achieve a factor of 10 depletion in CO for high cosmic ray ionization rates, but only in cold disk models. In both cases, the depletion levels are on the low end of what is observed in disks, and on longer timescales (∼3 Myr) than suggested by observations (∼0.5–1 Myr J. B. Bergner et al., 2020; K. Zhang et al., 2020). As considering dynamics and chemistry independently cannot reproduce observations, more recent models have considered the combined effects, though so far only in simplified ways due to the computational demand of such efforts. For instance, S. Krijt et al. (2020) explored CO depletion in a dynamic disk with a simplified chemistry of CO hydrogenation on grains.

Chemical and dynamical effects may also be responsible for producing high gas phase C/O ratios within a protoplanetary disk. To achieve high C/O ratios in the gas via chemistry alone requires C to be incorporated into volatile, gaseous species while O is incorporated into solids. Correspondingly, selective sequestration of oxygen bearing ices (e.g. H_2O) via pebble growth and settling has been invoked as a means of producing a carbon-rich gas (E. A. Bergin, 2016; K. Zhang et al., 2020; A. D. Bosman et al., 2021b). In this scheme, chemical destruction of CO is followed by formation and sequestration of H_2O, leading to an excess of carbon in the gas over the starting value. Alternate sources of carbon exist, such as photoablation of small carbonaceous grains (e.g. J.-E. Lee et al., 2010; D. E. Anderson et al., 2017; A. D. Bosman et al., 2021a); but these also rely on the presence of UV photons to power the chemistry. Thus, pebble growth and chemical processing may both be necessary to reach high C/O ratios.

To date, few models have explored the detailed feedback that exists between pebble growth and chemistry in protoplanetary disks. D. Semenov & D. Wiebe (2011), K. Furuya et al. (2013), and K. Furuya & Y. Aikawa (2014), have studied chemistry in a turbulent disk, but not including dust dynamics. R. A. Booth & J. D. Ilee (2019) combined chemistry with pebble dynamics, but focusing only on the radial movement of large pebbles at the midplane. However, the growth of pebbles and removal of small dust will have an effect on chemistry throughout the entire column of the disk. Because small dust is the primary source of UV opacity, its removal leads to greater penetration of UV radiation in the disk, initiating photochemical reactions deeper in the disk. Thus, as grain growth proceeds, the removal of ices and the increasing UV penetration will lead to changing physical conditions and initiation of new chemical pathways throughout a vertical column of the disk over time.

In this paper, we present a new model including a full chemical network along with pebble growth and ice sequestration, within a 1D vertical slice of a protoplanetary disk. We call this the Chemistry ANd DYnamics (CANDY) model. With CANDY, we explore the feedback of small dust removal and ice sequestration on gas phase chemistry as these processes occur concurrently. Here, we focus on the effects of the coupled chemistry and dynamics on CO depletion and elevated C/O ratios. Previous studies have linked these features of protoplanetary disks to both chemical processing and dust evolution, and recent observations have shown that these outcomes are robust across protoplanetary disks (A. D. Bosman et al., 2021b; K. Zhang et al., 2019). In Section 2.3 we describe the disk structure and model details used for this paper, and compare the results of our new model with static and diffusive disk models in Section 2.4. Sections 2.5 and 2.6 examine the effects of pebble growth on CO depletion and C/O ratios respectively. Finally, a discussion of our results in Section 2.7 compares our findings to those from previous modeling efforts, and describes how these results should be used to interpret disk observations.

2.3 Methods

Fig. 2.1 illustrates the physical processes investigated in our model. We begin with a vertical column of the disk, in which fine dust is well-mixed with the gas at all heights (Fig 2.1, left). Chemistry occurs at all elevations as determined by the local conditions: the temperature, density, and local UV flux. Dust and gas is able to diffuse throughout the column, being exposed to the different conditions in the column, rather than staying fixed in place (Fig 2.1, middle). Pebbles are created around the disk midplane via coagulation of the dust (Fig 2.1, right). The creation of the pebbles removes dust from this region of the disk, which is then resupplied by diffusion from the upper layers. As pebbles are created, the abundance of dust in the column decreases, allowing ambient radiation to penetrate deeper into the disk over time.

In this section, we describe in detail the various components of this framework and how they are

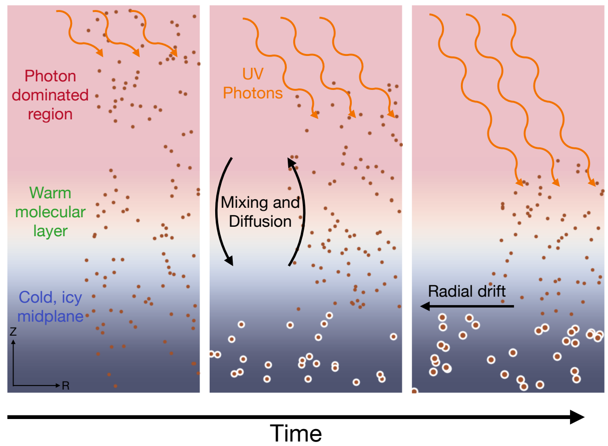

Figure 2.1: A cartoon diagram showing some of the feedback mechanisms between pebble growth and gas phase chemistry. Early in the disk lifetime (left), small dust is well coupled with the gas at all elevations throughout a vertical slice of the protoplanetary disk. UV radiation penetrates into the uppermost layers of the disk in the PDL, but are attenuated by the small dust. At later stages (middle), small dust has begun to form into larger pebbles. These pebbles inherit the icy composition of the dust from which they form. As pebbles form, dust grains settle towards the midplane, allowing radiation to penetrate deeper into the disk. As the disk continues to age (right) pebbles drift out of the vertical column considered, taking any frozen ice with them. This acts to selectively remove ice phase species from the column, and combined with increased UV radiation can significantly alter the chemistry in the disk.

treated in CANDY. We begin by describing the physical environment within which the processes are considered to operate. We then describe how we treat the dynamical evolution of the gas and dust, and the assumptions made around the growth of pebbles. We then outline the chemical model and network used in this study. Finally, we describe how the various components are integrated to evaluate the chemical evolution that occurs within the described framework.

2.3.1 Disk Structure

Because our model is 1D, we explore how these processes work across the disk by modeling vertical slices at various disk radii. We define a disk structure that is similar to S. Krijt et al. (2018) for a disk around a 1 $M_\odot$ star. The radial surface density is given by

$$\Sigma_g(r) = \Sigma_c \left(\frac{r}{r_c}\right)^{-p} \exp\left[-\left(\frac{r}{r_c}\right)^{2-p}\right], \tag{2.1}$$

normalized such that

$$\Sigma_c = (2-p)\frac{M_{\rm disk}}{2\pi r_c^2}. \tag{2.2}$$

For our model, we choose $M_{\rm disk} = 0.05 M_\odot$, $p = 1$, and $r_c = 100$ au. The midplane temperature follows the power law:

$$T_{\rm mid}(r) = 130\left(\frac{r}{\rm au}\right)^{-1/2}\,{\rm K}. \tag{2.3}$$

At any given distance from the star, r, the vertical density distribution is given by:

$$\rho_g(r,z) = \frac{\Sigma_g(r)}{\sqrt{2\pi}H}\exp\left[-\frac{1}{2}\left(\frac{z}{H}\right)^2\right], \tag{2.4}$$

where z is the height above the disk midplane, $H = c_s/\Omega$ is the scale height of the gas and

$$c_s = \sqrt{\frac{k_B T_{\rm mid}(r)}{\mu m_H}} \tag{2.5}$$

is the sound speed for a given midplane temperature, $T_{\rm mid}$ with a mean molecular weight $\mu = 2.3$, $\Omega = \sqrt{GM_\odot/r^3}$ is the Keplerian orbital frequency and k_B is the Boltzmann constant.

The surface layers (higher altitudes) of the disk are directly heated by radiation from the star, and thus reach higher temperatures than the midplane, which is only heated by reprocessed radiation. To describe this structure, we follow E. Dartois et al. (2003) and set the temperature in the surface layers as twice that of the midplane. That is:

$$T(r,z) = T_{\rm atm}(r) = 2T_{\rm mid}(r). \tag{2.6}$$

above a height $z = z_q H$. Below this height, the temperature is given by:

$$T(r,z) = T_{\rm mid}(r)\left(1 + \left[\sin\frac{\pi z}{2 z_q H}\right]^{2\delta}\right), \tag{2.7}$$

where $\Delta T(r) = T_{\rm atm}(r) - T_{\rm mid}(r)$ and we choose $z_q = 3$ and $\delta = 2$. The temperature and density structure for a column located at $r = 30$ au is shown in Figure 2.2.

We also assume that the disk is exposed to an external UV radiation field. As described above,

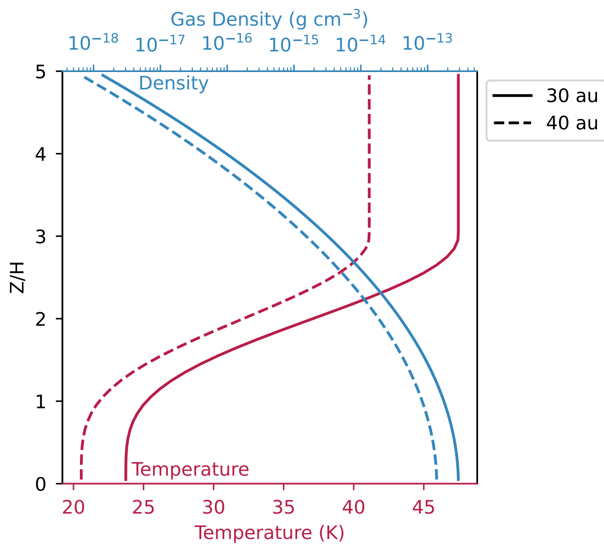

Figure 2.2: Temperature and density structure of the considered disk at 30 and 40 au. CO begins to freeze out at 21 K, so the midplane CO snowline lies between these two radii.

the depth of UV penetration is controlled by the dust abundance. The optical depth into the disk at each location in the column, $\tau_{UV}(z)$, is found via numerical integration:

$$\tau_{UV}(z) = \int_z^\infty \epsilon(z')\kappa_d\rho_g(z')\ \mathrm{d}z' \tag{2.8}$$

where $\epsilon(z)$ is the local small dust-to-gas mass ratio and the dust opacity is picked to be $\kappa_d = 10^5\ \mathrm{cm}^2\ \mathrm{g}^{-1}$ to agree with the extinction-column density relationship of Y. Aikawa & E. Herbst (2001). Here, the UV optical depth is assumed to be dominated by extinction from the small dust, with the gas opacity $\kappa_g \approx 0$ such that $\kappa_{tot} \approx \epsilon\kappa_d$.

Likewise, we determine the column density of CO above each given vertical height by integrating the abundance of the molecule relative to the number density of hydrogen $X(\mathrm{CO}, z) = n_{\mathrm{CO}}(z)/n_H(z)$, where $n_H(z) = 2\rho_g(z)/\mu m_H$

$$N_{\mathrm{CO}}(z) = \int_z^\infty X(\mathrm{CO}, z')n_H(z')\ \mathrm{d}z'. \tag{2.9}$$

A similar methodology is used to determine the column abundance of H_2 above a given location. These column densities are used to account for self-shielding by these molecules, as discussed in

Section 2.3.4.

While we allow the dust and UV vertical profile to evolve over time, the temperature and density structure remain fixed throughout our simulation, following S. Krijt et al. (2020). In future implementations of this model, we will include evolving density and temperature structures with the evolving UV radiation.

2.3.2 Turbulence and Diffusion

While the temperature and density structures remain constant throughout our simulations, we assume that materials are able to diffuse due to the presence of some background turbulence. We define the diffusivity of the gas as $D = \alpha c_s H$, and take it to be constant throughout the slice of the disk, with c_s evaluated at the midplane. The value of α in disks is uncertain; we assume a value of α=10^{-3} for our fiducial case, but also investigate other values as described in Section 2.5.

For a chemical species mixed within the gas and abundance, X_i, the vertical transport of that species is given by:

$$\frac{\partial X_i}{\partial t} = \frac{1}{\rho_g}\frac{\partial}{\partial z}\left(\rho_g D_i \frac{\partial X_i}{\partial z}\right) \tag{2.10}$$

for all species considered (S. Krijt et al., 2018).

Although settling of dust is not directly considered, dust (and ice) species are removed near the midplane in pebble growth. As a result, there is a net downward diffusive transport of dust and ice, effectively leading to dust settling in the column. The net effect is a reduction in fine dust in the upper layers and a concentration of solid mass in pebbles at the midplane.

2.3.3 Dust Growth and Pebble Formation

The solids in our model consist of two populations as in T. Birnstiel et al. (2012): small grains that are coupled to the gas and larger pebbles that decouple and are removed from our simulation after they form. The small grains interact with the gas, serving as sites for freeze-out and chemistry as well as being a source of gaseous species as they desorb from grain surfaces. The small grains are assumed to have radii $s = 0.1\mu$m and are initially present at a dust-to-gas mass ratio, ϵ, of 10^{-2}

everywhere in the column. We set the initial abundance of grains, $X(\text{grain}) = 2.2 \times 10^{-12}$ following A. D. Bosman et al. (2018), setting a material density of $\rho_\text{m} = 1.81$ g cm^{-3}. The small sizes and low densities imply that these grains are fully coupled to the gas and thus their abundance over time is described by Eq. 2.10, with the same diffusivity.

Pebbles form from the small dust grains via collisional growth. In detail, this would result from incremental growth of monomers and smaller aggregates over time. Rather than investigating this computationally intensive process here, we follow S. Krijt et al. (2020) by defining a timescale for pebble formation motivated by previous detailed studies of the process (e.g. T. Birnstiel et al., 2012):

$$\tau_\text{grow} = a\frac{1}{\Omega\epsilon} \tag{2.11}$$

where a is a scaling factor of order unity. This is used to define a loss of dust in a given cell to pebble formation that is described by:

$$\frac{\partial\epsilon}{\partial t} = -\frac{\epsilon}{\tau_\text{grow}} \tag{2.12}$$

As growth via collisions will be most efficient where dust densities are highest, pebbles are largely expected to form around the disk midplane. In our model we thus limit pebble formation to within one scale height of the disk midplane. We explore impacts of allowing pebbles to grow at all elevations in the disk in Sections 2.5 and 2.6.

The pebbles that form at a given time reflect the composition of the dust that is present. Thus we likewise adjust the abundance of any species that is frozen out onto the dust similarly to Eq. 2.12:

$$\frac{\partial X(\text{ice})}{\partial t} = -\frac{X(\text{ice})}{\tau_\text{grow}}. \tag{2.13}$$

In this treatment, we assume that once pebbles form, their ices are locked away and removed from interacting with the gas and dust in the column. This assumption is valid provided that pebble formation is limited by the drift or bouncing barriers, rather than fragmentation barriers, appropriate for the outer regions of a protoplanetary disk considered here (T. Birnstiel et al., 2012;

W. Misener et al., 2019).

2.3.4 Chemical model

Chemical evolution is modeled using a modified version of the publicly available `astrochem` solver (S. Maret & E. A. Bergin, 2015). For the gas phase reactions, we use reaction rate coefficients from the UMIST 2012 database (D. McElroy et al., 2013). Self shielding of CO and H_2 were also included following R. Visser et al. (2009). Additionally, we also account for chemistry with excited H_2 molecules (R. Visser et al., 2018, see Section A.1).

Thermal and photodesorption rates are determined following R. Visser et al. (2011). This limits the desorption rate by ensuring that each species desorbs as a function of its solid-phase abundance in the ice mantle. Binding energies are also taken from the UMIST 2012 database (D. McElroy et al., 2013). In addition, hydrogenation reactions were added to the chemical network also following R. Visser et al. (2011). Reactions with hydrogen dominate gas grain chemistry on short timescales (T. I. Hasegawa et al., 1992) and as such, hydrogenation of atomic species considered in R. Visser et al. (2011) is the only gas-grain process considered here beyond freeze-out and desorption. A list of hydrogenation reactions considered is given in Table A.1 in the appendix. As a result, CO does not react with other species when present as an ice.

These modifications make the gas and grain chemistry more similar to the chemical calculations of the DALI code (S. Bruderer et al., 2012). A detailed description of our network and chemical model is given in the appendix Section A.1. Our complete network includes 6830 reactions including 741 species.

2.3.5 Numerical Model

Within the CANDY model, we define a vertical column from the midplane ($z = 0$) to 5 scale heights ($z = 5H$) at a given stellar distance, R. The vertical column is divided into 50 cells, each with a height $dz = 0.1H$. Initially each cell has molecular abundances modified from A. D. Bosman et al. (2018) given in Table 2.1. For each cell, the initial density, temperature, column densities, optical depth, and dust-to-gas ratio are calculated.

The subsequent calculations are then carried out as illustrated in Figure 2.3. We begin by

Molecule	Abundance	Molecule	Abundance
H_2	5.00(-1)	He	9.75(-2)
NH_3	1.45(-6)	H_2O	1.18(-4)
CO	6.00(-5)	N_2	2.00(-5)
CH_4	2.00(-6)	CH_3OH	1.00(-6)
H_2S	1.91(-8)	CO_2	5.00(-5)
HCN	3.50(-7)	grains	2.20(-12)

Table 2.1: Initial abundances in each cell. Modified from A. D. Bosman et al. (2018).

running our modified `astrochem` model on each cell for a time, t_{chem} where $t_{\text{chem}} < t_{\text{tot}}$ and t_{tot} is the total simulation time. Once the chemical calculations are completed, the abundances of each species are updated. We then calculate the diffusion of each individual species through the disk over a diffusion time step, t_{diff}, using an Euler approach and ensuring that:

$$t_{\text{diff}} < \frac{(0.1H)^2}{D} = \frac{1}{100}\left(\alpha\Omega_K\right)^{-1} \tag{2.14}$$

Once species abundances are updated via diffusion, pebble growth occurs, reducing the abundances of frozen-out species within one scale height of the disk midplane following Eqn. 2.13 for the same length of time, t_{diff}. The diffusion and growth calculations are repeated again until a total time interval of t_{chem} was reached. While setting t_{chem}=t_{diff} would be ideal, it can be computationally expensive; we find $t_{\text{chem}} = nt_{\text{diff}}$ with n=5 yields convergent results while still giving reasonable run times.

After repeating the diffusion and dust growth step n=5 times, new column densities, optical depth, and dust-to-gas ratios are determined for each cell. The chemistry is then run again at each location and the process repeats until the cumulative time reaches t_{tot}.

2.4 Fiducial Cases

To begin, we consider the chemical evolution that occurs in our model disk at 30 and 40 au from the central star, regions that are just inside and outside of the CO snow line respectively. We pick these locations as we expect significant differences in carbon chemistry as a result of freeze-out of CO at the outer location. In order to isolate the consequences of pebble growth on the chemistry that occurs, we first consider two simpler disk dynamic scenarios: a *static* model and a *diffusive*

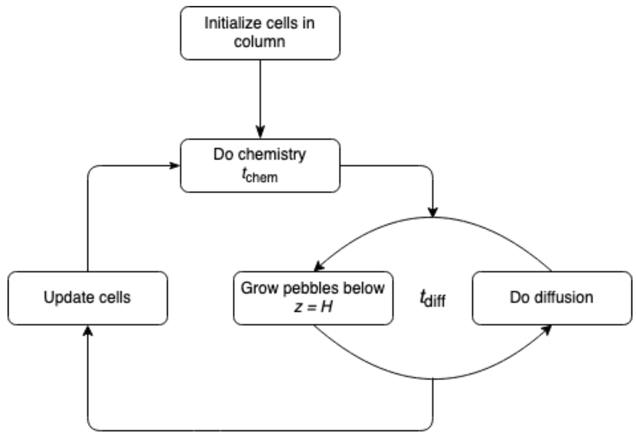

Figure 2.3: A schematic diagram of the process of the CANDY model presented in this paper. We run our models for a total of $t_{tot} = 1$ Myr with $t_{chem} = 500$ yr and $t_{diff} = 100$ yr. In other words, the chemical model is run a total of 2000 times (m=2000) for each cell, and the diffusion calculation is done 5 times (n=5) between each chemical model.

Parameter	Symbol	Value
UV Flux	χ	50
Cosmic-ray ionization rate	ζ	1.3×10^{-17} s^{-1}
Disk turbulence parameter	α	10^{-3}
Dust growth timescale parameter	a	1

Table 2.2: Fiducial model parameters. UV fluxes are given in Draine units (B. T. Draine, 1978).

model. Static modeling is the simplest and most common approach used in disk chemistry studies, in which the chemistry evolves at all heights of the disk under fixed conditions (e.g. S. Bruderer et al., 2012; F. Du et al., 2015; L. Reboussin et al., 2015; C. Walsh et al., 2015; I. Kamp et al., 2017; L. I. Cleeves et al., 2018; K. R. Schwarz et al., 2018; R. Le Gal et al., 2021; A. D. Bosman et al., 2021b). In a diffusive model, chemistry occurs while all materials are simultaneously able to diffuse through the column (e.g. D. Semenov & D. Wiebe, 2011; M. Kama et al., 2016). We present these models to compare with our *growth* model, which includes both pebble growth and diffusion as outlined above. The parameters used in these fiducial models are given in Table 2.2.

2.4.1 Static and Diffusive models

Figure 2.4 shows the distribution of CO and H_2O in the static and diffusive models. We focus on these two species to explore the differences in the behavior of key molecules with different volatilities. The initial distributions of each species in the ice and gas are also shown for reference; these are found by balancing thermal and photo-desorption with adsorption onto the grains in the absence of any other chemistry. At the locations considered here, temperatures are low enough that water is initially frozen out onto dust grains throughout most of the column, with the exception of the upper 0.5 scale heights of the disk where photodesorption is efficient. At 30 au, CO is entirely in the gas phase except for a very minor amount of CO ice that forms on the grains. At 40 au, CO is nearly completely frozen out as an ice around the midplane, but as temperatures rise at higher elevations, it returns to the gas phase.

Within the static models, we see a significant drop in the water abundance above the $\tau_{UV} = 1$ surface (which we refer to as the "photon dominated layer" or "PDL" in subsequent discussion). This is due to the high flux of UV, which leads to photodesorption off of the grains and photodissociation in the gas. Water is not completely destroyed in this region, however, as water can reform via reactions involving vibrationally excited H_2 and gas phase nitrogen (see R. Visser et al., 2018, A.1). Deeper in the disk, below the photon dominated layer, water largely remains on the ice due to the low temperatures and low photon fluxes present.

Similarly, the CO abundance and distribution between the gas and solid phases remains largely unaffected below the photon dominated layer. Above this, CO is destroyed by photodissociation but also produced by the photodesorption of CO_2 and its subsequent chemical processing. The net result is a slight increase in the CO abundance around the PDL.

When diffusion is considered, we see only slight changes in the H_2O and CO distributions when compared to the static cases. The net effect of diffusion is to smooth out concentration gradients. This is clearly seen in the H_2O distribution around the τ=1 line, where diffusion carries water-ice bearing grains to higher altitudes than in the static model. This occurs because the chemical timescales are finite, rather than instantaneous. For example, around the PDL the timescale for removing all the water from the grains is on the order $\sim$1000 years, which is longer than the residence time of grains in this region. As a result, ice-covered grains can move to higher altitudes compared to the static model. Where there is little difference between the diffusive and static cases, the timescales for reactions are short compared to the residence times.

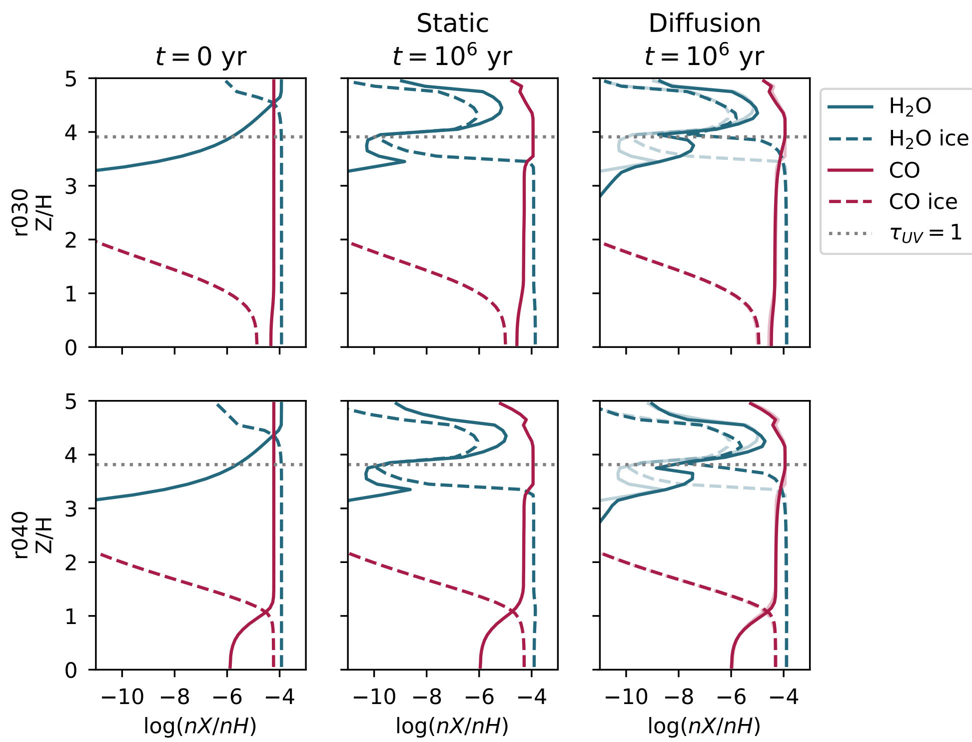

Figure 2.4: Comparison of initial conditions (left) inside (30 au, top) and outside (40 au, bottom) the CO snowline. Results after 1 Myr evolution for the static (middle) and diffusive (right) are also shown. The static evolution model is also shown as transparent lines in the final panel to help compare results.

2.4.2 Pebble growth model

Figure 2.5 shows the time evolution of CO and H_2O distributions in our pebble growth models for the same locations considered for the static and diffusive models previously.

As dust is removed, pebble formation acts as a physical sink for icy molecules around the disk midplane. Here, any species that are frozen out onto dust grains are sequestered, removing them from the active chemistry and dynamical redistribution occurring in the disk. As ice and grains are removed from the midplane, diffusion acts to transport material downward through the column, replenishing the midplane in new ices, and depleting the upper layers of the disk, even though pebbles are not forming there. In the case of H_2O, this results in its total abundance dropping by 1 to 2 orders of magnitude throughout the column at both 30 and 40 au.

Similarly, diffusion and pebble growth deplete the fine dust abundance in the upper layers of the disk. As the fine dust is the major source of UV opacity, the photon dominated region migrates deeper inside the disk, much closer to the midplane. The increased extent of the PDL drives photochemistry in denser regions of the disk, leading to the increased destruction of CO and chemical processing via excited H_2 chemistry compared to the static or diffusive models.

Figures 2.6 and 2.7 show the primary carbon carriers, and their distribution across the different reservoirs of carbon. Species in the gas and ice reservoirs are active in chemistry, and represent the gas phase or ice frozen to small dust grains, while the pebble reservoir contains the ice that has been sequestered into larger pebbles. For species that were present initially, the black dotted line shows the initial fraction of the total carbon. Both inside and outside the CO snowline, dust depletion and increased UV-radiation in the growth model increase production of HCN and HNC compared to the diffusive model. As dust is removed, increased UV-radiation excites H_2 in denser regions of the disk. This excited H_2 can react with atomic N (dissociated from N_2, again due to higher UV radiation) to create NH, in an otherwise endothermic reaction (R. Visser et al., 2018). The NH molecule can then react with atomic C, produced from the dissociation of CO, to create the cyanides HCN and HNC.

The carbon that winds up in HNC, HCN, and other secondary carriers is largely sourced from the destruction of gas phase CO. Given their lower volatilities relative to CO, this processing increases

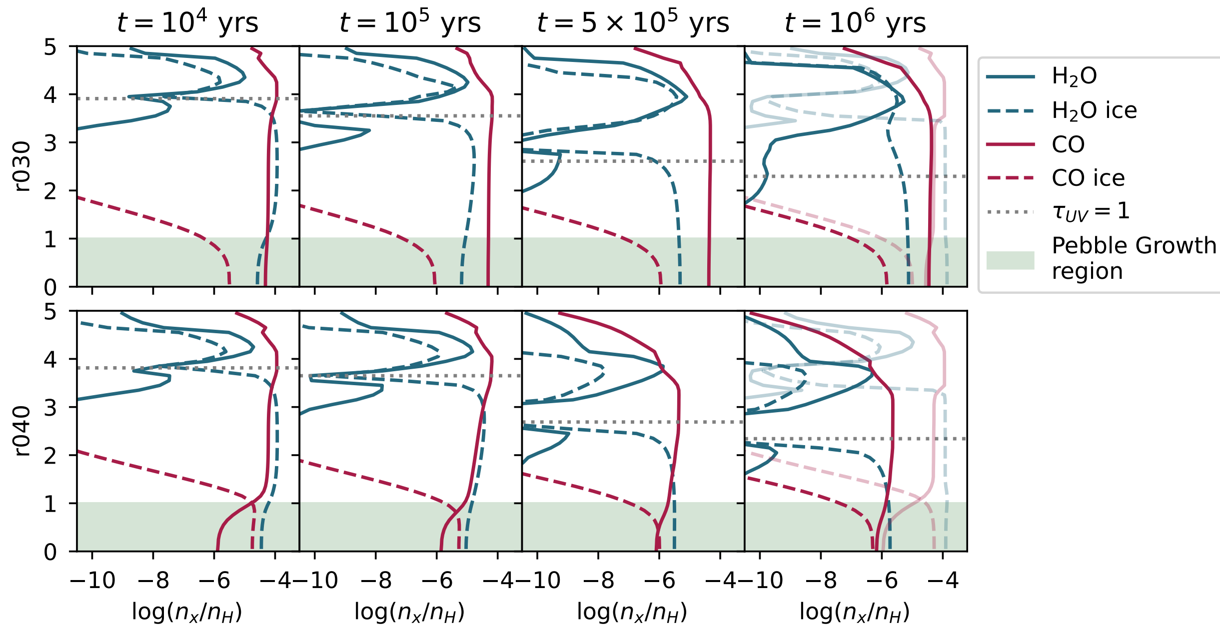

Figure 2.5: Comparison of the time evolution of CO and H_2O abundances inside (top) and outside (bottom) the CO snowline for growth models including pebble growth and diffusion. Static abundances are shown as transparent lines in the rightmost panel as a comparison.

the carbon sink that occurs via pebble formation. At 40 au, CO is largely removed via pebbles directly, limiting the amount of secondary materials produced when compared to 30 au.

The net effect of pebble growth on the CO distribution is very different at the two locations considered here. At 30 au, CO remains largely in the gas phase even close to the midplane, so pebble formation does not significantly contribute as a sink for the molecule. As a result, CO is primarily destroyed by photon-driven processing in the PDL. It is important to note that this does not occur throughout the entirety of the PDL, as CO self-shielding limits CO dissociation to the upper-most layers of the disk. The story is different at 40 au, however, as CO is frozen out at the disk midplane, and thus removed from the column via pebble formation. Diffusion from upper layers of the disk continuously replenish the midplane region with additional CO to be sequestered into pebbles. This effect, combined with the increased penetration of UV in the disk (due to removal of both dust and CO) leads to a decrease in CO throughout the column by at least 2 orders of magnitude after 1 Myr, with the greatest levels of depletion at higher altitudes (see fig 2.5).

Thus, the interplay of chemistry, diffusion, and pebble formation is critically important in shap-

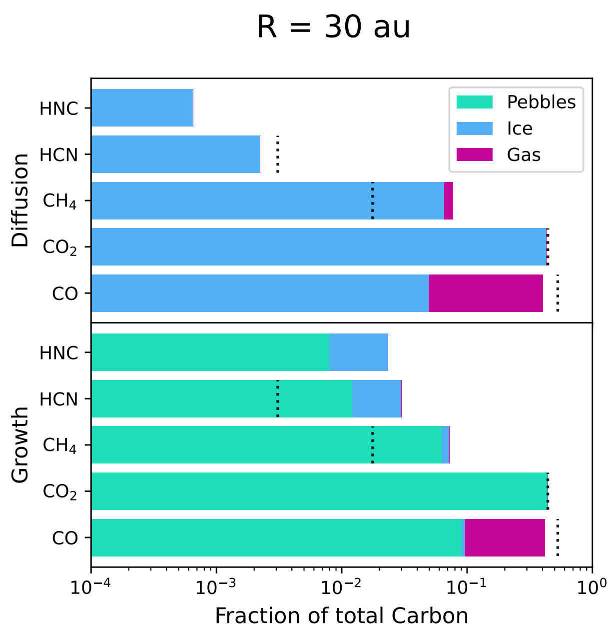

Figure 2.6: Fraction of carbon present in secondary species for the diffusive (top) and pebble growth models (bottom) at 30 au after 1 Myr. The distribution of each species into the gas, ice on small dust, and ice in pebbles is also shown. For species where the initial abundance was not zero, the black dotted line shows the initial carbon fraction. Compared to the diffusive model, about an order of magnitude more carbon is incorporated into the products HCN and HNC in the growth model. This is due to increased UV-driven chemistry in the disk as a result of the removal of small dust.

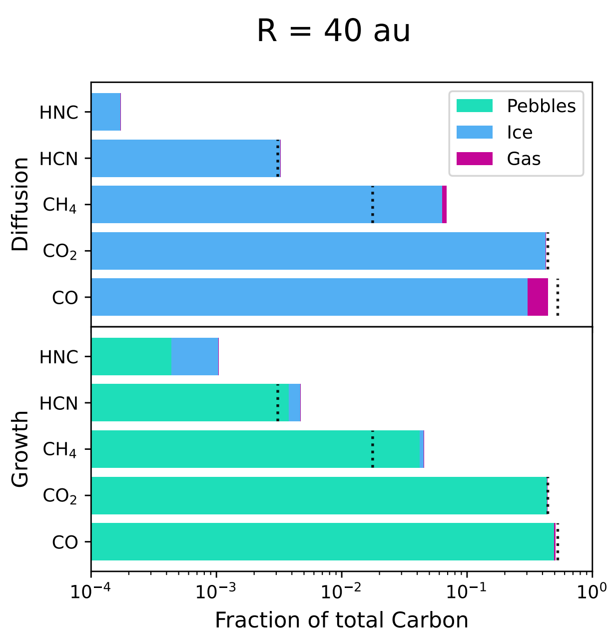

Figure 2.7: Same as Figure 2.6 but at 40 au, outside the CO snowline. Relative fractions of all secondary carbon carriers is lower than in the 30 au case, as CO is primarily in the ice phase, and thus is not as readily processed.

ing the distribution of molecules throughout a column of the disk. In the next sections we explore how this interplay depends on the conditions present in the disk by focusing on two important themes related to protoplanetary disk observations: CO depletion and the C/O ratio.

2.5 CO Depletion During Pebble Growth

As discussed in the previous section, the depletion of CO in a column will arise due to two active sinks: chemical processing of CO gas that largely occurs in the PDL, and pebble formation around the midplane that sequesters CO ice into large dust aggregates. The extent and time over which these processes operate will determine the amount to which CO is depleted in the column and timescale over which this depletion occurs. Figure 2.8 shows the CO depletion within the emissive layers of the disk, defined as T > 21 K (S. Krijt et al., 2020), after 1 Myr at various radial locations in the disk. The depletion factor is given by

$$f_{\rm depl} = \frac{X_0}{X_f} \tag{2.15}$$

where X_f is the abundance of CO or small dust grains after 1 Myr evolution, and X_0 is the initial abundance: 10^{-4} for CO and 2.2×10^{-12} for small dust (small dust-to-gas ratio of $\epsilon = 0.01$). In each panel, different sets of parameters are considered. We compare the modeled depletion levels to observed CO depletion factors, which are on the order of 1-2 orders of magnitude below interstellar C. Favre et al. (2013); K. Zhang et al. (2019). Notably, CO depletion is a robust outcome independent of our model assumptions, though the extent of depletion is sensitive to the different conditions present within the disk.

For the fiducial model, we find that the greatest CO depletion occurs in the region just beyond the CO snow line (40-60 au), while the CO abundance rises again at larger distances (100 au). This indicates that the formation of pebbles and sequestration of ices plays a critical role in CO depletion; if photo-processing alone were more important, we would expect higher depletion levels in the outer disk where UV can penetrate more deeply. The lack of CO depletion inside the CO snow line is further evidence of the importance of pebble formation in reducing CO levels in the disk.

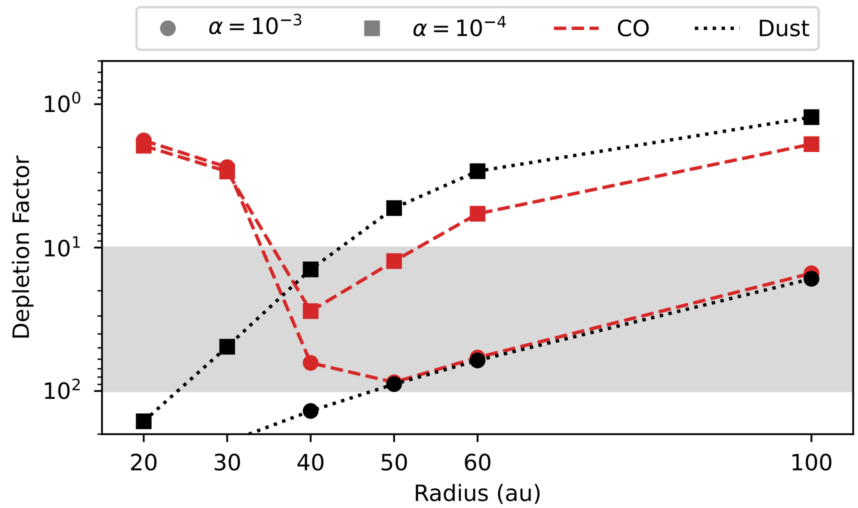

Figure 2.8: CO and dust depletion relative to ISM abundance of 10^{-4} and small dust-to-gas ratio of 0.01 in the warm molecular region ($T > 21$K) as a function of radial distance after 1 Myr of evolution. CO abundance generally follows the evolution of small dust, shown in black, outside of the CO snowline (∼35 AU). Observed CO depletion ranges of 1-2 orders of magnitude are shaded in grey.

The higher depletion levels around the CO snowline compared to the outer disk is due to the shorter time scales associated with dust growth and diffusion of small gas. As the growth time scale of pebbles scales with orbital period (see Eq. 2.11), a greater fraction of dust is converted into pebbles within 1 Myr at smaller radii, corresponding to more efficient removal of CO ice. The slightly lower depletion of CO at 40 au instead of 50 au in some cases is due to the shallow temperature gradient in the disk: there is a non-trivial amount of CO that remains in the gas phase at the disk midplane at 40 au despite the ice being the dominant form there. At larger distances, the amount of gas phase CO at the midplane is negligible.

Diffusion plays an important role in setting the level of CO depletion that occurs in the disk. The effect of different α values on the extent of CO depletion after 1 Myr is shown in Figure 2.8. In our model, pebble formation only occurs around the disk midplane; diffusion of dust downward reintroduces solids and allows ices to be further sequestered in the model. For pebble formation to be an effective sink for the CO, diffusion is necessary to carry the CO to greater depths where it can freeze out as an ice. Thus, the extent and timing of depletion is intimately connected to the level of turbulence present. The timescale for vertical diffusion is $t_{diff} = H^2/D = (\alpha\Omega)^{-1}$. At 40 au, this gives $t_{diff} \sim 4{\times}10^4$ years for α=10^{-3}, and 10× greater for α=10^{-4}. Faster diffusion results in more efficient removal of CO when there is an active sink around the midplane. Given that significant CO depletion is seen across a wide variety of disks, including young disks, this points to an active environment that enables efficient vertical transport of gases in disks.

The relative roles of dust dynamics and chemical processing in shaping the CO distribution can be seen when comparing the level of CO depletion to the level of dust depletion in Fig. 2.8. In the α=10^{-3} case, the level of CO and dust depletion are nearly identical at 50 AU or beyond, indicating that CO depletion is most strongly controlled by pebble formation. Closer in, because much of the CO remains in the gas phase, even around the midplane, the dust is depleted to a greater level than the CO. However, in the α=10^{-4} cases, the dust is depleted to a lesser extent than the CO. This indicates that chemistry and photo-processing contribute more to CO depletion than in the more turbulent cases.

The extent of CO depletion in our models depends somewhat on the physical parameters of the disk. The details of these differences are discussed in the appendix A.2.1. However, regardless of physical parameters, CO depletion is a robust outcome of our model, although to match observed depletions of 1-2 orders of magnitude high turbulence ($\alpha = 10^{-3}$) is necessary.

2.6 C/O Response to Ice Sequestration

As discussed in the previous section, pebble formation aids in the depletion of volatiles in a disk by the removal of ices around the midplane. The removal of ice species may impact subsequent gas-phase chemistry by changing the abundances and proportions of various reactants. For example, E. A. Bergin (2016) suggested that preferential removal of O-bearing species on pebbles may produce high C/O ratios, leading to the formation of hydrocarbons such as C_2H. Indeed, C_2H formation is favored by C/O values > 1.5-2, approximately 4-5× the canonical value to be inherited from the ISM (A. D. Bosman et al., 2021a).

Figure 2.9 shows the evolution of the major carbon- and oxygen-bearing species at 30 au along with the bulk C/O ratio in ice and gas. While water is initially the most abundant oxygen carrier, its abundance drops rapidly due to the formation and removal of pebbles. The next most important oxygen bearing species from our starting inventory is CO_2; while CO is more abundant, CO_2 carries

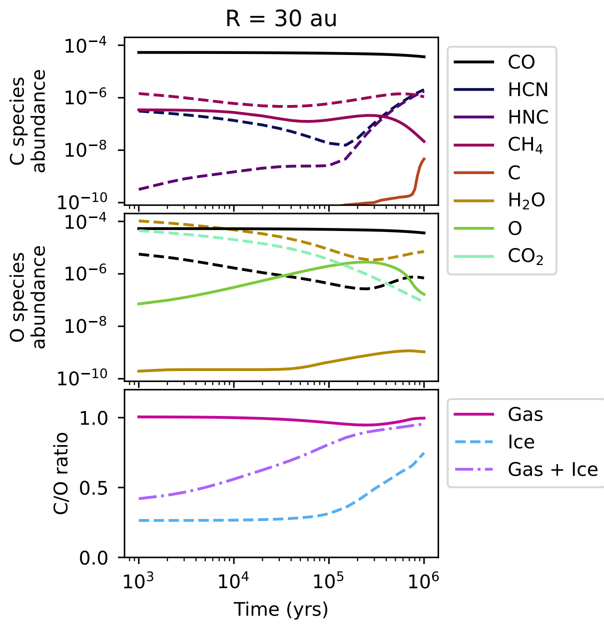

Figure 2.9: Most abundant column averaged carbon (top) and oxygen (middle) bearing species in the gas and ice. Dashed lines indicate ice phase abundances and solid lines represent gas phase abundances. Bulk C/O of the gas, ice, and ice and gas combined (bottom)

twice the amount of oxygen (see Table 2.1). At 30 au, CO_2 is largely present as an ice and is removed from the column along with water. The loss of H_2O and CO_2 ice leads to a net increase in the C/O ratio in the remaining gas + ice. As pebble growth removes ice, the total gas + ice C/O ratio becomes weighted more heavily towards the gas C/O, which is now dominated by CO, leading to C/O$\sim$ 1. As oxygen carriers become less and less abundant, the ices become increasingly rich in carbon and nitrogen, with cyanides the dominant carbon carriers in the ice by 1 Myr.

The evolution of the C/O ratio in the column will thus be sensitive to the partitioning of C and O into carriers with different volatilities, which will vary strongly with location. This is illustrated in Figure 2.10 which shows the C/O ratio of the gas and ice, as well as the total (gas+ice) C/O ratio throughout the column after 1 Myr of evolution at various locations in the disk. With the starting abundances in our model,the column begins with a C/O ratio of $\sim$0.4 throughout. Inside of the CO snow line, the C/O ratio increases everywhere as O-rich ices, notably H_2O and CO_2 are removed via pebble growth as described above, but CO gas remains behind. This allows C-rich ices, such as HCN, HNC, and CH_4, to develop later in disk evolution. While this creates ice C/O ratios > 1 in some regions of the disk, the ice abundances in these regions tend to be low, and the total ice+gas C/O ratios closely follow the gas C/O. Outside of the CO snow line, CO, CO_2, and H_2O are all removed equally, resulting in a negligible net effect on the bulk C/O ratio in the column. C/O ratios are higher in the gas around the disk midplane, but this is due to the small amount of CO left in the vapor phase.

In none of our cases, do we see C/O ratios that rise above $\sim$1, reaching the levels that have been inferred from disk observations of hydrocarbons. The key to reaching high C/O ratios is for oxygen to be incorporated into ices while carbon remains in the gas phase. The loss of H_2O and CO_2 via pebble growth produces C/O ratios of $\sim$1 within the CO snow line. Going beyond this value is a challenge, and seemingly can only be achieved if CO is dissociated and the carbon is partitioned into a more volatile carrier than H_2O. However, as discussed in Section 2.4.2, the majority of secondary carbon species are present as ices, and so both the carbon and oxygen from any dissociated CO is removed from the gas phase, leaving the total C/O unaffected.

This result is robust across the physical conditions considered, though the details are discussed in Section A.2.2. In general, the chemical processing of gas phase CO is too slow to raise C/O ratios above unity inside the CO snowline despite the removal of the oxygen rich ice. Outside of the CO snowline, carbon and oxygen are removed equally and there is no net change to the C/O ratio in the column.

2.7 Discussion

The growth of small dust into larger pebbles has two main effects on the gas phase chemistry of the disk

1. removal of small dust from upper layers of the disk extends the photon dominated layer, and

2. selective sequestration of ices can affect elemental abundances in the gas phase.

These two effects occur simultaneously with the ongoing chemical evolution in the gas. Collectively, this leads to an important feedback, altering the chemistry that occurs over million year timescales compared to static or diffusive disk models. Here we review our main findings and discuss how they can be used to interpret ongoing observations of protoplanetary disks.

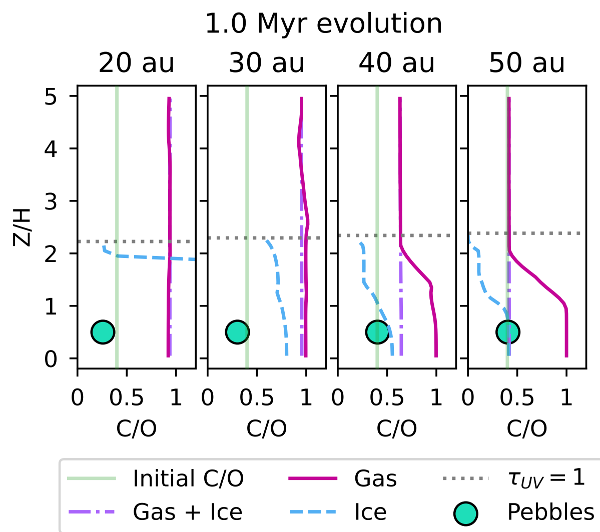

Figure 2.10: C/O ratios of the disk profiles at 20 au (left), 30 au (middle left), 40 au (middle right) and 50 au (right). Locations inside the CO snowline (30 and 40 au) tend to have C/O ratios close to unity throughout the column, while regions outside the C/O snowline (40 and 50 au) do not have C/O ratios above the inherited value. The initial C/O of 0.4 is shown by the green vertical bar.

2.7.1 CO Depletion

We find that CO depletion is ubiquitous outside of the snowline. For our fiducial model we find depletion factors from ∼10-100 in the outer disk, with comparable or lower depletion factors (2–100) seen for different assumptions of turbulence, growth timescale, or dust formation height. This result is particularly important in light of the wealth of observational evidence that gas-phase CO is under-abundant by up to 2 orders of magnitude in protoplanetary disks compared to the interstellar medium, on timescales of only ∼1 Myr (J. B. Bergner et al., 2020; K. Zhang et al., 2020).

This finding expands upon previous studies, which showed that CO can be depleted up to a factor of 10 in static chemical models (L. Reboussin et al., 2015; A. D. Bosman et al., 2018; K. R. Schwarz et al., 2018), or by a factor of ∼10 by freeze-out onto dust and pebble formation (M. Kama et al., 2016; S. Krijt et al., 2018). As these studies treated either just chemistry or dust growth, it was suggested that the combined effects of both may be necessary to explain the observed depletions in disks. S. Krijt et al. (2020) was the first to combine physical and chemical processes, by including a simplified carbon chemical network in a pebble growth model. They found that CO could be depleted by 2 orders of magnitude on a 3 Myr timescale in this framework. Our model extends the chemistry beyond 5 carbon-bearing species and considers a full astrochemical network. With this update, our model can achieve 2 orders of magnitude depletion of CO on a faster timescale (∼1 Myr). This is likely due, in part, to the inclusion of photochemistry in our model, which results in CO destruction in the disk surface layers in addition to ice sequestration in the midplane. Although our model does not include hydrogenation of CO on the grains, further processing of CO ice would not greatly affect the gas abundance of CO in our vertical diffusion model on 1 Myr timescales. In our model, gas phase CO is quickly sequestered into the pebbles, and so the growth mechanism presented here is the dominant source of CO depletion on shorter timescales ($\leq$ 1 Myr). However, this secondary processing of CO ice would further reduce the CO gas abundance on longer timescales and may be more important in inner regions of the disk (inside the CO snowline) and when considering the inward drift of pebbles. Our model can thus explain observations of CO depletion even in young ($\lesssim$1 Myr) disks (L. I. Cleeves et al., 2018; J. B. Bergner et al., 2020; S. Krijt et al., 2020).

We also explored various physical parameters to test the robustness of these results. Interestingly, we find that high values of α (10^{-3}) are required to explain CO depletion factors of 10–100 on 1 Myr timescales throughout much of the disk. Models with $\alpha = 10^{-4}$ show less depletion, around $\sim$ 30× immediately outside the CO snowline, and even lower (2×) in the outer disk. This is because diffusion is necessary to carry CO gas from the surface regions of the disk to the deeper interiors where it can freeze out and be incorporated into growing pebbles. This helps explain why S. Krijt et al. (2020) were able to reach similar levels of depletion, but on longer timescales,as they used α=10^{-4}. α values around 10^{-3} are consistent with, if on the high end, of the range inferred from observations of mature protoplanetary disks (K. M. Flaherty et al., 2017; C. P. Dullemond et al., 2018; R. Teague et al., 2018b).

2.7.2 C/O ratios

In our models, the selective removal of oxygen through ice sequestration within the CO snowline enhances the C/O ratio to about unity. This is still below the C/O ratios ($\gtrsim$ 1.5) inferred for disk surface layers via observations of C_2H (E. A. Bergin, 2016; A. D. Bosman et al., 2021a). Indeed, in our fiducial model the C_2H column density peaks at $3{\times}10^{-13}$ cm^{-2} (Figure 2.11) as compared

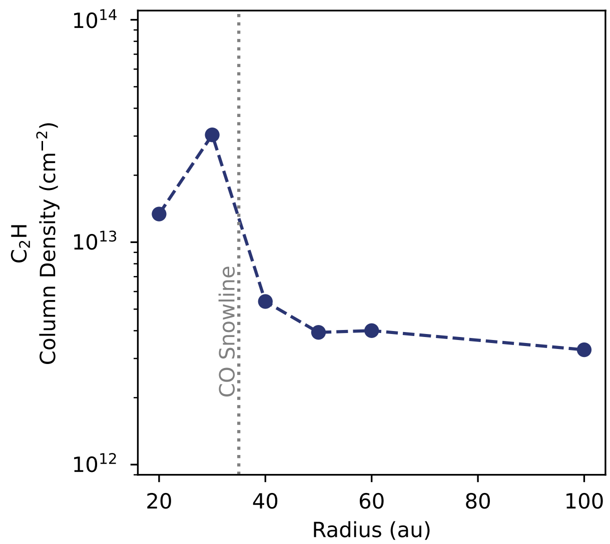

Figure 2.11: C_2H column density at different radial locations for the fiducial model. Modeled C_2H column densities remain 1-2 orders of magnitude below observed values of 10^{14} - 10^{15} cm^{-2}.

to observed C_2H column density peaks of $10^{14} - 10^{15}$ cm^{-2} (J. B. Bergner et al., 2019; V. V. Guzmán et al., 2021). Moreover, we achieve a high C/O only interior to the CO snowline, whereas observations of C_2H emission probe disk regions beyond the snowline. Thus, our model does not reproduce the carbon-rich chemistry observed in disk surface layers.

While C_2H is primarily a tracer of UV chemistry and C/O ratios (A. D. Bosman et al., 2021a), X-ray chemistry may further drive C_2H production in surface layers of the disk (H. Nomura et al., 2007; T. Henning et al., 2010). In our models we have included cosmic ray ionization, which behaves similarly to X-rays in mechanism (e.g. ionization of molecular hydrogen). X-ray induced chemistry can be important on the surface layers and can be considered in further implementations of the model.

In our model, CO destruction results in the formation of O-bearing and C-bearing species with comparable volatilities (e.g.H_2O and midsize hydrocarbons), which freeze out onto grains at similar temperatures. CO remains the main gas-phase carrier of C and O, resulting in a gas-phase C/O of unity. Unless our model over-predicts the formation of large carbon chains at the expense of more volatile carbon carriers like CH_4, a combined chemistry and pebble growth framework cannot explain the C/O levels >1 inferred from disk observations. Additional carbon insertion, i.e. from photoablation of grains (A. D. Bosman et al., 2021a), is then necessary to explain C/O ratios above unity.

The carbon abundance in refractory grains is $10^{-4} \times 100\epsilon$, where ϵ is the dust to gas ratio (A. D. Bosman et al., 2021a). After 1 Myr of evolution at 30 au, dust is depleted by a factor of 50, such that $\epsilon = 2 \times 10^{-4}$, resulting in a carbon abundance in grains of 2×10^{-6}. The ablation of 100% of these remaining small grains would be necessary to raise the C/O ratio to ~2. This scenario is not realistic, implying that carbon grain destruction should be ongoing over the course of grain growth and disk evolution. Additionally, grain ablation would provide a similar feedback on the chemistry as grain growth, via the removal of UV opacity and the increase in gas-phase C/O. Further implementations of this model will be able to capture grain ablation simultaneously with growth and chemistry.

2.8 Conclusions

We have developed a new technique to self-consistently model the growth and dynamics of small dust with a full gas and grain chemical network in a 1D vertical column of the protoplanetary disk. Using this new approach, we have explored in detail the influence of dust growth on CO depletion and C/O ratios in the disk. We find that a disk turbulence parameter of $\alpha = 10^{-3}$ is most closely able to match observed CO depletions of 10-100 below ISM abundances (C. Favre et al., 2013; K. Zhang et al., 2019). Additionally, we find that selective removal of H_2O ice inside of the CO snowline is able to increase C/O to unity, but are unable to reach higher C/O values implied by the observations of C_2H in disks (E. A. Bergin, 2016; A. D. Bosman et al., 2021a).

CHAPTER 3
THREE-DIMENSIONAL TRANSPORT OF SOLIDS IN A PROTOPLANETARY DISK

This chapter has been published as the following:

Van Clepper, E., Price, E. M., & Ciesla, F. J. 2025, "Three-dimensional Transport of Solids in a Protoplanetary Disk Containing a Growing Giant Planet", *The Astrophysical Journal*, **980**, 201, doi: 10.3847/1538-4357/ada8a4.

3.1 Chapter Abstract

We present the results of combined hydrodynamic and particle tracking post-processing modeling to study the transport of small dust in a protoplanetary disk containing an embedded embryo in 3D. We use a suite of FARGO3D hydrodynamic simulations of disks containing a planetary embryo varying in mass up to 300 $M_\oplus$ on a fixed orbit in both high and low viscosity disks. We then simulate solid particles through the disk as a post-processing step using a Monte Carlo integration, allowing us to track the trajectories of individual particles as they travel throughout the disk. We find that gas advection onto the planet can carry small, well-coupled solids across the gap opened in the disk by the embedded planet for planetary masses above the pebble isolation mass. This mixing between the inner and outer disk can occur in both directions, with solids in the inner disk mixing to the outer disk as well. Additionally, in low viscosity disks, multiple dust pile-ups in the outer disk may preserve isotopic heterogeneity, possibly providing an outermost tertiary isotopic reservoir. Throughout Jupiter's growth, the extent of mixing between isotopic reservoirs varied depending on dust size, gas turbulence, and the Jovian embryo mass.

3.2 Introduction

As giant planets form, they sculpt their surroundings through gravitational interactions, creating rings, gaps, and spiral structures throughout the protoplanetary disks (PPDs) in which they are embedded. Such rings and gaps have been observed in numerous extrasolar PPDs (e.g. S. M. Andrews et al., 2018; K. I. Öberg et al., 2021), and in some cases the observed gas dynamics have been used to infer the existence of exoplanets in these disks (C. Pinte et al., 2018, 2019; R. Teague et al., 2018a; A. F. Izquierdo et al., 2022). The flows of gas that develop as a result of these interactions play important roles in the dynamics of small dust and pebbles in the disk, as their trajectories are closely tied to the gas structure. Modeling these interactions in detail is key to understanding the formation history of planetesimals and planets in (extra-)solar systems.

The role that these substructures play in the compositional diversity of planetary materials is uncertain. In our own solar system, measurements of multiple isotopic systems have revealed a clear dichotomy between the carbonaceous (CC) and non-carbonaceous (NC) meteorites, including both chondritic and non-chondritic meteorites (P. H. Warren, 2011; G. Budde et al., 2016; T. S. Kruijer et al., 2017). This dichotomy has been hypothesized to be the result of the preservation of two distinct compositional reservoirs in the solar nebula via a gap opened by a growing Jovian embryo (T. S. Kruijer et al., 2017; S. Gerber et al., 2017; S. Ebert et al., 2018; T. S. Kruijer et al., 2020). Such a gap can create a pressure "bump" (a local pressure maximum) exterior to the planet where the gas pressure gradient is zero and the orbital velocity is Keplerian. In this region, solids and the surrounding gas co-orbit at the same speed, and the drag induced inward drift of solids halts. This can result in the creation of ring-like structures exterior to the planet at the local pressure maximum as solids drift into this region from beyond, depleting the exterior regions of the disk as solids pile up at the bump (see e.g. P. Pinilla et al., 2012; C. P. Dullemond et al., 2018). In the solar system, this ring and gap substructure may be responsible for halting the inward drift of CC-like material and calcium-aluminum-rich inclusions (CAIs) from the outer disk to the inner disk, preserving the isotopic dichotomy observed in the meteorite record (M. Lambrechts et al., 2014; T. S. Kruijer et al., 2017; S. J. Desch et al., 2018; T. S. Kruijer et al., 2020). While today, NC and CC parent bodies coexist in the asteroid belt interior of Jupiter's orbit it is assumed that they formed in these spatially distinct reservoirs separated by Jupiter during the disk's lifetime. After the dispersal of the disk, both asteroid families could be scattered to their current day locations, mixing the NC and CC parent bodies (e.g. K. J. Walsh et al., 2012; S. N. Raymond & A. Izidoro, 2017).

In addition to the bulk isotopic differences measured in meteorites, isotopic differences have also been measured in individual refractory inclusions within meteorites. For example, CAIs and sodium-aluminum-rich chondrules, two types of refractory inclusions found in both ordinary and carbonaceous chondrites, show distinct Ti isotopic ratios from one another, further indicating two reservoirs in the disk from which these refractory inclusions may have formed (S. Gerber et al., 2017; S. Ebert et al., 2018). In addition to these isotopic differences, NC and CC meteorites have different distributions of CAIs, with CC chondrites tending to have both larger and a higher volume percent than NC chondrites (E. T. Dunham et al., 2023).

Although Jupiter is often invoked as the separator of these two reservoirs, some studies have brought into question the extent to which the embedded Jovian embryo could have prevented the exchange of material between them. In 1D models, while large solids remain trapped at pressure bumps, accretion flows onto the star through the disk may drag sufficiently small particles across pressure bumps, mixing outer and inner reservoirs (J. Chambers, 2021). In 2D, the interactions between the planet and disk result in non-axisymmetric substructures in the disk that further affect the trajectories of small solids in the disk. For example, interactions between the embedded giant planet and surrounding disk can create more complex substructures than a simple ring and gap, such as spiral wakes and vortices (Z. Zhu et al., 2014; J. Bae et al., 2017; J. Bae & Z. Zhu, 2018). The asymmetry in the disk near the planet can have important implications for dust dynamics, in particular the transport of smaller solids from the outer reservoir to the inner nebula, also referred to as the "filtering" of material across the planet (P. Weber et al., 2018; T. Haugbølle et al., 2019; S. M. Stammler et al., 2023). Such filtering also depends on the gas advection through the disk and the planet's migration through the disk (A. Morbidelli et al., 2023). In 3D, the planet creates meridional flows, driving gas away from the planet at the midplane and onto the planet from the upper regions of the disk, such flows have been observed in real protoplanetary disks, indicating a promising method for identifying new embedded planet candidates (A. Morbidelli et al., 2014; J. Szulágyi et al., 2014; J. Fung & E. Chiang, 2016; R. Teague et al., 2019; J. Szulágyi et al., 2022). The consequences of this 3D structure created by an embedded planet on the subsequent transport of solids in the disk remains uncertain.

To date, models investigating the dynamics of solids in PPDs generally treat both the gas and dust as fluids, solving the continuity equations on a grid, giving gas and dust densities and velocities at fixed locations throughout the disk (J. Szulágyi et al., 2014; L. Krapp et al., 2022; J. Szulágyi et al., 2022; F. Binkert et al., 2023). While these approaches are useful for determining large scale gas and dust structures through the disk, it is difficult to determine the detailed histories — that is, the physical conditions experienced — of individual particles through the disk, and the pathways through which material may or may not cross the gap opened by an embedded giant planet.

Here, we use a particle tracking technique to study the 3D dynamics of small solids in a disk containing an embedded planetary embryo. This approach allows us to track the histories of small dust and pebbles in a protoplanetary disk during different stages of a Jupiter-like planet's growth. Specifically, this approach allows us to connect different regions of the disk, identifying not only regions of the disk where solids concentrate, but also from where those solids may have originated in the disk. We can also identify the mechanisms by which potential mixing between reservoirs in the disk occurs and the extent of mixing based on disk and grain parameters.

While we focus specifically on an embedded Jovian embryo and implications for planetesimals in the solar nebula, the results presented here are applicable to protoplanetary disks broadly. In Section 3.3 we describe the hydrodynamic simulations of the gaseous disk containing the embedded planet and the Monte Carlo integration technique used to track the solid particles. In Section 3.4 we present the results of this suite of models and discuss their implications within a Solar System context in Section 3.5. In Section 3.6 we summarize our results and present avenues for future research.

3.3 Methodology

In this work, we combine FARGO3D hydrodynamic simulations (F. Masset, 2000; P. Benítez-Llambay & F. S. Masset, 2016) with the particle tracking technique of F. J. Ciesla (2010, 2011) to track the evolution of small dust through a PPD sculpted by an embedded planetary embryo. We first simulate the gas disk as a single fluid in FARGO3D until a steady state is reached. We explore a variety of disk conditions including a range of planet masses and disk viscosities. We then simulate a population of dust particles in a post-processing step, holding the gas density and velocity field constant over the particle integration. Particle sizes studied here range from 10 µm to 1 cm, corresponding to small, well coupled solids up to largest inclusions found in meteorites, including CAIs and other meteorite constituents (see e.g. E. T. Dunham et al., 2023). Thus, we

Planet Mass, M_{pl}	Viscosity	Particle Sizes, s
$M_\oplus$	$\log_{10}\alpha$	cm
0	-3, -4	1, 0.1, 0.01, 0.001
1	-3	1, 0.1, 0.01, 0.001
5	-3	1, 0.1, 0.01, 0.001
10	-3, -4	1, 0.1, 0.01, 0.001
20	-3, -4	1, 0.1, 0.01, 0.001
50	-3, -4	1, 0.1, 0.01, 0.001
100	-3, -4	1, 0.1, 0.01, 0.001
200	-3	1, 0.1, 0.01, 0.001
300	-3, -4	1, 0.1, 0.01, 0.001

Table 3.1: Model parameters for simulations.

expect these results to be informative of the dynamics of the range of dust sizes in the solar nebula. A full list of all the different models considered is given in Table 3.1.

3.3.1 Hydrodynamic Simulations

Using the publicly available version of FARGO3D (F. Masset, 2000; P. Benítez-Llambay & F. S. Masset, 2016), we use a 3D, spherical mesh to simulate a gaseous disk around a solar-mass star. The mesh has $2048 \times 256 \times 32$ ($N_\phi \times N_r \times N_\theta$) cells, with logarithmic spacing in the radial direction, and the mesh being defined on $\phi \in (-\pi, \pi)$, $r/R_0 \in (0.5, 3.0)$, and $\theta \in (\pi/2 - 0.15, \pi/2)$. Within each mesh, we include an embedded planet with constant mass, M_{pl}, varying from 0 to 300 $M_\oplus$. In all cases, we place the planet at the midplane, $\theta = \pi/2$, and at the azimuthal angle $\phi = 0$. We define the physical radius of the planet's orbit to be $R_{pl} = R_0 = 5.2$ au. The planet's orbit is held fixed at this location throughout the hydrodynamic simulation and particle integration. We use a rotating reference frame such that the planet remains at $\phi = 0$ throughout the simulation.

The initial surface density of the disk at $r = R_0$ is $\Sigma_0 \approx 210$ g cm^{-2}, and it scales radially as

$$\Sigma(r) = \Sigma_0 \left(\frac{r}{R_0}\right)^{-1}. \tag{3.1}$$

We set the temperature in the disk to be $T(R_0) = T_0 \approx 118K$, and it scales radially as $T \propto r^{-1/2}$. These values correspond to a surface density and temperature at 1 au of $\Sigma(1 \text{ au}) = 1088$ g cm^{-2} and $T(1 \text{ au}) = 270$ K respectively. The scale height of the disk at $r = R_0$ is $H(R_0) = H_0 = 0.05R_0$

with a flaring index of 1/4; that is, the gas scale height is given by

$$H(r) = \frac{c_s}{\Omega_k} = 0.05r \left(\frac{r}{R_0}\right)^{1/4} \tag{3.2}$$

where c_s is the sound speed of the gas and $\Omega_K = \sqrt{GM/r^3}$ is the Keplerian orbital frequency. As such, the FARGO3D mesh extends approximately 3 scale heights above the midplane. The kinematic viscosity of the disk is then given by $\nu = \alpha c_s H$ as in N. I. Shakura & R. A. Sunyaev (1973), where we use $\alpha = 10^{-3}$ and 10^{-4} in our models. The temperature profile is held constant throughout the simulation and the disk is vertically isothermal.

The disk is initially axisymmetric and in hydrostatic equilibrium, with the equation for density throughout the disk given in the appendix B.1. In the co-rotating frame with the planet, the rotation rate of the frame, Ω_f, is equal to the orbital frequency of the planet, Ω_0.

Each model is integrated for at least 500 orbits of the planet ($\sim$ 5900 years), or until a steady state in gas density is reached. We define a steady state in the disk as being reached when the azimuthally averaged midplane density everywhere in the disk changes by less than 1% over the course of one orbit. For some models a steady state is not reached before 1000 orbits, and the midplane experiences small oscillations over orbital timescales. For these cases, we use a time average of the ten orbits from 990 to 1000 for the particle integration, following J. Fung & E. Chiang (2016). Although this approach may ignore some transient structures such as vortices at the gap edges, the timescale of these orbit-to-orbit variations are short compared to the integration time of the particles, and vortex lifetimes for planets smaller than $1M_{\rm Jup}$ tend to be shorter than the timescales considered here (M. Hammer et al., 2017). The effect of this time-varying density on particle transport can be explored in future work.

3.3.2 Particle Integration

Particles are taken to be compact spheres with a given constant size, s, and solid density, $\rho_s = 2$ g cm^{-3}. This choice of solid density corresponds with fluffy dust aggregates. Each particle's initial radial and azimuthal velocity is determined from analytic particle velocities for an axisymmetric disk based on the surrounding gas velocity (T. Takeuchi & D. N. C. Lin, 2002; P. J. Armitage, 2017).

The particle is forward integrated following the technique of F. J. Ciesla (2010, 2011) extended to 3D, non-axisymmetric structure. The particle tracking is done in Cartesian coordinates, with the gas density and velocity at the position of the particle interpolated from the FARGO3D outputs. Using this particle tracking technique, as opposed to fluid or dye-tracking approaches, allows us to follow the trajectories of individual particles, seeing how solids may transit across different regions of the disk. In the current public release of FARGO3D, solids are treated as pressureless fluid of constant Stokes number. Here, we use a constant particle size in the integration, thus the drag on a given particle can be consistently determined at each time and location, adjusting the particle's Stokes number as it moves through different environments. As a particle moves through the disk, the surrounding gas density, and thus particle Stokes number, can vary by multiple orders of magnitude, and accounting for this difference can have important consequences for resulting solid dynamics (P. Weber et al., 2018, Price et al. *in press*).

In our model, each particle's location and velocity is integrated forward in time using an Eulerian approach:

$$\boldsymbol{Y}^i = \boldsymbol{Y}^{i-1} + \frac{\partial}{\partial t}\boldsymbol{Y}^{i-1}\Delta t + \boldsymbol{R}\left[6D(\boldsymbol{x}')\Delta t\right]^{1/2} \tag{3.3}$$

where

$$\boldsymbol{Y}^i = \begin{bmatrix} x^i \\ y^i \\ z^i \\ v_x^i \\ v_y^i \\ v_z^i \end{bmatrix} \tag{3.4}$$

is a 6D Cartesian position and velocity vector. We can also write $\boldsymbol{Y}^i = [\boldsymbol{x}^i, \boldsymbol{v}^i]$ where $\boldsymbol{x}^i = [x^i, y^i, z^i]$ and $\boldsymbol{v}^i = [v_x^i, v_y^i, v_z^i]$, giving the Cartesian position and velocity (respectively) of the particle in the co-rotating frame centered at the center of mass of the system. The superscript i, denotes the values of $\boldsymbol{Y}$ at the i-th timestep. Where it is not necessary, we drop the i superscript for simplicity. The last term in equation (3.3) represents a random displacement over timestep Δt associated with diffusion, with $\boldsymbol{R} = [p_x, p_y, p_z, 0, 0, 0]$ where $p_{[x,y,z]}$ is a random number drawn from a uniform distribution ranging from [-1,1]. $\boldsymbol{x}'$ is a location chosen near $\boldsymbol{x}^{i-1}$ offset toward increasing diffusivity and is given by

$$\boldsymbol{x}' = \boldsymbol{x}^{i-1} + \frac{1}{2}\boldsymbol{\nabla} D(\boldsymbol{x}^{i-1})\Delta t \tag{3.5}$$

and $D(\boldsymbol{x})$ is the diffusivity of the particle at a given location (see discussion in F. J. Ciesla, 2010). Thus, we assume diffusion leads to a random displacement of the particle without changing its velocity. The particle diffusivity is related to the gas diffusivity using the relationship given in A. N. Youdin & Y. Lithwick (2007):

$$D = \frac{D_g}{1 + \mathrm{St}^2}. \tag{3.6}$$

where

$$\mathrm{St} = t_{\mathrm{stop}}\Omega_K \tag{3.7}$$

is the Stokes number and

$$t_{\mathrm{stop}} = \frac{\rho_s s}{\rho_g c_s} \tag{3.8}$$

is the stopping time of the particle. The gas diffusivity is the same as the kinematic viscosity $D_g = \nu = \alpha c_s H$, e.g. we assume a Schmidt number of unity.

The time derivative of $\boldsymbol{Y}$ is

$$\frac{\partial}{\partial t}\boldsymbol{Y} = \begin{bmatrix} v_{\mathrm{eff},x} \\ v_{\mathrm{eff},y} \\ v_{\mathrm{eff},z} \\ a_x \\ a_y \\ a_z \end{bmatrix} = \begin{bmatrix} \boldsymbol{v}_{\mathrm{eff}} \\ \boldsymbol{a} \end{bmatrix}. \tag{3.9}$$

The effective velocity, $\boldsymbol{v}_{\mathrm{eff}} = [v_{\mathrm{eff},x}, v_{\mathrm{eff},y}, v_{\mathrm{eff},z}]$ accounts for the actual velocity of the particle plus effects due to the spatially varying density and diffusivity throughout the disk (see F. J. Ciesla, 2010, 2011),

$$\boldsymbol{v}_{\rm eff} = \boldsymbol{v} + \frac{D(\boldsymbol{x})}{\rho_g(\boldsymbol{x})}\boldsymbol{\nabla}\rho_g(\boldsymbol{x}) + \boldsymbol{\nabla}D(\boldsymbol{x}). \tag{3.10}$$

The acceleration, $\boldsymbol{a} = [a_x, a_y, a_z]$, is determined from the gravity due to the planet, gravity from the central star, drag with the surrounding gas, and the centripetal acceleration in the rotating frame. That is, the total acceleration of the particle is

$$\boldsymbol{a} = \boldsymbol{a}_{\rm grav} + \boldsymbol{a}_{\rm grav,pl} + \boldsymbol{a}_{\rm drag} + \boldsymbol{a}_{\rm rot}. \tag{3.11}$$

Tracer particles do not interact with one another, nor do we account for back reactions of the dust on the gas.

The gravitational acceleration due to the central star is given by:

$$\boldsymbol{a}_{\rm grav} = -\frac{GM_\star}{|\boldsymbol{x}-\boldsymbol{x}_\star|^3}(\boldsymbol{x}-\boldsymbol{x}_\star), \tag{3.12}$$

and the gravitational acceleration from the planet is:

$$\boldsymbol{a}_{\rm grav,pl} = -\frac{GM_{\rm pl}}{|\boldsymbol{x}-\boldsymbol{x}_{\rm pl}|^3}(\boldsymbol{x}-\boldsymbol{x}_{\rm pl}), \tag{3.13}$$

where $M_\star$ and $\boldsymbol{x}_\star$ are the mass and position of the central star, and $M_{\rm pl}$ and $\boldsymbol{x}_{\rm pl}$ are the mass and position of the planet respectively.

The drag acceleration of the particle is determined following the methodology of T. Tanigawa et al. (2014):

$$\boldsymbol{a}_{\rm drag} = \frac{\boldsymbol{F}_{\rm drag}}{m} = -\frac{(C_D/2)\pi s^2\rho_g|\boldsymbol{u}|\boldsymbol{u}}{(4/3)\pi s^3\rho_s}, \tag{3.14}$$

where C_D is the drag coefficient, ρ_g is the local gas density, $\boldsymbol{u} = \boldsymbol{v} - \boldsymbol{v}_{\rm gas}$ is the relative velocity of the particle, and m is the mass of the particle.

Equation 3.14 simplifies to the following form:

$$\boldsymbol{a}_{\rm drag} = -\frac{3}{8}\frac{C_D}{s}\frac{\rho_g}{\rho_s}|\boldsymbol{u}|\boldsymbol{u}. \tag{3.15}$$

In the Epstein drag regime, which we use for all cases as the particle sizes are less than the mean free path in the gas, this is further simplified to:

$$\boldsymbol{a}_{\text{drag}} = -\frac{\rho_g c_s}{\rho_s s}\boldsymbol{u} = -\frac{\boldsymbol{u}}{t_{\text{stop}}}. \tag{3.16}$$

Finally, the acceleration due to rotation, including the Coriolis and centrifugal forces is given by

$$\boldsymbol{a}_{\text{rot}} = -2\boldsymbol{\Omega}_f \times \boldsymbol{v} - \boldsymbol{\Omega}_f \times (\boldsymbol{\Omega}_f \times \boldsymbol{x}) \tag{3.17}$$

or, in expanded vector notation

$$\boldsymbol{a}_{\text{rot}} = \begin{bmatrix} 2v_y\Omega_f + x\Omega_f^2 \\ -2v_x\Omega_f + y\Omega_f^2 \\ 0 \end{bmatrix} \tag{3.18}$$

where the $\boldsymbol{\Omega}_f = [0, 0, \Omega_f]$ is the rotation rate of the frame.

While particles are integrated forward in time, their positions, velocities, and Stokes numbers are recorded at each timestep. If particles leave the bounds of the mesh (i.e. drift to the inner edge or are lofted such that their polar angle exceeds $\pi/2 \pm 0.15$), they are removed from the simulation. Additionally, any particles that pass within the planetary envelope are considered accreted by the planet, and removed from the simulation. Following J. Chambers (2017) and M. N. Barnett & F. J. Ciesla (2022), the planetary envelope radius is given by

$$r_{\text{env}} = \min\left[\frac{r_{\text{Hill}}}{4}, r_{\text{Bondi}}\right] \tag{3.19}$$

where $r_{\text{Hill}} = a_{pl}(M_{pl}/3M)^{1/3}$ is the Hill radius of the planet and $r_{\text{Bondi}} = 2GM_{pl}/c_s^2$ is the Bondi radius of the planet.

We use a Runge-Kutta 4$^{\text{th}}$ order method for integration, with the timestep, Δt, chosen to ensure numerical stability. The timestep is defined as

$$\Delta t = \min(0.1 \text{ yr}, \Delta t_{\text{orbit}}, \Delta t_{\text{drag}}, \Delta t_{\text{diff}}, \Delta t_{\text{rho}}) \tag{3.20}$$

where

$$\Delta t_{\rm orbit} = \eta \frac{2\pi}{\Omega_K}, \tag{3.21}$$

$$\Delta t_{\rm diff} = \xi \frac{|\boldsymbol{x}|}{|\boldsymbol{\nabla} D|}, \tag{3.22}$$

$$\Delta t_{\rm rho} = \zeta \frac{\rho_g}{D} \frac{|\boldsymbol{x}|}{|\boldsymbol{\nabla} \rho_g|}. \tag{3.23}$$

Here, each expression represents a step-size limit to ensure numerical stability. In $\Delta t_{\rm orbit}$, we limit the timestep to be a sufficiently small fraction, $\eta = 1/50$, of the orbit, to account for changes in v_x and v_y with location. Additionally, we limit the step size of the particle during the integration dependent on the components of the effective velocity, where $\Delta t_{\rm diff}$ and $\Delta t_{\rm rho}$ are based on the diffusive terms of the effective velocity in equation (3.10). We also include an upper limit of 0.1 yr in all cases, to prevent unphysical displacement due to turbulence, even in smooth regions of the disk. The coefficients ξ and ζ in $\Delta t_{\rm diff}$ and $\Delta t_{\rm rho}$ are chosen to be 10^{-6} and 10^{-5} respectively to ensure these timesteps remain small relative to the stopping time of moderately coupled solids. As the effective velocity of the particle depends on $\boldsymbol{\nabla} \rho_g$ and $\boldsymbol{\nabla} D$, the timestep of the integration is decreased where the magnitude of these values is large. This ensures particles only move small distances in a given timestep when in regions of sharp density or diffusivity gradients. This was tested using values of ξ and ζ an order of magnitude smaller and there was no significant difference to the integration results.

In testing, we found that particles with Stokes number less than about 10^{-3} were always strongly coupled to the gas, that is, $\boldsymbol{u} \approx 0$. However, these particles tended to have long integration times as $t_{\rm stop}$ was small, limiting Δt. To allow for reasonable integration times, we use an adjusted $\Delta t_{\rm drag}$ in equation (3.20). The adjusted $\Delta t_{\rm drag}$ is given by the equation

$$\Delta t_{\rm drag} = \frac{t_{\rm stop}}{\sigma(\log_{10}{\rm St})} = \frac{s\rho_s}{c_s \rho_g} \frac{1}{\sigma(\log_{10}{\rm St})}, \tag{3.24}$$

where σ is a sigmoid function centered at -3

$$\sigma(x) = \frac{1}{1 + e^{-(x+3)}}. \tag{3.25}$$

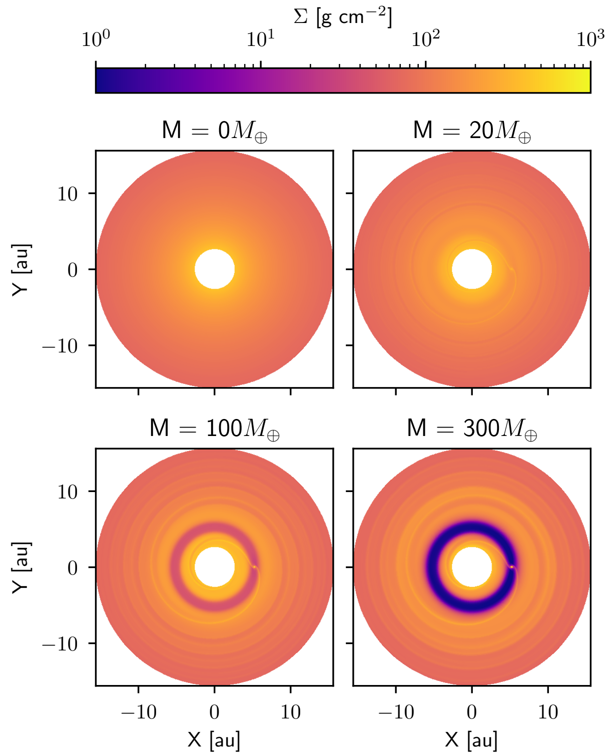

Figure 3.1: Surface density maps for FARGO3D simulations containing embedded planets of mass 0 (no planet), 20, 100, and 300 $M_\oplus$. Results are shown in the co-rotating frame with the planet, with the planet located at $x = 5.2$ au and the central star at the origin. At 20 $M_\oplus$ a small gap can be seen, although the planet has not yet reached the pebble isolation mass. At 100 and 300 $M_\oplus$, the co-rotating spiral arms can be seen coming off the planet, with density perturbations from the initial surface density increasing with embryo mass.

Thus, for particles with Stokes number greater than 10^{-3}, $\Delta t_{\rm drag} \approx t_{\rm stop}$. Alternatively, for particles with Stokes number much less than 10^{-3}, $\Delta t_{\rm drag}$ is large and integration steps can be much longer as particles follow the flow of the gas. When a particle's Stokes number is less than 10^{-3}, the drag force is assumed to be zero and the particle velocity is set to the same as the surrounding gas, that is, $\boldsymbol{v} = \boldsymbol{v}_{\rm gas}$. We tested different limits of this coupling Stokes number, and found no significant difference in results when this value was lowered by an order of magnitude.

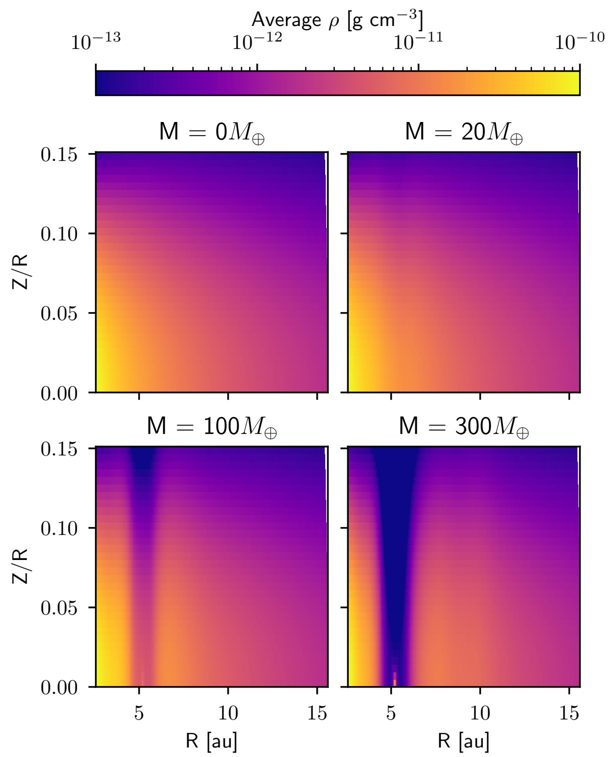

Figure 3.2: Azimuthally averaged densities for the same set of embedded planets as Figure 3.1. The density is averaged over the full disk, $\phi \in [-\pi, \pi]$. The gap opened by the planet extends from the midplane ($Z/R = 0$) to the upper layers of the disk. The dense planetary embryo can be seen at the location of the planet.

3.4 Results

3.4.1 Hydrodynamic Simulations

The results of the FARGO3D simulations for several embedded planet masses are shown in Figures 3.1 and 3.2. The results shown here and in the following sections are using the fiducial disk viscosity of $\alpha = 10^{-3}$; we discuss the effects of lowering disk viscosity in Section 3.4.5. The gap opened by the planet and spiral arm structure can be seen in the figures. As in previous studies (e.g. K. D. Kanagawa et al., 2016; J. Fung & E. Chiang, 2016; P. C. Duffell, 2020), the gap grows wider and deeper for more massive planets and with disk decreasing viscosity.

Figure 3.3 shows the azimuthally averaged deviation from Keplerian velocity and surface density depletion relative to the initial disk that develops as a result of the planet-disk interactions. In our model with $\alpha = 10^{-3}$, a planet mass $\gtrsim 30M_\oplus$ is necessary for gas velocities to reach Keplerian at the pressure maximum exterior to the planet, in good agreement with typical pebble isolation masses in the solar nebula found in other studies (M. Lambrechts et al., 2014; B. Bitsch et al., 2018). Here, we define the gap as the region of the disk where the azimuthally averaged surface density is depleted by at least 50%. While planetary masses greater than or equal to $30M_\oplus$ are required to deplete the gas by more than 50% to create a gap, we note that the gas is still depleted around the planet for smaller embryo masses, just not to a sufficient level to halt the inward drift of solids. The location of the gap edge is highlighted in Figure 3.3. In our simulations, we find that gap width, scales as $M_{pl}^{1/2}$ as in other studies (e.g. P. C. Duffell, 2015; K. D. Kanagawa et al., 2015, 2016; P. C. Duffell, 2020).

The gas density and velocity around the embryo for three simulations with the largest masses, 100, 200, and 300 $M_\oplus$, are shown in Figure 3.4. As the mass of the planet grows, the strength of the advective flows in the disk increase, with clear meridional flow circulation patterns developing around the embedded embryos. This outward flow can be seen along the spiral arms in the left side of Figure 3.4, and at the midplane near the planet in the right column. The increased strength of these flows outward along the midplane result in both faster gas velocities and a greater radial extent of the transport of material away from the planet, in agreement with previous 3D studies of embedded disks (e.g. A. Morbidelli et al., 2014; J. Fung & E. Chiang, 2016; J. Szulágyi et al., 2022;

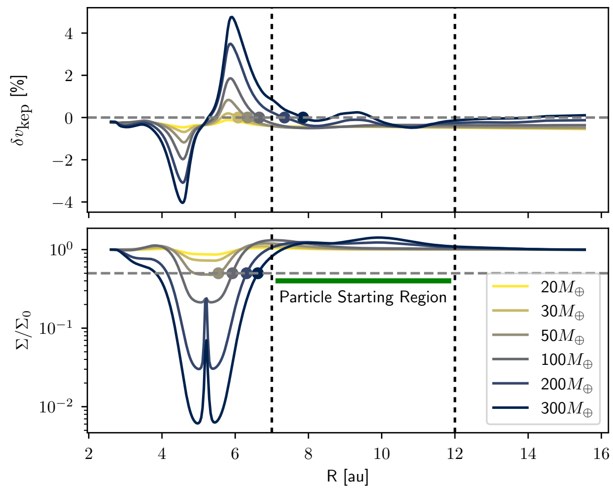

Figure 3.3: Azimuthally averaged midplane azimuthal velocity (*top*) and surface density relative to a disk with no planet (*bottom*). The azimuthal velocity is given as percent deviation from keplerian, $\delta v_{\rm kep} = (v_\phi - v_{\rm kep})/v_{\rm kep}$, and the horizontal dashed line is at $\delta v_{\rm kep} = 0\%$. In the bottom panel, the gap edge is defined as where $\Sigma/\Sigma_0 = 0.5$. The region where we start particles in our simulation is shown between the two vertical dotted lines at 7 and 12 au, chosen to be outside the gap for all planet masses considered.

L. Krapp et al., 2022).

3.4.2 Particle Crossing From Outer Nebula to Inner Nebula

In the absence of any planet, the transport of mm- to cm-sized solid particles is largely dominated by inward drift due to gas drag (e.g. S. J. Weidenschilling, 1977). As the growing embryo opens a gap in the nebula, the inward drift of solids can be halted in the resulting pressure bump. However, as has been shown in previous 2D simulations (e.g. P. Weber et al., 2018; T. Haugbølle et al., 2019) small particles (< 1 mm) can filter past Jupiter-mass embedded embryos, replenishing the inner nebula with solids. Here, we consider particle movement in 3D to understand the details of these motions in the presence of an embedded planet.

To explore the trajectories of these crossing particles and identify the size and provenance of such grains, we track the evolution of different sized particles that begin evenly distributed in the 7 to 12 au region through all disks considered here. We consider the outer disk to be the region exterior the orbit of the embryo at 5.2 au, and the inner disk the region interior to the orbit of the embryo. We choose this initial location for the particles as it is just exterior to the gap opened by

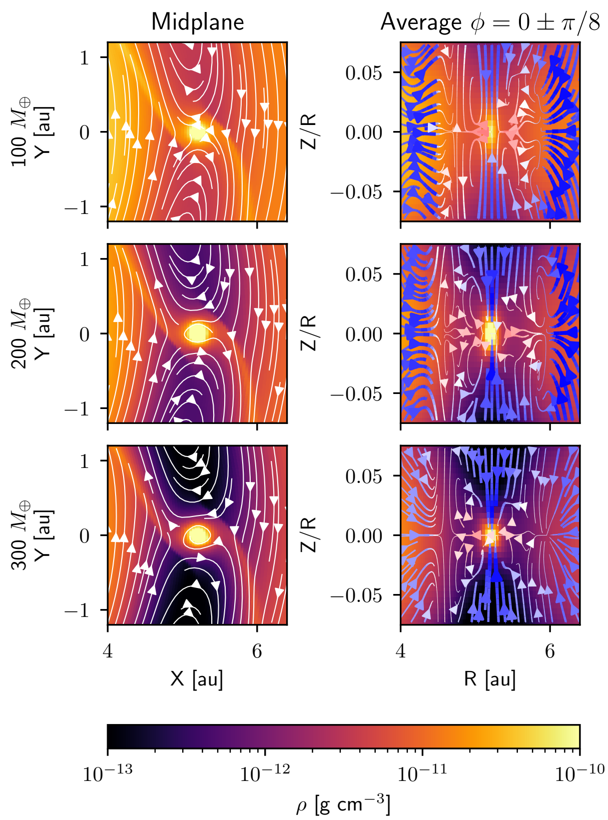

Figure 3.4: Results of FARGO3D simulation of disks containing a 100, 200, and 300 $M_\oplus$ (top to bottom) embedded planet showing the gas density and velocity. The left panels show the Cartesian midplane gas structure of the disk. The right panels show the radial and vertical gas density and gas advection near the planet, averaged over $\phi = 0 \pm \pi/8$. Here, the arrow color corresponds to the advection of the gas relative to the planet, with blue indicating flows towards the planet and red away. As the planetary embryo grows, the magnitude of the gas advection velocities grow while the width and depth of the gap deepens.

the 300 $M_\oplus$ embryo, the most massive planet and widest gap considered (see Figure 3.3).

Sample trajectories of particles of different sizes for a variety of embryo masses are plotted in Figure 3.5, showing the radial movement of 20 illustrative particles over their 100 kyr integration time. As can be seen, the efficiency at which particles move from the outer disk to the inner disk depends on both grain size and embryo mass. Below the pebble isolation mass ($< 30M_\oplus$) the planetary embryo does not create an effective pressure bump outside of its orbit, allowing the 1 cm size particles to efficiently drift from the outer disk to inner disk. Smaller particles are well coupled with gas and have much longer drift timescales, and thus do not significantly drift inward over the 100 kyr simulated here; and instead their dynamics are dominated by diffusion. Once the embryo is massive enough, inward drift is halted for all particles larger than 1 mm in size.

However, once the planetary embryo reaches $\gtrsim$ 100 $M_\oplus$, the mass corresponding to the runaway accretion phase of giant planet formation (R. Helled et al., 2022), particles smaller than 100 µm that are well coupled to these strong advective flows can pass the orbit of the embedded embryo. The path of a 10 µm sized particle that moves past a 100 $M_\oplus$ embryo is shown in Figure 3.6. At the first time shown, the particle is exterior to the planet and approximately one scale height away from the midplane. Here, the gas advection is towards the planet, pushing the particle both inward and downward. The particle passes nearby the planet, $\sim 200R_{\rm Jup}$ or about $1.5r_{\rm env}$, before moving to an orbit interior to the planet. Although the flow of gas at the midplane near the embryo is outward, if the solids diffuse to a high enough elevation, they can be entrained in the inward flowing gas. This favors crossing for small particles or disks with high α.

To explore the fraction of solids able to cross the planet, we extend the integration of 1000 particles starting at 7 au to 1 Myr. We note here that over 1 Myr timescales, our assumptions that the disk structure and planet mass remain constant likely break down. However, the results presented here still give us a good insight to the total crossing efficiency for dust grains. While the fraction of solids crossing depends on time, shown in Figure 3.7, we give the final fraction of solids that cross the orbit of the planet in Figure 3.8. In each figure, we show the fraction particles simulated that are either accreted by the protoplanet or cross from the outer disk to the inner disk. We also show the fraction particles that leave the bounds of our simulation, either by diffusing outward to the maximum radius of the simulation or by diffusing above or below $\pi/2 \pm 0.15$ in

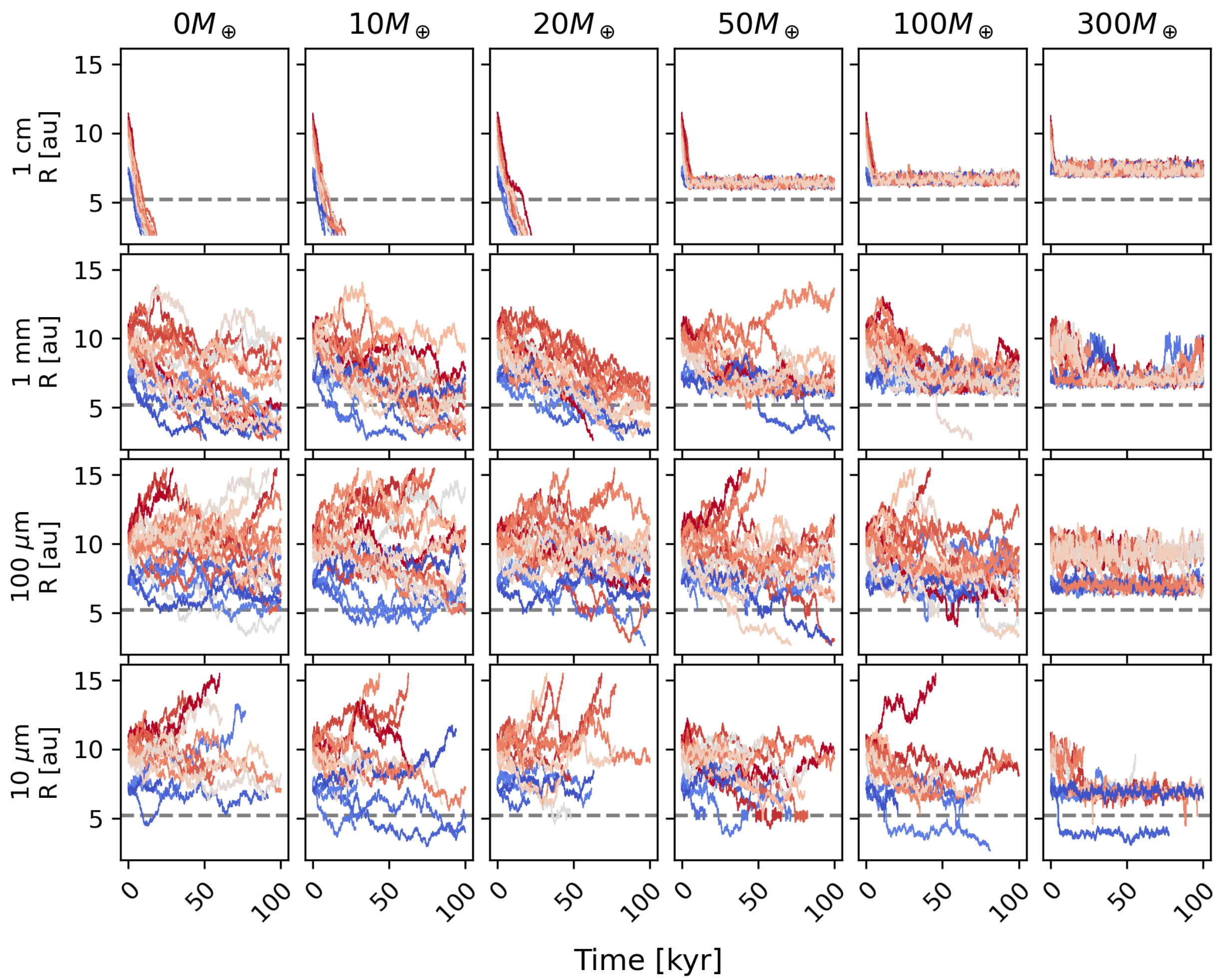

Figure 3.5: A selection of particle trajectories, showing the radial location of 20 particles as a function of time. Each subplot represents the evolution of particles in a disk containing different mass planetary embryos (columns) and different size grains (rows). Each line is colored according to the particle's initial location, ranging from 7 to 12 au, with bluer lines representing particles starting at 7 au and redder lines showing particles starting at 12 au. The location of the planet at 5.2 au is marked in each subplot by the horizontal dashed line. Broadly, large grains with in disks containing small embryo masses efficiently drift from the outer disk to the inner disk, while this inward drift is halted above the pebble isolation mass. Small particles may cross the planetary for large planetary embryo masses as a result of strong advection, either bringing the solids into the gap in a horseshoe orbit, to be accreted, or past the gap into the inner disk. In cases where particles do not survive for the full 100 kyr, they may be accreted onto the planet or diffuse outside of the domain of the simulation.

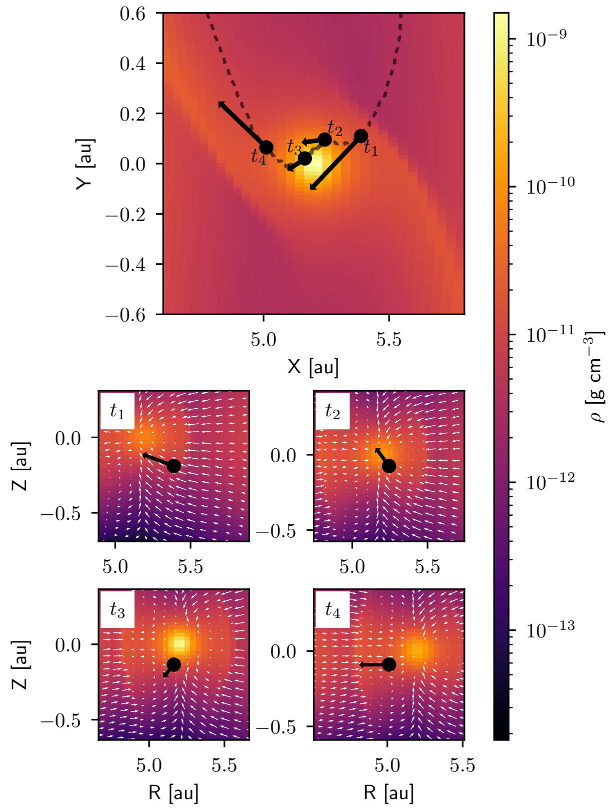

Figure 3.6: An example trajectory of a solid particle that crosses from the outer disk to the inner disk. The top panel shows the path followed by the particle as the black dashed line projected onto the midplane of the disk, with 4 locations and particle velocities labeled. The particle velocity and surrounding gas density and advection in the R-Z plane is shown below for each of the highlighted times in the top panel. For this particle, the inward advecting gas pulls the solid particle towards the planet (t_1 and t_2) following the meridional flow. The particle comes close to the planet, but remains outside of the accretion envelope (t_3). Then, the particle follows the outward meridional flow along the midplane to the inner disk (t_4).

polar angle, the upper and lower bounds of our simulation. For the 10 and 100 µm particles where particles diffuse out of bounds in the no planet case, additional particles are integrated for each planet mass until 1000 total particles drift inwards of 5.2 au by 1 Myr. Consistent with previous work, we find that while the planetary embryo is less about 30 $M_{\oplus}$, particles larger than 1 mm drift inward past the growing protoplanet, while smaller particles tend to stay in the outer nebula for longer times, with about 30% eventually diffusing inward. For more massive embryos, the larger particles are entirely trapped at the pressure bump exterior to the planet due to the local pressure maximum. However, up to 30% of particles smaller than 100 µm filter from the outer disk to the inner disk by 1 Myr, slightly increasing the crossing efficiency of these small particles as the planet grows.

At more massive embryo masses, small particles cross at higher efficiency than than low mass embryos because larger embryo masses drive stronger advective flows around the embryo (Figure 3.4). Small particles are well coupled to the gas and follow this advective flow past the embryo and across the gap. As such, the meridional flows onto the embedded planet increase the relative crossing rate of these small particles. Note that at the largest planetary embryo only the smallest 10 µm sized dust crosses the orbit of the planet. This is due to the increasing depth and width of the gas gap surrounding the planet. As the gas density around the embryo decreases, particle stokes numbers increase, such that only the smallest dust remains well coupled with the gas to follow the gas flows through the gap. Larger dust decouples from the gas before crossing into the gap.

We also find that a fraction of solids pass within the planetary envelope, given in equation 3.19, meaning they are accreted by the planet. While the planet is below the pebble isolation mass, approximately 1 to 10% of millimeter and centimeter sized pebbles are accreted, dependent on grain size and embryo mass, consistent with previous theoretical and modeling work on pebble accretion (C. W. Ormel & B. Liu, 2018; B. Liu & C. W. Ormel, 2018; J. Drążkowska et al., 2021; M. N. Barnett & F. J. Ciesla, 2022). Above the pebble isolation mass, the accreted solids come from the population of small dust in the disk, as these solids follow the meridional flow away from the midplane and onto the planet at higher altitudes. These results are supported by the findings of J. Szulágyi et al. (2022) and N. Maeda et al. (2024), which show the primary accretion of material to an embedded giant embryo occurs through accretion of small dust at the polar regions of the

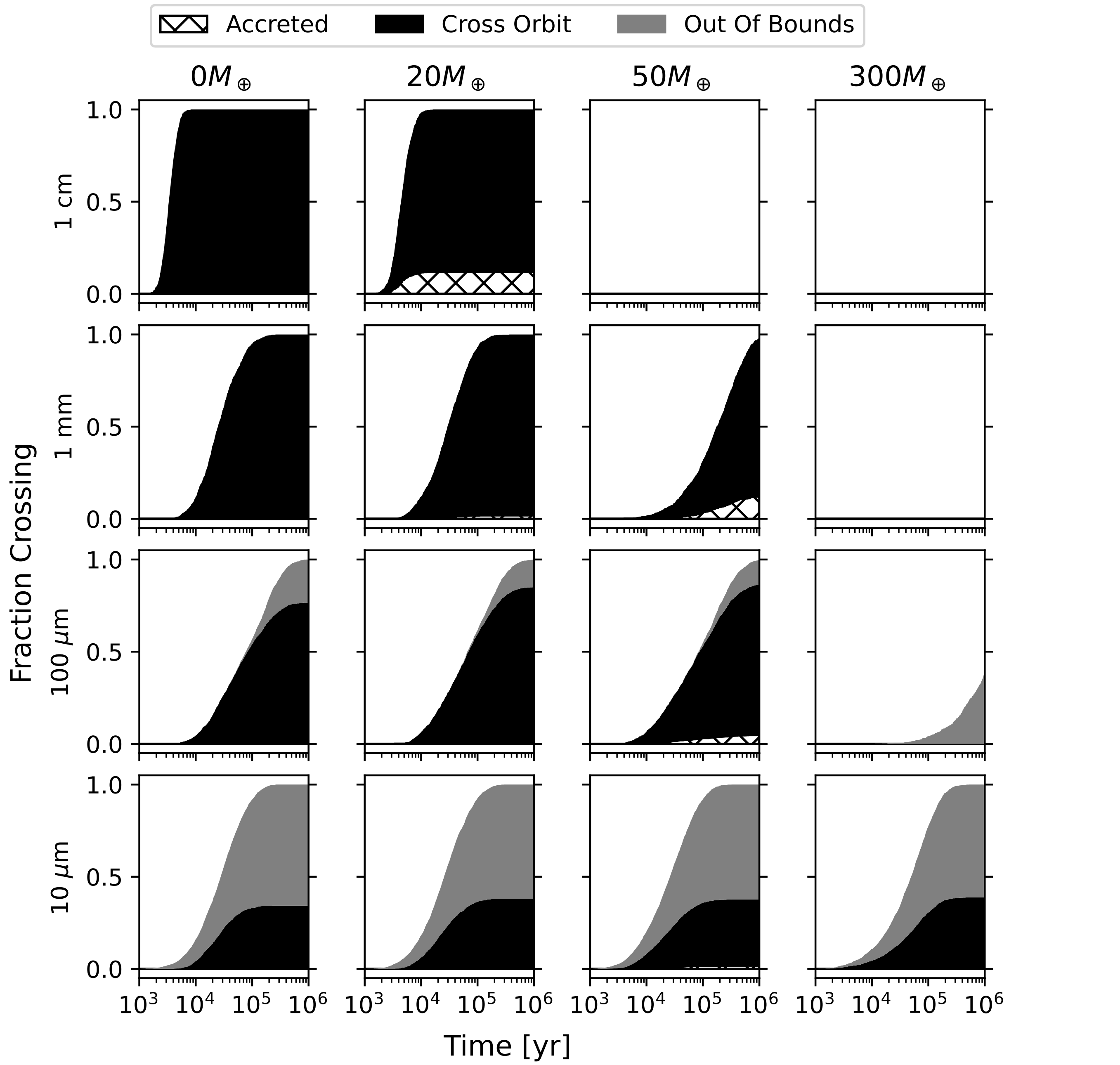

Figure 3.7: The fraction of solids starting at 7 au that cross the orbit of the planet. For the 1 cm and 1 mm sized pebbles, drift across the orbit of the planet occurs over longer timescales as the planet mass increases. Some grains are lost to accretion onto the planet, indicated by the cross hatched regions. Other grains diffuse outside of the domain of the integration, and are shown by the light gray region of the plots. For the smaller 100 and 10 μm sized dust, which is well coupled to the gas, the fraction crossing increases with increasing planet mass. This is because the larger embryo creates advective flows through the gap, carrying the small dust with the gas. The final percentages for each planet mass and grain size are shown in Figure 3.8.

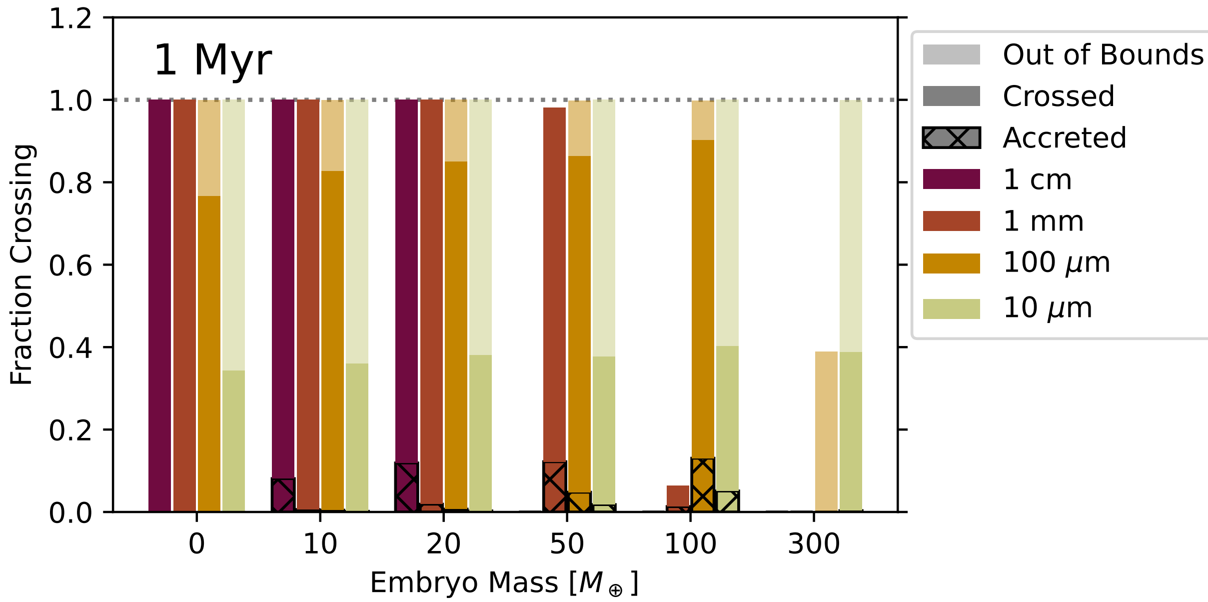

Figure 3.8: Of solids initialized at 7 au (the same population as shown in Figure 3.7), we show the fraction of particles either accreted by the planet or crossing the orbit of the planet after 1 Myr of integration. While the planet is below the pebble isolation mass, the fraction of 1 cm particles crossing the orbit of the planet is near unity, with up to $\sim 10\%$ accreted by the planet, as their dynamics are primarily driven by inward drift over the timescale of the integration. Smaller particles have much lower crossing fractions until the mass of the planet grows to facilitate advection mediated crossing. A fraction of these crossing solids are accreted by the planetary embryo, as they follow gas streamlines onto the accreting planet.

embryo. Thus a growing Jovian-like planet regulates what solids it can accrete as it grows.

3.4.3 Outward Transport of Solids

Thus far we have focused on inward transport through the disk and across the planet's orbit, but outward transport of dust can occur as well. To investigate the importance of such movement we simulated the trajectories of 1 cm and 10 µm sized grains (the largest and smallest sizes considered here) that originate in the range of 3.0 to 4.2 au and 6.2 to 7.4 au, considering particles that begin both inside and outside of the planetary embryo. While this ensures no particles begin within 1 au of the embryo, and thus outside the planetary envelope, some particles do begin in the gap opened by the most massive embryo. Such dust could be generated by collisions of dust aggregates or planetesimals present at these locations. We also choose to focus only on embryo masses above the pebble isolation mass, as this is where we expect the accretion flow mediated transport of small dust to be most prevalent.

The initial radial locations of each particle and their positions after 100 kyr of evolution are shown in Figure 3.9. In the outer disk, 1 cm sized particles for each planet largely clump together at the pressure maxima where the gas flow is Keplerian. Particles of this size that start in the inner disk drift to the inner edge of the disk, and are removed from the simulation. The dynamics of these grains are largely dominated by gas drag induced drift. No cm sized grains cross the orbit of the planet for the embryo masses considered here.

The smaller, 10 µm grains, shown in the bottom row of Figure 3.9, behave quite differently. For all embryo masses considered, the vast majority of small dust particles survive in the inner disk for the full 100 kyr due to their much longer drift timescales compared to the larger 1 cm size particles. In general, these smaller particles are dominated by diffusion rather than drift and tend to spread out through the disk rather than concentrate at a single location. These solids are much more likely to cross the orbit of the growing planetary embryo in both directions, both moving inward from beyond the orbit of the planet as discussed above, but also outward from the inner disk to the outer disk. This effect can also be seen in 3.5, where 10 and 100 µm sized grains can be seen to move between the inner and outer disk even in the presence of a 100 $M_\oplus$ embryo. Thus, we find that some amount of small solids can be transported from the inner disk to the outer disk throughout the

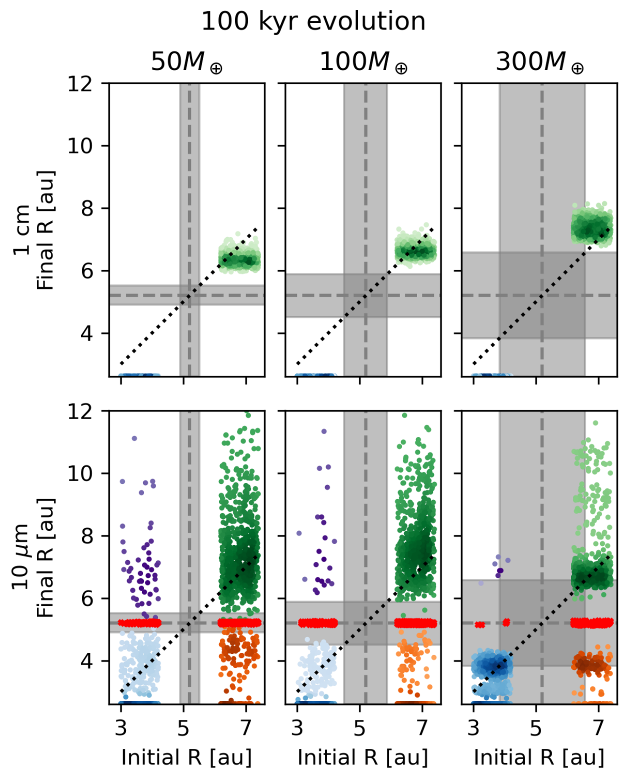

Figure 3.9: The starting and ending locations of solid particles that begin both inside and outside of the planet after 100 kyr of evolution. The planet location is shown by dashed grey lines, with the gap shown by the thick grey regions. A 1:1 line is shown by the black dotted line. Particles above this line moved outward in the nebula, while particles below this line moved inward. Points are colored according to the quadrant they are in, with darker colors indicated a higher density of points in that region of space. The upper right quadrant of each subfigure represents solids that start and end in the outer disk, while the bottom left are solids that start and end in the inner disk. The upper left and lower right quadrants show material that crosses the orbit of the planet, from the inside out or outside in respectively. Points in red show solids that are accreted by the planetary embryo.

growth of the embedded embryo resulting in additional mixing of materials across the gap opened by the embryo.

As expected, the 1 cm particles tend to concentrate at the pressure bump where the solids move at the same speed as the gas resulting in no drag. These locations are at about 6.5, 7, and 8 au for the 50, 100 and 300 $M_\oplus$ cases respectively (see Figure 3.3). In the outer nebula, the smaller solids show a much wider distribution for the 50 and 100 $M_\oplus$ cases, although tend to concentrate at the gap edge for the 300 $M_\oplus$ case. This concentration of 10 µm dust is due to the increased strength in gas flow due to gravitational interactions between gas and the massive embedded embryo. These dust concentration points are discussed in more detail in Section 3.4.4. Interestingly, these 10 µm solids also tend to concentrate at the inner gap edge, at about 4 au. At this location, the gas azimuthal velocity approaches Keplerian, although it is still slightly sub-Keplerian (see Figure 3.3). Additionally, at the gap edge, gas is flowing into the gap, radially outward at the inner gap edge. Because the gas is relatively depleted at this point in the disk, the small dust has a larger Stokes number than in the outer disk. As such, the dust do not diffuse as readily away from this region as would be expected in an unperturbed case. Combined, these effects result in a low radial velocity for the small dust, leading to an increase in concentration of small dust at the inner edge of the gap in addition to the outer edge.

3.4.4 Dust Concentration Points

In the limit of many particles over long timescales, the residence times of the particles mirror the spatial density of particles at a given location. These regions of high dust concentration (long residence times) may be important growth regions, as the resulting elevated dust-to-gas ratios may lead to more frequent collisions (T. Birnstiel et al., 2012) and/or the initiation of the streaming instability (A. N. Youdin & J. Goodman, 2005; A. Johansen et al., 2007).

The average residence time of a particle between radial location R_j and R_{j+1}, where R_j is the inner bin edge, is given by

$$\tau_{res}(R_j) = \frac{1}{N_{part}} \sum_{i=0}^{N_{part}} \Delta t_i \delta(r_i), \tag{3.26}$$

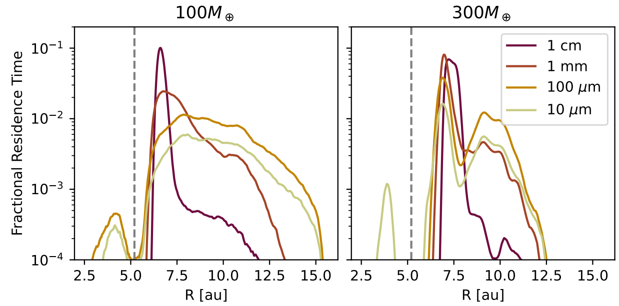

Figure 3.10: Average residence time for different sizes of solids as a function of radial location in the disk. Residence times are shown for disks containing planetary embryos of mass 100 $M_\oplus$ (left) and 300 $M_\oplus$ (right). For particles smaller than 1 mm, residence times show a two peaked distribution in the outer disk when $M = 300\ M_\oplus$, but a smooth, single peaked distribution when $M = 100\ M_\oplus$. The location of the planet at 5.2 au is indicated by the vertical dashed line in both plots. Thus, solids may form two distinct rings outside of the planet when the embedded Jovian embryo is massive enough.

where N_{part} is the number of particles, Δt_i is the timestep of the integration, r_i is the particle location at the start of the timestep, and

$$\delta(r_i) = \begin{cases} 1, & \text{if } R_j < r_i < R_{j+1} \\ 0, & \text{else} \end{cases} . \tag{3.27}$$

This can also be expanded to 2 or 3D residence times in Cartesian or spherical coordinates. The residence time in a given cell in the RZ plane is given by

$$\tau_{res}(R_j, Z_k) = \frac{1}{N_{part}} \sum_{i=0}^{N_{part}} \Delta t_i \delta(r_i)\delta(z_i), \tag{3.28}$$

where $\delta(z_i)$ is defined similarly to $\delta(r_i)$ for a z-coordinate with bin edges at Z_k and Z_{k+1}. These residence times are then normalized to the total integration time to give the fractional residence time.

We use the same bins for the residence times as are used for the FARGO3D mesh. The radial residence times for the different sizes of particles considered for planetary embryo masses of 100 and 300 $M_\oplus$ are shown in Figure 3.10. We use the same population of particles from Section 3.4.2, that is, solids initialized between 7 to 12 au over 100 kyr.

In both cases, 1 cm size particles tend to pile up in a narrow region just outside of the gap opened by the embryo, while the solids less than 1 mm in size are more spread out through the outer disk. While the smaller solids have a single peak distribution for the planetary embryo of 100 $M_\oplus$ around 7 au, the 300 $M_\oplus$ embryo creates a bimodal distribution of the small solids in the outer disk. This can be seen in the right panel of Figure 3.10, with a sharp peak in residence time at about 7 au for all particles, (although the smaller particles tend to have their longest residence times closer to the planet). The solids smaller than 1 cm then also have a secondary broad peak centered at 10 au. The massive planetary embryo creates global substructures throughout the disk, which can create concentric rings and gaps, as has been inferred for disks around other stars (D. Fedele et al., 2018; S. Pérez et al., 2019). As such, a single giant planet may create multiple dust pileups in a single disk, explaining the observation of multiple ring and gap systems in other protoplanetary disks.

As shown in Figure 3.3, for embryo masses $30M_\oplus \geq M_{\rm pl} < 100M_\oplus$, the azimuthal gas velocity is exactly Keplerian in only one location, corresponding to the pressure bump outside of the gap opened by the planet. But when $M_{\rm pl} \gtrsim 200M_\oplus$, there are multiple locations where $\delta v_{\rm Kep} = 0$, and two locations where particles may concentrate. For a roughly Jupiter mass embryo of $300M_\oplus$, these locations are at about 7.5 au, and 10 au.

We note that in the higher turbulence case shown here ($\alpha = 10^{-3}$), the outer pressure bump is not sufficient to trap the largest centimeter sized dust. However, smaller dust is more efficiently trapped in this outer pressure bump. This is because the larger dust is more vertically settled, and the dynamics are driven primarily by drift through the midplane of the disk (see also C. P. Dullemond et al., 2018). Thus, given the turbulence of the disk, a small diffusive "kick" can free the larger pebbles from the region where the gas velocity is Keplerian, and they rapidly drift inward. The smaller dust, on the other hand, is more vertically distributed and concentrates where the gas radial velocity is low or slightly outwards (offsetting inward drift). The small dust is much more sensitive to the radial gas advection not just along the midplane, but also up to a few scale heights in the disk.

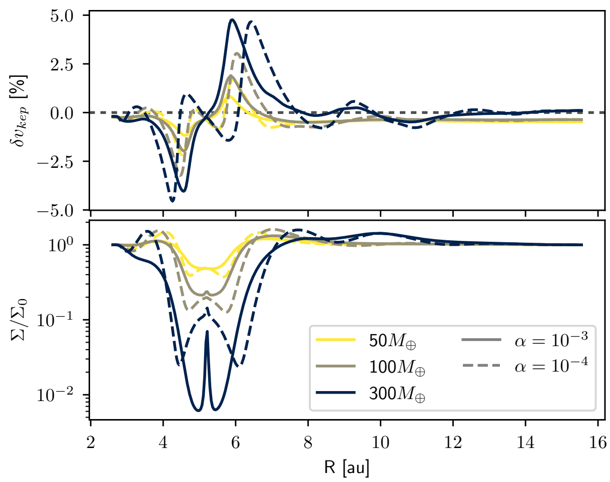

Figure 3.11: Comparison of azimuthally averaged disk structure for $\alpha = 10^{-3}$ (solid lines) and 10^{-4} (dashed lines). In general, gaps in disks with lower α values are both deeper and wider. In both cases, variations in the density remain in the outer disk, leading to multiple areas in the disks where azimuthal velocity is Keplerian. We note that while the region around the planet in the lower viscosity case always has lower density compared to the higher viscosity case, The 300 $M_\oplus$, case does not fully clear all of the gas from the gap in the timescales considered. The gas present in the gap is primarily opposite the planet (that is, $\phi = \pm\pi$). As particles crossing the orbit of the planet generally do so at the location of the planet, this gas present in the gap does not affect the crossing of particles.

3.4.5 Dependence on Disk Viscosity

Although the level of turbulence in disks is uncertain, observations of PPDs have shown that turbulence can generally be modelled using an α-disk approximation with $\alpha \approx 10^{-3} - 10^{-4}$ (e.g. K. Doi, 2021; K. Flaherty et al., 2020, 2024; T. Paneque-Carreño et al., 2024). Here, we also explore a lower viscosity disk (i.e. lower turbulence) with $\alpha = 10^{-4}$. The lower viscosity affects the particle trajectories in two major ways. First, planets open deeper and wider gaps in the disk, as has been described in analytic and numerical studies (e.g. P. C. Duffell, 2015; K. D. Kanagawa et al., 2015, 2016). The resulting azimuthally averaged gas structure of these $\alpha = 10^{-4}$ disks are shown compared to the fiducial $\alpha = 10^{-3}$ disks in Figure 3.11. Second, the diffusivity of the particles is also decreased, as the particle diffusivity is proportional to the gas viscosity (Equation (3.6)).

The resulting trajectories of several particle integrations using $\alpha = 10^{-4}$ are shown in Figure 3.12. Here, similar to as in Section 3.4.2, we focus on solids in the outer disk. As can be seen, the lowered viscosity results in much less solid material crossing the orbit of the embedded embryo. This finding is consistent with previous 2D models, which have shown the fraction of material crossing the gap opened by the planet decreases as the gas viscosity decreases (P. Weber et al., 2018; T. Haugbølle et al., 2019). This is because the gas density at the edge of the gap is much lower than the $\alpha = 10^{-3}$ case with a steeper density gradient, and so the grains decouple from the gas and no longer follow the gas advection across the gap. These solids are also unable to diffuse closer to the planet, where the gas advection and gravitational interactions may pull the solids towards the inner disk, as in the $\alpha = 10^{-3}$ cases.

Another feature of the lower viscosity cases is that the solids tend to concentrate at multiple locations at lower embryo masses when compared to the higher $\alpha = 10^{-3}$ case. The lower viscosity leads to less damping of density and velocity perturbations in the outer disk, resulting in more pronounced substructure, as seen in the disk's azimuthal velocity and density shown in Figure 3.11. As a result, there are several regions of the disk that are at or near Keplerian velocity, leading to multiple pileups of all solids, including the drift-dominated, 1 cm size solids. Small dust that is well-coupled to the gas can also concentrate away from the midplane, as seen in Figure 3.13, leading to concentrations of the smaller 10 and 100 µm dust. In lower viscosity disks, the embedded embryo can create large scale gas advection throughout the disk, with gas moving away from the midplane and through the upper layers of the disk. For sufficiently small solids, they can become well entrained with these flows and concentrate at the center of these 3D gas circulation patterns, as shown by the regions of longer residence time in the lower right plot in Figure 3.13. Additionally, due to the lower particle diffusivity, the solids cannot easily diffuse away from these regions, and thus remain much more concentrated in space over the length of the particle integration.

3.5 Discussion

Given our results, we now explore how the growth of a giant embedded planet may affect the distribution of small dust grains and pebbles, including CAIs and other inclusions not yet incorporated into parent bodies, throughout the surrounding disk. In particular, we place these results in the context of Jupiter in the solar nebula and how the movement of solids around the embedded Jovian embryo can be reconciled with the meteoritic record as well as implications for other disks.

Jupiter is typically thought to serve as the barrier of NC and CC reservoirs in the disk, with

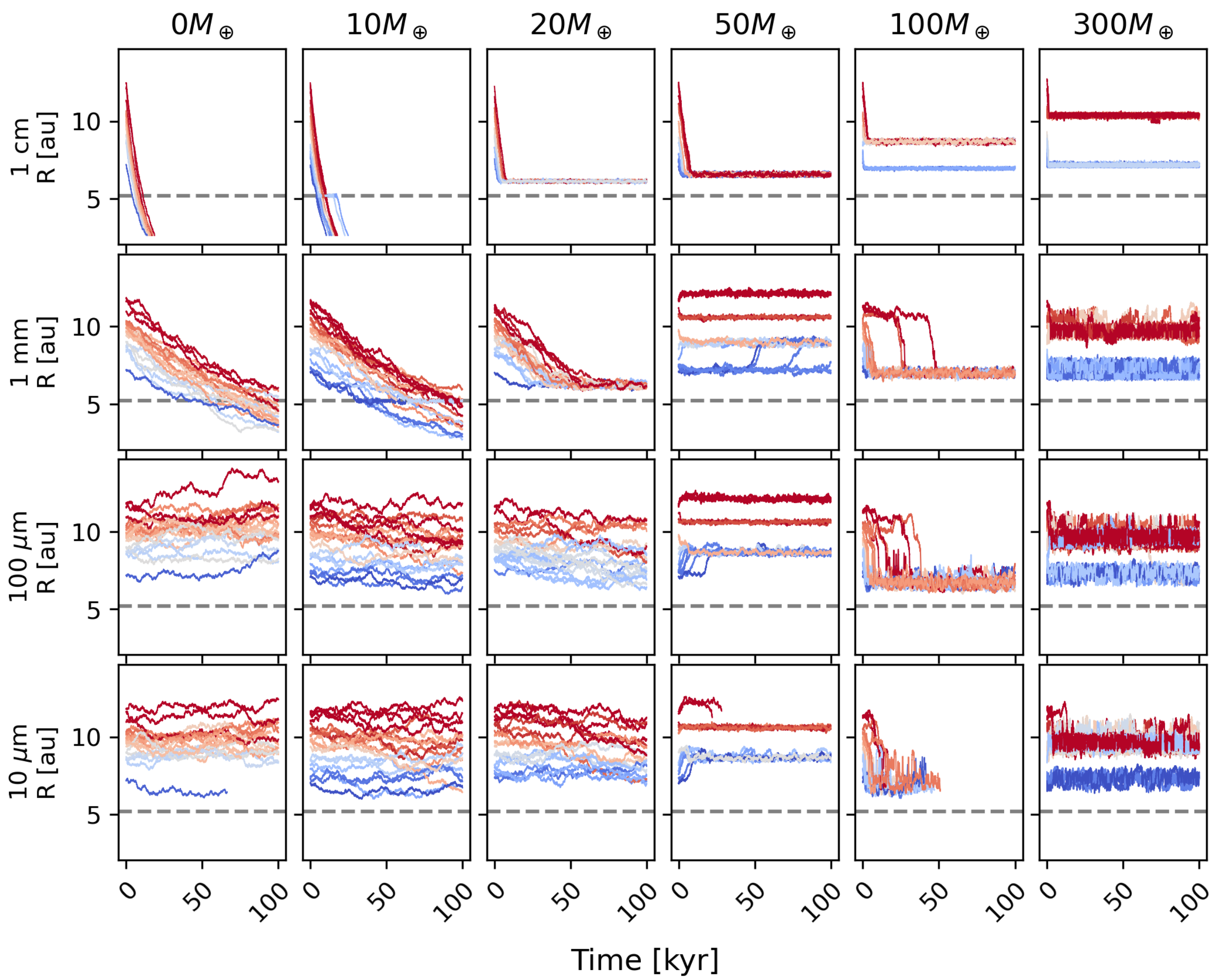

Figure 3.12: Some example trajectories of particles in a disk with an alpha of 10^{-4}, as in Figure 3.5. When compared with trajectories of solids in the $\alpha = 10^{-3}$ disks, these solids are much more concentrated radially, and tend to group in multiple radial locations in the outer disk. Additionally, filtering from the outer disk to inner disk is much rarer, as particles become decoupled from the gas advection due to lower gas densities. We note that in some cases, all particles reach the edges of the simulation before the 100 kyr integration time. In these cases of low viscosity, this is due to large scale coherent flows in the disk, eventually bringing all particles above 3 scale heights, the upper-limit of our simulation.

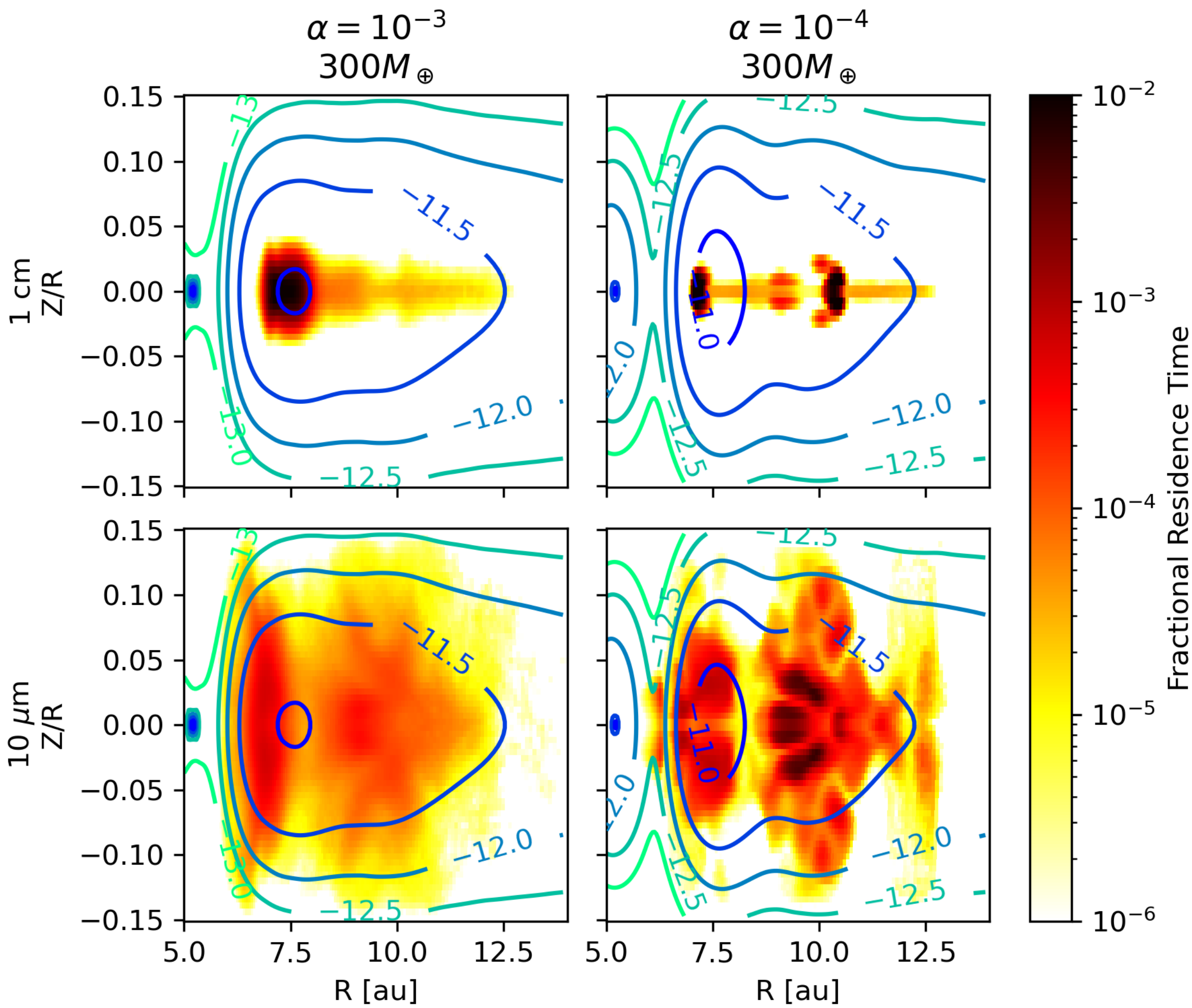

Figure 3.13: Azimuthally averaged residence times for the largest (top) and smallest (bottom) solids considered in high viscosity (left) and low viscosity (right) disks containing a 300 $M_\oplus$ planet. The contour lines show the surrounding gas density and are placed logarithmically, with contour labels indicating the $\log_{10}$ of the gas density. In the high viscosity case, the solids diffuse more vertically and tend to concentrate near the gap. In the high viscosity case, solids much more closely follow the gas advection, and are concentrated in much smaller areas. The small solids can spend significant amounts of time away from the midplane.

NC interior to the Jovian embryo and CC exterior (e.g. T. S. Kruijer et al., 2017, 2020). However, we have shown here that solids are able to mix between the inner and outer reservoirs, depending on the dust grain sizes and the mass of the growing embryo. Not only can small solids can drift inwards past the embedded embryo, consistent with previous results, but we have also shown that there can be outward mixing through the nebula throughout the growth of Jupiter. We explore how the results of the Monte Carlo technique presented here may relate to the mixing of isotopic reservoirs in the disk and the benefits of the Monte Carlo method presented here over alternative fluid-based simulations.

3.5.1 Growth to the Pebble Isolation Mass

We first consider the earliest stages of Jupiter's growth, when it was below the pebble isolation mass. In this early stage of growth, the embryo provides very little barrier to inward drift, with solids of all sizes crossing from the outer to the inner disk. As the embryo grows more massive, the transport of grains from the outer disk inward is slowed, with larger centimeter and millimeter sized grains completely trapped in the outer disk, while smaller sub-millimeter grains are able to cross the orbit of the planet even after the embryo has reached it's full Jupiter mass. The question arises, then, how Jupiter might act as a barrier between the inner NC and outer CC reservoirs throughout this time. This is only possible if 1) dust growth is limited such that drift-dominated pebbles do not grow and 2) gas viscosity is low, preventing turbulent mixing of small grains (See Figures 3.5, 3.7, 3.8, and 3.12). Given the ubiquity of millimeter-sized particles observed in other protoplanetary disks (e.g. S. M. Andrews et al., 2018), the presence of CAIs in meteorites in this size range, and the need for Jupiter's core to grow to tens of Earth masses, this scenario seems unlikely.

Considering the presence of drift-dominated pebbles in the outer disk, transport of outer disk material to the inner disk is problematic for a number of reasons. If pebble accretion rates are indeed 1-10% for large pebbles, as shown here and found in previous work (C. W. Ormel & B. Liu, 2018; B. Liu & C. W. Ormel, 2018; J. Drążkowska et al., 2021), this implies at least 100 $M_\oplus$ of solids must drift past the proto-Jovian core before reaching 10 $M_\oplus$. Not only would this present a significant source of pollution for the the inner isotopic reservoir, but this would also supply the inner disk with much more mass than expected given the mass of the inner terrestrial planets (R.

Brasser, 2020).

We note that there are other models for Jupiter's formation beyond pebble accretion. Formation via gravitational instability has been suggested, but points to a highly dynamic environment where large-scale mixing across the disk would occur (e.g. A. P. Boss, 2017, 2019), again making the preservation of separate isotopic reservoirs a challenge. Accretion of Jupiter's core via planetesimal collisions could also occur, but the question remains as to how to prevent the inward drift of solids during the ongoing growth of planetesimals, which we know formed over the course of millions of years (e.g. J. N. Connelly et al., 2012).

Given the challenge of preventing the inward drift of such a large amount of solids before Jupiter reached its isolation mass, we must consider that some other feature in the disk may have been responsible for creating a pressure bump in the disk early in its history. A number of mechanisms have been proposed to explain the ring structures observed in disks beyond planets. For example, snowlines may facilitate the growth of Jupiter while separating inner and outer reservoirs (R. Brasser, 2020; A. Izidoro et al., 2021; A. Morbidelli et al., 2021). As shown in T. Lichtenberg et al. (2021), snowlines may also act as the seed locations for the NC and CC planetesimals, without the need for a gap carved by Jupiter. The formation of such a bump early on in the disk lifetime may indeed aid in the formation of giant planets such as Jupiter (T. C. H. Lau et al., 2024). Thus, the isotopic dichotomy in the Solar Nebula may have been preserved by another process, and the formation of Jupiter was not the cause of the dichotomy, but an additional consequence of some other process or processes. More work considering the dynamical evolution of solids in such disks affected by these processes is needed.

3.5.2 Growth Beyond the Pebble Isolation Mass

We can also consider what the continued growth of Jupiter after it reached its isolation mass would mean for the preservation of the observed isotopic dichotomy. After the embryo reached the isolation mass, the inward drift of large pebbles was halted in the outer disk, leading to a pileup of millimeter and larger solids. If at this time most of the solid mass was contained in these drift-dominated pebbles, then leaking between reservoirs would be limited. Exchange of small dust, however, is possible in cases of high disk viscosity and turbulence. As shown in Figure 3.8, we find that upwards of 10% of small dust may have filtered from the outer disk to inner disk during this phase of Jupiter's growth for the case of $\alpha = 10^{-3}$. Additional transport of material from the inner reservoir outward may continue as shown in Figure 3.9 and discussed in Section 3.4.3.

Some amount of mixing between the inner and outer reservoirs at later stages of planet formation may help to explain various observations from the meteoritic record. Previous work has found evidence of NC-like material in CC meteorites (D. L. Schrader et al., 2020; D. L. Schrader & J. Davidson, 2022; E. Van Kooten et al., 2021) and interpreted this as a record of outward transport across Jupiter's orbit. Further, presence of only the smallest CAIs in NC meteorites compared to CC meteorites (E. T. Dunham et al., 2023) could be consistent with the leakage of only small particles from the outer disk to the inner disk. Such outcomes are dependent on the turbulence in the disk, and as such we cannot rule out alternative explanations, for example, CAI storage in early forming planetesimals (S. Ebert et al., 2024).

It is important to note that the later-crossing small dust is facilitated by the growing embryo, and, as a result, any dust that crossed the orbit of Jupiter at this later period did so by passing nearby the accreting planet. We call this the "funneling effect," as solids passing between inner and outer reservoirs are funneled past the embedded embryo. In some cases, we found particles moving within only a few hundred Jupiter radii of the embryo, just outside the planetary envelope (see Figure 3.6). While the details of the circumplanetary disk (or circumplanetary envelope) are not resolved here, the temperatures are expected to be elevated by $\sim$ 100 to 1000 K depending on the mass accretion rate of the embryo (see, e.g., J. Szulágyi et al., 2014, 2016; E. Lega et al., 2024; L. Krapp et al., 2024; F. Alarcón & E. A. Bergin, 2024). As such, later crossing dust may have lost volatiles as a result of thermal processing from the embedded embryo core (M. N. Barnett & F. J. Ciesla, 2022). If volatile ices and organics are the carriers of the supernova-derived isotopes (e.g. B. Liu et al., 2022), then this could provide a means of changing the isotopic compositions of the transported solids. The chemical implications of small grains passing by giant planets in the outer disk has recently been explored in H. J. Petrovic et al. (2024).

3.5.3 Global Effects and the Potential Trichotomy

In addition to the dichotomy between NC and CC meteorites, Ti and Fe isotopic measurements of CI chondrites and recently returned samples from the asteroid Ryugu have revealed a third potential isotopic reservoir in the solar nebula (S. Tachibana et al., 2022; T. Hopp et al., 2022; T. Yokoyama et al., 2023; E. Siciliano Rego et al., 2025). As such, an alternative model of meteorite formation may be a trichotomy model, requiring further separation of dust into at least three distinct regions in the disk.

In our models, we see that as Jupiter grew, the embedded planet can create multiple concentric rings in the disk beyond the pressure bump immediately outside of the planetary gap. In our simulations this secondary pileup occurs at about 10 au, though its exact location will depend on where Jupiter formed. This secondary pressure bump can either slow the inward drift, or halt it completely depending on the viscosity of the disk and size of the grains. Importantly, this bump and the one immediately outside the planet source solids from distinct regions in the disk, as in Figures 3.5 and 3.12. If there was a compositional gradient in the initial distribution of solids then these multiple dust reservoirs in the outer disk may remain compositionally distinct from one another, though mixing between these outer disk reservoirs may occur depending on disk viscosity and turbulence. These rings and the limited exchange of material between them may offer an explanation for the observed tertiary isotopic reservoir observed in CI meteorites and Ryugu samples.

Interestingly, we see that where grains do move between these reservoirs, they are transported quickly, moving multiple au through the disk on timescales much shorter than expected by drift. This can be seen in Figure 3.12 for 1 mm sized grains in disks containing 50 and 100 $M_\oplus$ embryos. This rapid transport may have important implications for understanding the chemistry of these solids as they change environments within the disk. The effects of UV radiation on ice-mantle chemistry of grains has been explored recently in, e.g. J. B. Bergner & F. Ciesla (2021) and L. Flores-Rivera et al. (2025) using similar techniques.

The dynamical separation that develops at more distant regions from the planet is most effective when the viscosity of the disk is low, as higher disk viscosities both broaden pressure bumps in the disk and enable greater diffusion of solids out of these pressure bumps. This is in contrast with the hypothesized late inward exchange of CAIs and outward transport of NC material described above, which relies on a higher disk viscosity. If this transport did occur, preservation of the trichotomy may require additional effects or substructures. The subsequent formation of Saturn and the ice giants may act to further separate the CI reservoir in the outer disk (T. Hopp et al., 2022; D. Nesvorný et al., 2024).

3.5.4 Future Work and Caveats

While we have mainly focused on the role of Jupiter in the solar nebula, these results are also applicable to PPDs more broadly. For example, the mass available for planet formation is dependent on the pebble flux through the disk (M. Lambrechts et al., 2019; B. Bitsch et al., 2019; G. D. Mulders et al., 2021). Thus the presence of an outer giant planet may limit the pebble flux through the disk, reducing the occurrence of super-Earth planets in the inner disk. However, observations of exoplanetary systems reveal that systems with Jupiter-like exoplanets often also contain inner super-Earth planets (W. Zhu & Y. Wu, 2018; M. L. Bryan et al., 2019; M. L. Bryan & E. J. Lee, 2024), although this correlation may not be conclusive (D. Barbato et al., 2018). The late, accretion-mediated filtering of small solids past an outer giant planet may allow enough small dust to pass that can then grow to pebbles, providing feedstock that would otherwise be shut off. We note that the exact size of solids that may pass the planet depends on the aerodynamic interactions between the gas and solids – as such the density of solids and density of the disk gas may change the size of solids capable of crossing the orbit of the planet proportional to these densities (see Equation 3.8)

Although this work assumes constant gas density and velocity structure, this may be expanded in the future to allow for time varying disk conditions. This will allow for the study of the effects of migration, disk dissipation, and multiple planets. For example, the early disk may have been a more turbulent decretion disk, as opposed to the assumed standard accretion disk. Such structure may have been important for the early outward transport of CAIs (J. N. Cuzzi et al., 2003; F. J. Ciesla, 2007; L. Yang & F. J. Ciesla, 2012; B. Liu et al., 2022).

Migration, in particular, may affect the fraction of material able to cross the orbit of the planet in either direction. In the regions of the disk explored here, planets tend to migrate inward faster than the unperturbed radial velocity of the gas (P. C. Duffell et al., 2014; C. Dürmann & W. Kley, 2015). If the planet migrates faster than the surrounding gas, then the relative velocity of the gas with respect to the migrating planet should be negative, that is, from the inside the planet's orbit to outside. This relative outward gas velocity would inhibit the inward transport of small particles across the planet gap, and increase the outward transport of solids (A. Morbidelli et al., 2023). This may increase the number of solids observed to migrate outwards as reported in Section 3.4.3, providing a mechanism for introducing NC like material to the outer CC reservoir. We note, however, that small particles tend to cross the orbit of the planet nearby the planet (Figure 3.6), where the gas flow is onto the planet and into the gap, as shown in Figure 3.4, rather than the gas velocity being only inward. As such, even with migration, we would still expect to see some amount of material crossing the orbit of the planet in both directions. That said, the effects of including a migrating planet with the particle tracking techniques presented here should be explored further in future work to address these questions on the filtering and accretion percentages. Migration would also affect the location in the disk where Jupiter is expected to form. For example, if Jupiter formed much further out in the disk than its current location (i.e. beyond the N_2 snowline; K. I. Öberg & R. Wordsworth, 2019; A. D. Bosman et al., 2019) then gas densities would be lower than explored here, affecting the meridional flows around the planet and the size of solids that remain well coupled to the gas.

Grain growth and fragmentation may have important implications for the transport of solids though the disk, as has been explored in, e.g.,J. Drążkowska et al. (2019); S. M. Stammler et al. (2023). For example, fragmentation near the planet may increase the density of small particles, providing a source of small dust which could migrate across the planet's orbit, as has recently been shown in L. E. J. Eriksson et al. (2024). Here, we do not explore the origin of the small dust. The consequences of the size evolution of solids should be explored more in future work, but it seems that fragmentation of large solids would increase the rate of solid mass transport across the planet's orbit.

As with all Monte Carlo methods, the results presented here are limited due to the finite number of particles integrated. In all cases, we explore a representative sample of a large number of particles originating in a small region of the disk. While we are not able to explore, for example, expected dust densities throughout the disk, this method excels in connecting regions of the disk, that is, understanding how particles from one region of the disk mix with material from other regions of the disk. Using the particle tracking technique presented here, we can begin to quantify the degree of radial mixing throughout the disk, as is discussed in Sections 3.4.2, 3.4.3, and 3.4.4. Although integrating a larger number of particles would enable us to better probe the low probability events (for example, accretion onto the planet or outward crossing particles), it would be computationally prohibitive to increase the number of particles explored. In its current implementation, the computation time scales linearly with the number of particles. As such, an order of magnitude increase in the number of particles integrated would require an order of magnitude increase in computation time.

Similar to limits on the number of particles, the computational time also scales linearly with the time of integration. As such, our simulations here are limited to less than 1 Myr, likely less than the age of the disk. However, it is important to note that throughout its lifetime, the disk and embedded planet are both constantly evolving. As such, the "snapshots" of constant disk and embryo mass are approximations, and such disk conditions are not expected to exist over million year timescales as considered. The results shown here, however, are useful limiting cases to demonstrate how mixing around the embedded planet changes over time.

Despite these drawbacks of Monte Carlo simulations, we believe there are benefits and novel insights of the techniques presented here compared with typical fluid-based studies. For one, we are able to study the dust evolution for a wide range of models out to 1 Myr. For our case with the planet at 5.2 au, this is equivalent to just under 100,000 orbits of the embryo, much longer than typical for hydrodynamic simulations. This is particularly true for the high resolution 3D hydrodynamic models we use for the gas structure here. Additionally, we are able to connect regions of the disk, quantifying mixing and accretion of solids onto the embedded embryo. While fluid approaches can identify regions of the disk where solids concentrate, similar to the residence time calculations in Section 3.4.4, we have shown here that solids in a given "clump" tend to be sourced from nearby in the disk (see, Figures 3.12 and 3.13 and discussion in Section 3.4.5) and, when they do move between reservoirs, do so quickly. These results are new findings of this technique and are not apparent from fluid approaches. Using these techniques we can begin to understand the chemical environments and residence times in those environments these are particles are expected to experience.

3.6 Conclusion

In this work, we have combined 3D hydrodynamic simulations of a disk containing an embedded planetary embryo with particle tracking techniques to model the transport and trajectories of solids. We place the histories of these small solids within the context of the meteoritic record of the Solar System, to constrain the timing and environment of Jupiter's formation.

We find that there was a significant evolution and change in the dynamical behavior of dust as Jupiter grew. Early on, before reaching the pebble isolation mass, solids were able to drift and diffuse from the outer disk to the inner disk freely and from all azimuthal angles. Given the large flux of solids expected in the disk at this time, preserving the NC-CC dichotomy across the orbit of the planet would be challenging. Instead, if some process or feature was already present that prevented or limited the drift of solids, then this would make preservation of the dichotomy possible and also could facilitate Jupiter's growth.

Once Jupiter grew to and beyond the pebble isolation mass, gas-drag-induced drift became inefficient, and the only solids that were capable of crossing the planet's orbit were small dust particles which were funneled from the outer disk to the inner disk, or from the inner to outer disk, immediately around the growing planet. Given the presence of NC materials in CC meteorites (D. L. Schrader et al., 2020; D. L. Schrader & J. Davidson, 2022; E. Van Kooten et al., 2021), and that the only objects in the NC meteorites that are genetically linked to those in the CC meteorites, CAIs, are smaller and less abundant than found in their outer disk counterparts (E. T. Dunham et al., 2023), it has been suggested that such crossing did occur. If true, then this implies that the disk was sufficiently turbulent or viscous around the orbit of the planet. Further, due to the funneling effect, any crossing solids passed nearby a luminous protoplanet, leading to some level of thermal processing of those solids.

Jupiter's growth would also impact the dynamics of dust particles at more distant regions of the solar nebula. At sufficient mass, it could create an additional pressure bump in the outer disk, which would collect solids and source them from a different region than the bump immediately exterior to the planet's orbit. This may further lead to compositional zoning of materials in the outer disk and may be recorded in the trichotomy suggested by analyses of CI meteorites and Ryugu samples.

Using the techniques presented here, we are able to identify individual grains that may cross the orbit of the embedded planet. Understanding the paths traveled by these solids will allow us to better understand the chemical processing expected to occur, as these solids move through drastically changing temperature and radiation environments throughout the disk. This technique also allows us to begin to quantify the extent of mixing between reservoirs in the disk and accretion onto the growing envelope and how these effects change over time as embedded planets grow. Thus, we can begin to study how planets sculpt their own environment during formation and affect the composition of the surrounding disk.

CHAPTER 4
DUST RECYCLING AND VOLATILE ENHANCEMENT

This chapter has been published as the following:

Van Clepper, E. R., Alarcón, F., Bergin, E., & Ciesla, F. J. 2025, "Dust Recycling and Icy Volatile Enhancement (DRIVE): A Novel Method of Volatile Enrichment in Cold Giant Planets", *The Astrophysical Journal Letters*, **994**, L44, doi: 10.3847/2041-8213ae1d81.

4.1 Chapter Abstract

Giant planet atmospheres are thought to reflect the gas phase composition of the disk when and where they formed. However, these atmospheres may also be polluted via solid accretion or ice sublimation in the disk. Here, we propose a novel mechanism for enriching the atmospheres of these giant planets with volatiles via pebble drift, fragmentation, and ice sublimation. We use a combination of 3D hydrodynamic simulations, radiative transfer, and particle tracking to follow the trajectories and resulting temperatures of solids in a disk containing an embedded planet forming outside the CO snowline. We show that small dust can become entrained in the meridional flows created by the giant planet and advected above the disk midplane where temperatures are well above the sublimation temperature of CO. This transport of small grains occurs over 10 kyr timescales, with individual micron-sized grains cycling between the midplane and surface of the disk multiple times throughout the planetary accretion stage. We find that this stirring of dust results in sublimation of CO gas above the snow surface in the dust trap created exterior to the giant planet, leading to super-solar CO abundances in the pressure bump. This mechanism of Dust Recycling and Icy Volatile Enhancement in cold giant planets, which we call the DRIVE effect, may explain enhanced metallicities of both wide separation exoplanets as well as Jupiter in our own Solar System.

4.2 Introduction

A major goal of studying protoplanetary disk (PPD) evolution is to connect observed exoplanets with their formation regions within the disk. Observations of young giant planets and PPDs, however, have revealed an unexplained mismatch between disk and planetary compositions. Cold giant planets have been observed to have an enriched metallicity compared to their host star, both in our solar system and around other stars (S. K. Atreya et al., 2020; C. Li et al., 2020; C.-C. Hsu et al., 2024; E. Nasedkin et al., 2024; E. A. Bergin et al., 2024; W. O. Balmer et al., 2025; J. D. Lothringer et al., 2025). The gas phase metallicity in the outer disk, however, should be low, with the majority of major C- and O-bearing molecules frozen out onto grains (K. I. Öberg et al., 2011; E. A. Bergin et al., 2024). While the gas in the cold outer regions of PPDs is carbon rich and low metallicity, the atmospheres of giant planets that are inferred to form in these regions of the disk have lower C/O and higher metallicity than their host star. Understanding the composition of the disk gas during the formation of these giant planets, and possible enrichment in volatile elements, is necessary for connecting observed compositions and metallicities of giant planets to the disk conditions in which they form.

One of the current leading theories for giant planet formation is pebble accretion, wherein planetary cores grow by accreting drifting pebbles through the disk (M. Lambrechts & A. Johansen, 2014). In this model, planetary core composition is set by the composition of these solids, both the refractory grain as well as any volatiles that may be present as an ice mantle. Once the core grows large enough, it opens a gap in the disk, halting the inward drift of solids and shutting off pebble accretion (M. Lambrechts et al., 2014). Though the pebble isolation mass depends on the gas scale height and turbulence, typical masses are on the order of a few 10s of Earth Masses (B. Bitsch et al., 2018). At this stage, the core accretes gas from the disk, undergoing a runaway growth phase until the gas disk dissipates (J. B. Pollack et al., 1996). During this runaway growth phase, the atmosphere of the planet should accrete primarily gas, with the planet becoming more metal poor as it grows in mass, reflecting the metallicity of the PPD gas (D. P. Thorngren et al., 2016). So while the core of the planet may initially be metal rich, once the planet reaches the pebble isolation mass the atmosphere should largely reflect the relatively metal poor composition of the gas where the planet formed.

One way to alter the composition of a giant planet atmosphere is if the planet grows inside of a snowline in the disk. As pebbles drift from the outer disk, they will pass snowlines, enriching the region interior in volatiles (J. N. Cuzzi & K. J. Zahnle, 2004; F. Ciesla & J. Cuzzi, 2006; K. I. Öberg & E. A. Bergin, 2016; R. A. Booth et al., 2017; C. Danti et al., 2023). If a planet grows just interior to one of these snowlines, then its atmosphere should become enriched in those volatiles (A. D. Schneider & B. Bitsch, 2021a,b). Additionally, if the ice present on these grains carries with it trapped noble gasses, this sublimation may explain the enrichment of both volatiles and noble gasses in Jupiter's atmosphere (N. Monga & S. Desch, 2014; O. Mousis et al., 2019; S. K. Atreya et al., 2020). This model is particularly attractive as snowlines can also create local pebble pile-ups, which may help to initiate core formation (J. Drążkowska & Y. Alibert, 2017; G. Andama et al., 2022; T. C. H. Lau et al., 2022). This, however, requires the planetary core to accrete gas from the region just interior to the snowline, and cannot explain any enrichment of a given species exterior to its respective snowline.

Recent models have shown that the growing planetary embryo, surrounding gas, and smaller solids all interact with one another, complicating the otherwise simple picture of giant planet formation. One such complication is the meridional flow patterns of gas accretion onto the planet in 3D (W. Kley et al., 2001; A. Morbidelli et al., 2014; J. Szulágyi et al., 2014; J. Fung & E. Chiang, 2016; R. Teague et al., 2019; E. Lega et al., 2024). Hydrodynamic simulations of gap opening planets in 3D show that gas moves outward, away from the planet along the spiral arms at the midplane. Gas flows are away from the midplane at the gap edges and fall onto the poles of the planet from 1-3 scale heights above the midplane. Such 3D stirring can entrain small dust, increasing the dust scale height near the planet (J. Bi et al., 2021) and even lead to the accretion of small dust onto the planet (J. Szulágyi et al., 2022; N. Maeda et al., 2024; H. J. Petrovic et al., 2024; E. R. Van Clepper et al., 2025b).

In this work, we examine the chemical consequences of the vertical stirring immediately outside a growing planet, and the delivery of volatiles to the planetary atmosphere. First, we describe our methodological approach, including disk hydrodynamic simulations, radiative transfer modeling, Monte-Carlo particle integrations, and dust growth and fragmentation simulations. Using the results of these combined modeling techniques, we show that the Dust Recycling and Icy Volatile Enhancement (DRIVE) effect can lead to an enhancement of the gas phase abundance of volatiles, even exterior to the their respective snowlines. Here, we use the enrichment of CO exterior to the CO snowline as an example, though the DRIVE effect can work in general, and is expected to function in a similar manner for other volatile ice species. We discuss these results in the context

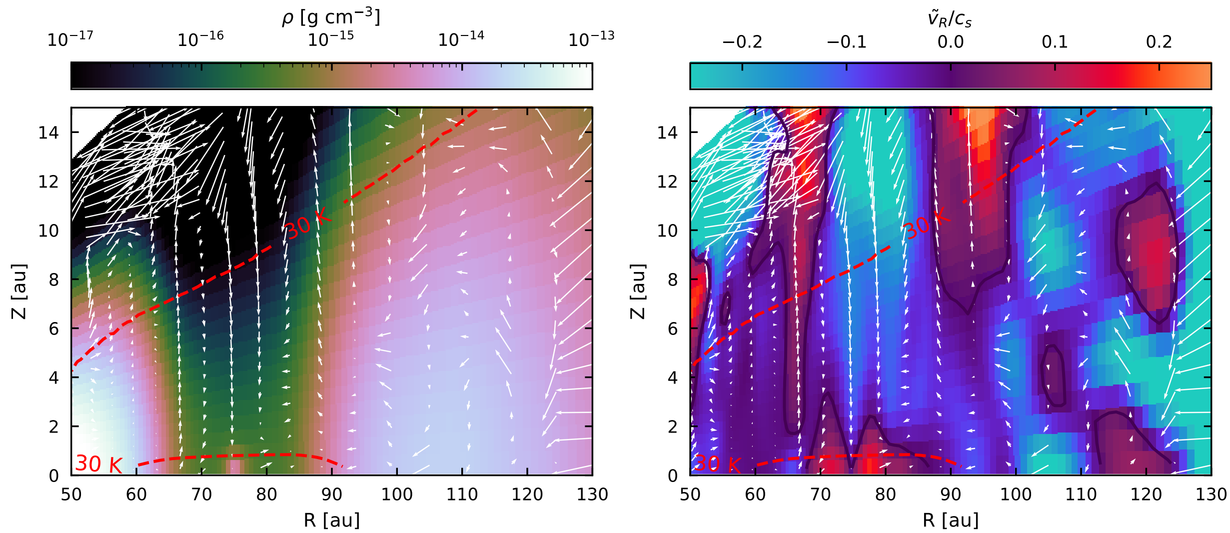

Figure 4.1: Azimuthally averaged gas density (left) and gas radial velocity relative to the planet (right) for our FARGO3D disk model containing a Jupiter mass planet at 75 au. The CO sublimation surface at 30 K recovered from our RADMC-3D model is indicated in both panels by the red dashed line. The region near the embedded planet is heated from a combination of accretion heating onto the planet, disk viscous heating, and radiative heating from the star, resulting in higher temperatures at the midplane in the gap. Gas advection relative to the local sound speed is also indicated by white arrows. Gas advection is primarily outward along the midplane near the planet, with significant vertical flows away from the midplane at the gap edge and in the pressure bump at 100 au.

of Jupiter and other directly imaged exoplanets and compare with other mechanisms of volatile enhancement in giant planet atmospheres.

4.3 Methodology

To explore the consequences of dust stirring near an embedded giant planet, we model the gas disk using single-fluid FARGO3D hydrodynamic simulations (F. Masset, 2000; P. Benítez-Llambay & F. S. Masset, 2016) with 256 radial cells ranging from 30 au to 337.5 au, 512 cells in azimuth from 0 to 2π, and 32 cells in colatitude spanning from 1.32 rad to the disk midplane. We simulate a 0.05 $M_\odot$ disk around a 1 $M_\odot$ star. We include a 318 $M_\oplus$ giant planet at a fixed separation of 75 au using a mass taper over the first 100 orbits. The disk aspect ratio at the planet separation was set to 0.05. The disk is simulated for 1000 orbits, and the resulting structure is used to determine the dust temperature in post-processing, following F. Alarcón & E. A. Bergin (2024). The resulting gas density and velocity structure are shown in Figure 4.1, with the velocity shown relative to the planet, $\tilde{v}$, with $\tilde{v}_r < 0$ indicating gas flow towards the planet. Near the midplane, gas is primarily flowing away from the planet along the spiral arms. Gas accretion tends to be onto the poles of the planet, as is expected from meridional flow patterns (W. Kley et al., 2001; A. Morbidelli et al., 2014; J. Szulágyi et al., 2014). Within the pressure bump near 100 au, gas advection tends to be vertically away from the midplane.

The temperature within the disk is determined using RADMC-3D (C. P. Dullemond et al., 2012) including radiation from the central star, emission from the embedded planet, and viscous heating (see F. Alarcón & E. A. Bergin, 2024). For the temperature structure, we assume a constant dust-to-gas mass ratio of 0.01, with the solid mass entirely in small dust. The outer disk is characterized by passive heating, with the upper layers of the disk being hotter than the regions close to the midplane (E. I. Chiang & P. Goldreich, 1997). In the gap, a combination of accretion heating from the planet, viscous heating at the midplane, and asymmetric dust scattering results in increased temperatures near the midplane, as shown via the isothermal contour in Figure 4.1.

As an example of a volatile species, we track the sublimation of CO from the grains at this location in the disk. CO is highly volatile in protoplanetary disks; the temperature at which it begins to appreciably come off the grains depends on the CO binding energy and surface area of grains available. The binding energy of CO is uncertain and depends on the ice mixture on the mantle of the grain, with literature values ranging from 855 K (D. McElroy et al., 2013) up to 1500 K (E. C. Fayolle et al., 2016), suggesting freeze-out temperatures of ~20 - 30 K. Throughout this work, we use a conservative assumption for the CO sublimation temperature of 30 K, corresponding to a midplane snowline location of 45 au, interior to the planet location of 75 au modeled here. The location of the CO snowline is shown by the red dashed line in Figure 4.1. While this temperature is an approximation, the results presented here do not depend the exact temperature, and we discuss differing heights of the CO sublimation surface later. Although, heating from the embedded planet increases the midplane temperature above the CO sublimation temperature near the edge of the gap, the main region of the pressure bump that is above 30 K is above $Z/R \approx 0.1$, slightly above 1 scale height at this location of the disk.

Small solids in the disk, which serve as the feedstock of planetesimals and planets, can be grouped via their aerodynamic properties and interactions with the gas. These aerodynamic properties are defined via the Stokes number, St, which is the dimensionless ratio of the stopping time to the orbital period of the solid. Throughout this work, we refer to two main populations of solids, the small dust and larger pebbles (as in, e.g. T. Birnstiel et al., 2012). Small dust ($\mathrm{St} < 10^{-3}$) is defined as those solids which are primarily coupled with the gas, and whose dynamics are strongly affected by gas advection and turbulence. The dynamics of larger pebbles ($10^{-3} < \mathrm{St} \lesssim 1$) are mainly driven via gas drag-induced radial drift (S. J. Weidenschilling, 1977). Pebbles also experience significant settling, with typical scale heights much less than that of the gas, in contrast with the smaller dust which has a comparable scale height to the gas (A. N. Youdin & Y. Lithwick, 2007).

Once the physical conditions within the disk are known, we track the location and temperature of pebble and dust tracer particles of constant size using the 3D Monte-Carlo particle tracking technique described in E. R. Van Clepper et al. (2025b). Particles are started at the midplane exterior to the gap opened by the giant planet, here at about 100 au. We examine particle sizes ranging from sub-micron, $\mathrm{St} < 10^{-5}$, up to 1 cm in size, $\mathrm{St} \approx 1$. Because the solids are integrated using a constant particle size, their Stokes numbers vary throughout the integration, with the Stokes number inversely proportional to the gas density. As a result, particles' Stokes numbers decrease in the pressure bump, where gas densities are at a local maximum, and increase in the gap and away from the midplane, where gas densities are lower. Where Stokes numbers are given here, it is the Stokes number for solids at the midplane at 100 au as a means to compare between the 3D constant size integration and 1D DustPy simulations, described further below. Particles of all sizes are integrated forward in time including random diffusion for 1 Myr, with their locations recorded every 10 years (~ 0.01 orbital period). At each time, the temperature of the particles are interpolated from the RADMC-3D outputs. While the RADMC-3D simulations only consider the small, well-coupled dust to determine the dust temperature, we assume that all dust and gas are in thermal equilibrium; that is, the temperature of all sizes of dust and the gas is the same at a given location of the disk.

While particles in our simulations remain at fixed sizes, we also use DustPy simulations (S. M. Stammler & T. Birnstiel, 2022) to model the dust size evolution for the disk. We match the DustPy surface density to the FARGO3D simulation including a Jupiter mass planet at 75 au. The disk is initialized with a MRN-like dust size distribution (J. S. Mathis et al., 1977) in the outer disk

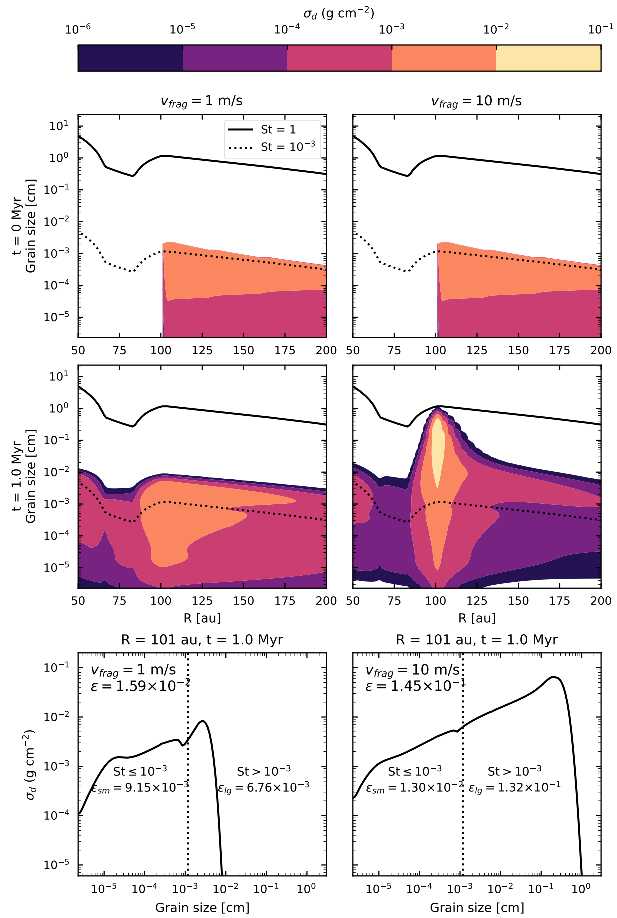

Figure 4.2: Dust distribution as a function of size and radius from DustPy simulations showing the initial conditions of the dust size distribution (top row) and after 1 Myr of evolution (center row) for a disk containing a Jupiter mass planet located at 75 au. We examine disks with particle fragmentation velocities of 1 m s^{-1} (left column) and 10 m s^{-1} (right column). The grain size distribution in the pressure bump at 101 au is shown in the bottom row. Regardless of dust fragmentation velocity, we see an enhancement of small dust less than St = 10^{-3} (dotted line) in the pressure bump. The total dust-to-gas mass ratio, ε, is labeled in each plot, where the initial dust-to-gas is $\varepsilon = 0.01$ in the outer disk. The dust-to-gas mass ratios for grain with St $\leq 10^{-3}$, ε_{sm}, and St $> 10^{-3}$, ε_{lg} are also shown. For the case with larger fragmentation velocity, while the total dust mass is higher and grains reach much larger sizes, the total mass of dust with St $\leq 10^{-3}$ is about 0.01 in both cases.

with a dust-to-gas mass ratio of 0.01. As the fragmentation velocity of dust is uncertain, we do two simulations, one with a fragmentation velocity of 1 m s^{-1} and one with 10 m s^{-1}. Both simulations assume a constant α viscosity parameter of $\alpha = 10^{-3}$ as in our FARGO3D runs. The initial conditions and dust size distribution after 1 Myr of evolution for both simulations are shown in Figure 4.2. The location of the pressure bump in the DustPy simulations is centered at 101 au, agreeing with the full 3D hydrodynamic simulations.

4.4 The DRIVE mechanism

Combining these techniques, we examine the stirring of small dust in the pressure bump created by a giant planet. We find that a natural consequence of dust growth is the concentration of solids in the dust trap and stirring of small dust to higher and warmer regions of the disk, enriching the gas accreted onto the planet in volatiles. Figure 4.3 shows a cartoon illustration of this process highlighting the essential ingredients: pebble drift, fragmentation, meridional circulation, and volatile sublimation. We refer to this process as "Dust Recycling and Icy Volatile Enhancement" (DRIVE), whereby small dust grains undergo a cycle of growth and fragmentation, transporting volatile ices above the snow surface and sublimating them into the gas phase. The gas, now enriched in volatiles sublimated from the grains, can then be accreted onto the planet and incorporated into the giant planet atmosphere. Thus, we do not require giant planets to grow interior of the midplane snowline to inherit volatile gas into their atmosphere. This provides a novel way to enrich the atmospheres of cold giant planet after they have reached the pebble isolation mass.

4.4.1 Solid concentration and fragmentation

Once they reach the pebble isolation mass, giant planets create pressure maxima external to their orbit (R. R. Rafikov, 2002), where radial drift is halted and solids can concentrate (S. J. Weidenschilling, 1977; M. Lambrechts et al., 2014; C. P. Dullemond et al., 2018). In these regions, grains grow to a certain maximum size before relative velocities exceed fragmentation velocities, breaking apart larger pebbles into small dust grains (T. Birnstiel et al., 2011, 2012). Indeed, numerical simulations have shown that fragmentation is a common outcome in the pressure bump exterior to a giant planet (J. Drążkowska et al., 2019; S. M. Stammler et al., 2023; L. E. J. Eriksson et al., 2024).

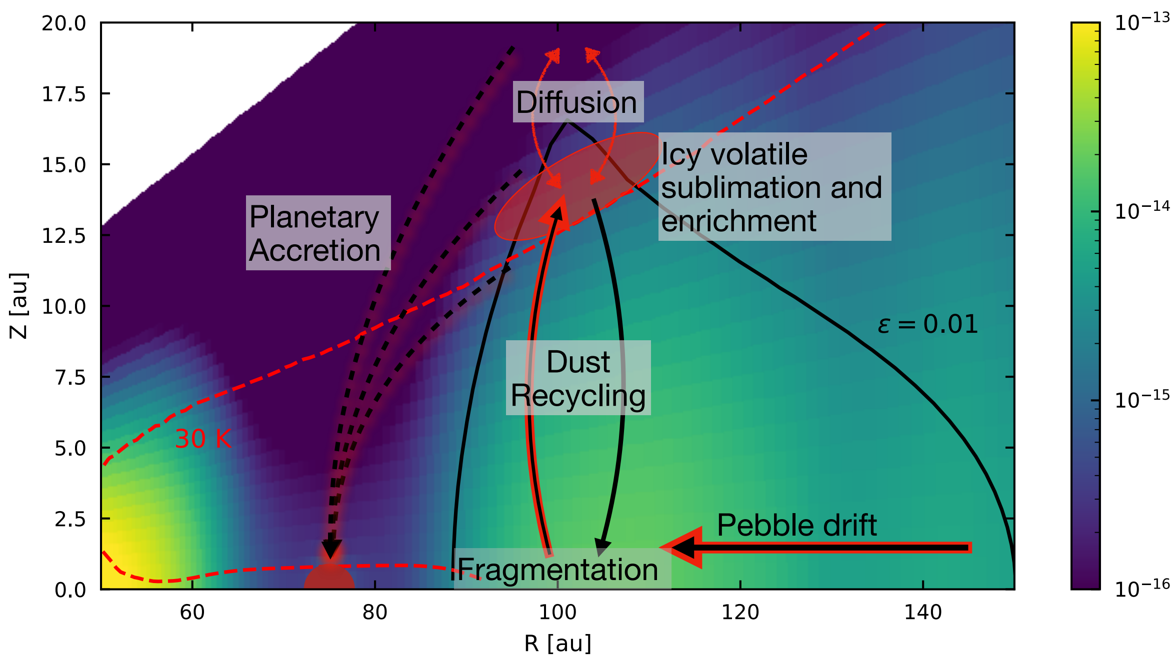

Figure 4.3: Cartoon schematic of the DRIVE effect enriching the atmosphere of a giant planet with volatiles. Larger pebbles trap volatiles from the outer disk and transport them to the pressure bump created by the giant planet via radial drift. Here, fragmentation creates fine dust, which can be lofted away from the midplane, leading to sublimation of ice mantles on the dust and enriching the gas above the snow surface with volatiles. This volatile rich gas can then be accreted onto the planet, resulting in a volatile enriched atmosphere. The dust, due to the lower gas density at the surface of the disk, decouples from the gas and can settle back to the midplane as a bare grain, fractionating the volatile elements from the more refractory solids. Here, the color shows the azimuthally averaged gas density from our FARGO3D simulations. The solid black contour outlines the region of the disk where total dust-to-gas mass ratio is equal to 0.01 in our DustPy simulations, with higher dust-densities below this contour. The transport of icy pebbles is represented by the black and red solid arrows, while black arrows represent bare grains and red arrows represent CO gas. Meridional flows onto the planet including entrained CO gas are illustrated by the red and black dashed arrows. The approximate location of the CO snowline at 30 K is also included.

Our DustPy simulations show that regardless of fragmentation velocities assumed, the pressure bump exterior to the planet becomes enriched in both large pebbles and small dust. Because these dust grains in the bump are supplied by inward drift of ice-rich pebbles, the increase in dust mass also corresponds with an increase in total CO in the bump. Figure 4.2 shows the grain size distribution in the pressure bump, where both the dust-to-gas mass ratio, ε, and maximum grain size reach peak values. We also show the dust-to-gas mass ratios for small and large grains, ε_{sm} and ε_{lg} respectively, where we define small grains as dust (St$\leq 10^{-3}$) and large grains as pebbles (St$> 10^{-3}$). In both the model with low fragmentation velocity and high fragmentation velocity, the total dust-to-gas mass ratio is increased above the initial value of 10^{-2}, with $\varepsilon = 1.59 \times 10^{-2}$ and 1.45×10^{-1} respectively after 1 Myr. Despite differences in the total dust-to-gas ratios, the value of ε_{sm} is comparable in both cases, $\varepsilon_{sm} = 0.915 \times 10^{-2}$ and 1.3×10^{-2} for $v_{frag} = 1$ m s^{-1} and 10 m s^{-1} respectively. Regardless of fragmentation velocity, we see an enhancement not only in the total dust-to-gas mass ratio, but also an enhancement of the small, well-coupled dust with St $\leq 10^{-3}$, approximately equal to the initial value of 0.01 in the pressure bump exterior to the planet. This enhancement in small dust is key to the delivery of CO ice to the gas, as the small dust is more mobile in the pressure bump and can be lofted to regions in the disk above the CO sublimation temperature, sublimating CO from the ice phase into the gas.

4.4.2 Dust recycling and ice sublimation

Next, we examine the thermal histories of solids of different sizes immediately exterior to the planet. The larger pebbles, here ranging from 100 µm to 1 cm, tend to stay near the cold midplane, while grains smaller than 10 µm can be lofted to higher elevations and reach higher temperatures. Figure 4.4 shows the maximum temperature reached by 1000 particles of different sizes over time. Dust with sizes $\leq$ 10 µm (St $\leq 10^{-3}$) experience temperatures much higher than the midplane temperature of 21 K. After 0.1 Myr, 75% of micron-sized dust has reached temperatures well above the CO sublimation temperature of 30 K with 100% of the small dust reaching temperatures above 30 K by 1 Myr. This trend is similar for 10 µm, while the larger 100 µm show only about 10% of grains reaching above 30 K, with no millimeter or larger grains reaching the CO sublimation temperature. These larger grains tend to experience some heating from the luminous planetary

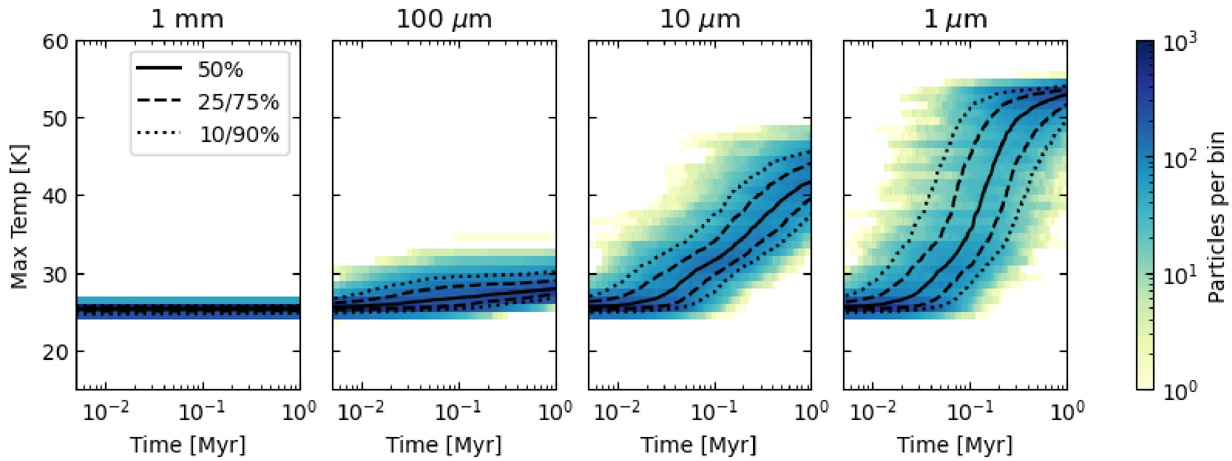

Figure 4.4: The maximum temperature reached by particles of different sizes, ranging from 1 mm to 1 μm (right column) for particles starting at the midplane at 100 au. The colormap shows the number of particles out of 1000 total that have reached a given temperature as a function of time. Also indicated in each plot by a solid line is the 50^{th} percentile for maximum temperature reached as a function of time. The dashed lines show the 25^{th} and 75^{th} percentiles, and dotted line show 10^{th} and 90^{th} percentiles. While large particles are not heated much above the midplane temperature, solids below 10 μm in size (St $\lesssim 10^{-3}$ at the midplane experience heating. All of these dust particles experience temperatures above 30 K by 1 Myr.

embryo, but here it is insufficient for CO sublimation, and we focus on the heating of small grains at the surface of the disk.

The locations and temperatures over time for one hundred 1 μm sized examples particles are shown in Figure 4.5. Although these small dust grains tend to experience the highest degree of heating, they spend the majority of the time near the midplane and low temperatures. When these solids are heated, it is typically during brief excursions to upper layers of the disk, before returning to the cold midplane, as has been found in studies of disks not containing a planet (e.g. F. J. Ciesla & S. A. Sandford, 2012; J. B. Bergner & F. Ciesla, 2021; L. Flores-Rivera et al., 2025).

This migration of small grains to the disk surface is enhanced via the meridional flows created by the planet. 3D hydrodynamic simulations have shown that planet-induced pressure bumps can significantly increase the scale height of small dust (J. Bi et al., 2021; J. Szulágyi et al., 2022). In Figure 4.5, we also show the trajectory of the particle that experiences the highest degree of heating near the time when it reaches this temperature. The planet creates meridional flow patterns that can entrain small particles, lifting them near the surface of the disk. Here, where the dust grains

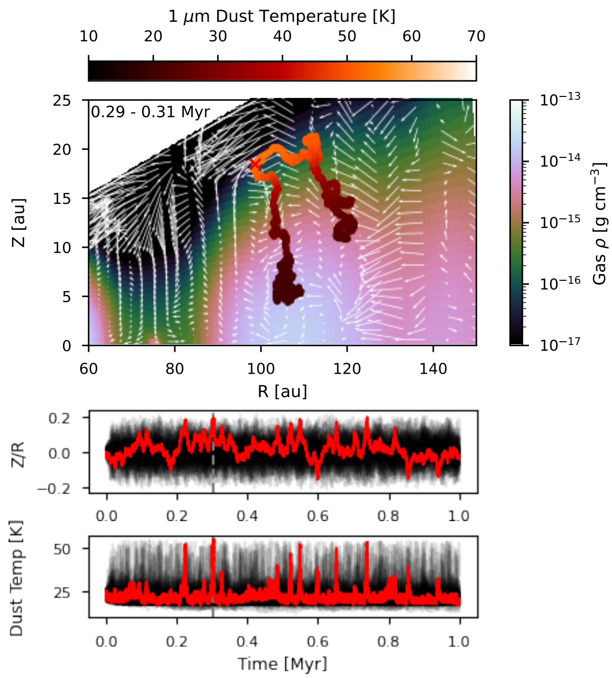

Figure 4.5: (Top) Particle trajectory of the tracer particle reaching the maximum temperature, with the hottest point labeled with a red dot. The background color and arrows show the azimuthally averaged gas density and advection. This particle is lofted to high altitude following the meridional gas circulation in the disk, reaching temperatures up to 55 K. The particle's temperature along its trajectory is shown by the color of line. The particle temperature is shown over 20 kyr to demonstrate the particle's trajectory before and after reaching the hottest point at 0.3 Myr. This particle's height above the midplane (middle) and temperature (bottom) are also shown as a function of time over the full 1 Myr integrated by the red lines. Examples of other particles are also shown in black, indicating the highlighted particle's trajectory and temperature are typical of other similarly sized particles.

are heated, they sublimate CO ice to the gas phase, increasing the CO gas abundance above the snow surface. In Figure 4.5, the highlighted particle's position and temperature is shown over only 20 kyr, yet the dust particle is transported vertically over 2 gas scale heights. While the timescale for vertical transport via turbulence in the disk is $\tau_{turb} = (\alpha\Omega)^{-1} \approx 200$ kyr for $\alpha = 10^{-3}$, dust particles simulated here tend to be transported on much shorter timescales, indicating gas advection as the dominant transport mechanism.

While these grains initially follow the gas advection away from the midplane, they do not tend to be accreted by the planet. This is because as the small grains are lofted, the gas density decreases, resulting in an increase to the particle's Stokes number. Thus, while experiencing heating at the surface of the disk, the grains decouple from the gas flow and settle back to the midplane, where – now depleted in CO ice – they may coagulate into larger pebbles (S. Krijt & F. J. Ciesla, 2016; W. Misener et al., 2019). Any gas phase CO that is not accreted onto the planet may diffuse back below the snow surface and freeze out again as ice. Even if some amount of CO vapor returns to the grain, that grain remains in the pressure bump, where fragmentation will resupply the fine dust, which can again transport that CO ice back to the disk surface, repeating the cycle of grain lofting and volatile sublimation. As a result, a single micron sized grain may transport CO ice to the surface of the disk multiple times over the disk lifetime.

4.4.3 Giant planet atmosphere enrichment

We have shown that embedded giant planets are expected to both create dusty pile-ups exterior to their orbit and that dust grains in this pile-up should experience heating when they advect to the upper regions of the disk. These small grains are resupplied via the fragmentation of inward drifting, volatile-rich pebbles from the outer disk. As a result, volatiles are carried to the surface regions of the disk, where they can sublimate and be accreted onto the planet, even in the case where the planet is located outside of the midplane snowline.

To determine the magnitude of enhancement we expect above the snow-surface, we assume a steady-state dust distribution based on our DustPy simulations. We assume that this disk structure has evolved from an initially homogeneous disk, with constant dust-to-gas and CO abundance given by ε_0 and $X_{\mathrm{CO},0}$ respectively, where the dust-to-gas is given by $\varepsilon_0 = \rho_{dust}/\rho_{gas} = 0.01$. Outside of the CO snowline, CO is entirely frozen onto grain surfaces such that the CO-to-grain mass ratio remains constant throughout the disk evolution. Additionally, we assume that grains heated above 30 K are able to fully sublimate CO from the ice-phase to the gas phase, such that the CO gas abundance, $X_{\rm CO}$, is proportional to the mass of grains heated above 30 K. Finally, we assume that in this steady-state approximation CO is able to diffuse vertically, such that $X_{\rm CO}$ is constant everywhere above the snow surface.

This process is outlined in Figure 4.6, showing a schematic of the dust-to-gas and CO abundance in a column of the disk over time. Initially, the dust-to-gas mass ratio is constant throughout the column, and CO is only present as gas above $Z_{\rm sub}$, where $Z_{\rm sub}$ is the height above the midplane where ice sublimation occurs. For CO sublimation at $T = 30$ K, this is located at $Z/R \approx 0.1$ at 100 au, but $Z_{\rm sub}$ will depend on the radial location in the disk and sublimation temperature for the specific volatile species of interest. If the dust in the column is puffed up, as we expect from giant planet induced stirring, then these grains will carry CO ice above the sublimation surface, increasing the abundance of CO there.

Under these assumptions, the total abundance of CO gas above the snow surface is given by

$$X_{\rm CO} = \frac{\beta(Z_{\rm sub})}{\varepsilon_0} X_{\rm CO,0} = f_{\rm CO} X_{\rm CO,0}, \tag{4.1}$$

where $\beta(Z_{\rm sub})$ is the integrated dust-to-gas ratio above $Z_{\rm sub}$. The enhancement in CO above the initial abundance is given by $f_{\rm CO} = \beta(Z_{\rm sub})/\epsilon_0$, where $\beta(Z_{\rm sub})$ is given by the equation

$$\beta(Z_{sub}) = \frac{\int_{Z_{\rm sub}}^{\infty} \int_{a_0}^{a_{\rm max}} \eta(a, z)\ {\rm d}a\ {\rm d}z}{\int_{Z_{\rm sub}}^{\infty} \rho(z)\ {\rm d}z}. \tag{4.2}$$

Here, $\rho(z)$ is the gas density and $\eta(a, z)$ is defined such that $\int_{a_0}^{a_{max}} \eta(a, z)\ {\rm d}a = \rho_{\rm dust}(z)$ gives the total volume density of dust at height z, with a_0 and $a_{\rm max}$ being the smallest and largest grains present. By definition, $\beta(0)$ (where $Z_{\rm sub}/R = 0$ corresponds to a location interior to the midplane volatile snowline) is equivalent to the column integrated dust-to-gas mass ratio. This corresponds to the total ϵ from our DustPy simulations (See Section 4.4.1 and Figure 4.2). Inside of the midplane snowline, all of the volatile ice is expected to be sublimated. At this location where $Z_{\rm sub}/R = 0$, $f_{\rm CO}$

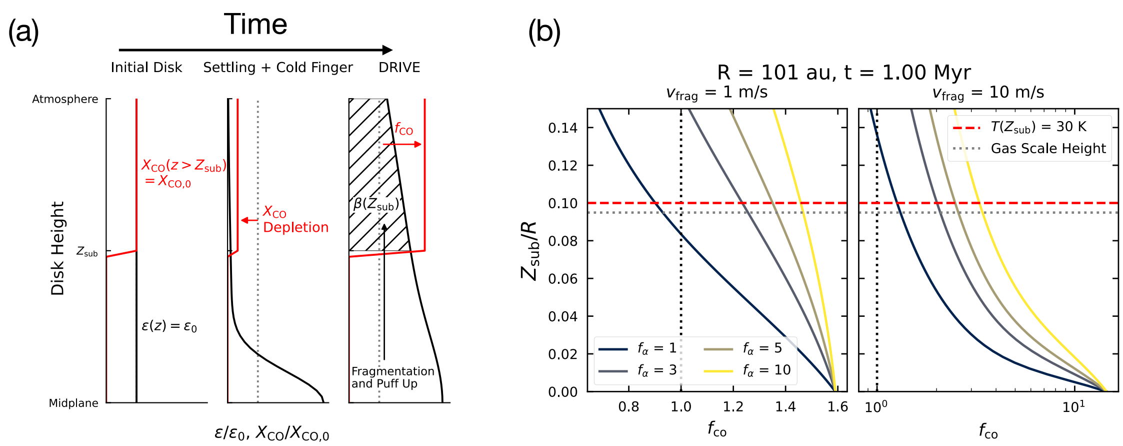

Figure 4.6: *(a):* Schematic diagram illustrating the vertical stirring of dust and expected CO enrichment. Initially, the vertical column has a uniform dust-to-gas mass ratio, ε, shown in black, and gas-phase CO abundance $X_{\rm CO} = X_{\rm CO,0}$, shown in red, above the sublimation height, $Z_{\rm sub}$ (top). Typically, dust growth and settling concentrated dust mass near the midplane, with CO gas depleted as a result of the cold finger effect (middle). In the DRIVE Mechanism, dust is puffed vertically from planetary stirring carrying CO ice above the sublimation height. CO ice is then sublimated into the gas phase, with the abundance of CO proportional to the integrated dust-to-gas mass ratio above $Z_{\rm sub}$, indicated by the hatched region. *(b):* Expected CO abundance relative to the initial abundance, $f_{\rm CO}$, as a function of $Z_{\rm sub}$ and f_α. $f_{\rm CO}$ is calculated from the DustPy simulation after 1 Myr of evolution in the pressure bump for fragmentation velocities of 1 m s^{-1} (left) and 10 m s^{-1} (right). The CO sublimation surface where dust temperatures reach 30 K is shown by the red dashed line, while the gas scale height is shown by the gray dotted line. The dust scale-height is increased using a diffusivity of $f_\alpha \alpha$, accounting for vertical stirring as a result of meridional flows. We find that for $Z_{\rm sub}/R < 0.1$, dust densities (and thus CO abundances) are near or above expected solar metallicities in all cases.

is precisely the enhancement in dust-to-gas relative to the initial ϵ_0 integrated vertically. Exterior to the midplane snowline ($Z_{\rm sub}/R > 0$), some amount of volatiles remain in the ice phase near the midplane, with the abundance of sublimated volatiles proportional to the dust mass above the sublimation temperature.

Here, we assume a gas with a typical ISM dust-to-gas mass ratio of $\epsilon_0 = 0.01$ corresponds with a solar metallicity and that the total metallicity of the gas is proportional to the dust-to-gas mass ratio above the sublimation temperature, as the majority of molecules other than hydrogen and helium are frozen as ice onto the grains. As such, $\beta(Z_{\rm sub}) > \epsilon_0$ represent cases in which the gas is enhanced in CO, corresponding to a super-solar metallicity, and $f_{\rm CO} > 1$.

Because DustPy is a 1D simulation, we assume a vertical distribution of dust and grains from the surface density and gas scale height. The gas scale height, $h = c_s\Omega$ (where Ω is the local Keplerian frequency and c_s is the sound speed), is assumed from a E. I. Chiang & P. Goldreich (1997) like midplane temperature profile. The dust scale height, h_a, is written as in A. N. Youdin & Y. Lithwick (2007):

$$h_a = \sqrt{\frac{\delta}{\delta + {\rm St}_a}}h, \tag{4.3}$$

where δ is the vertical diffusivity of the dust and ${\rm St}_a$ is the Stokes number of a solid of size a. We define $\delta = f_\alpha \alpha$, where f_α is a dimensionless enhancement parameter to the vertical turbulence, to account for an increase in the vertical scale height of dust as a result of stirring via meridional flows exterior to the planet (J. Bi et al., 2021; J. Szulágyi et al., 2022). While this value of f_α is uncertain, we test a variety of values ranging from $1 \leq f_\alpha \leq 10$.

The enhancement in CO relative to the initial abundance, $f_{\rm CO}$, is plotted as a function of $Z_{\rm sub}/R$ at $R = 101$ au, the location of the pressure bump and dust trap for our DustPy simulations, in Figure 4.6. Here, we see that higher fragmentation velocities and stirring both tend to increase the mass of dust above the sublimation surface, and thus the expected abundance of gaseous CO. For $Z_{\rm sub}/R = 0.1$, as is the case for CO at 101 au, CO abundances directly exterior to the planet range from slightly sub-solar up to a maximum of $3\times$ solar abundance if $f_\alpha = 10$. While disk turbulence is difficult to constrain, observations of disks containing ring and gap structures have shown that some rings may be "puffier" than others, with vertical turbulence up to $\alpha \approx 10^{-2}$ (K. Doi, 2021; M.

Villenave et al., 2025), corresponding to $f_\alpha = 10$ in our model. We note that 30 K assumed here is likely an upper limit for the temperature of CO sublimation. If CO begins to sublimate off of the grain at lower temperatures, this will correspond with lower values of $Z_{\rm sub}$ and an increase of $\beta(Z_{\rm sub})$. Thus a lower sublimation temperature – and lower sublimation height in the disk – will increase the expected volatile enrichment onto the planet. A sublimation temperature of 25 K, for example, corresponds to $Z_{\rm sub}/R \approx 0.09$. For this lower sublimation temperature, and thus lower sublimation height, CO abundances range from solar up to 4× solar.

While low fragmentation velocities tend to create more small dust, the concentration of total solids in the pressure bump remains relatively low compared with the higher fragmentation velocity model (See Section 4.4.1 and Figure 4.2). For the high fragmentation velocity case, pebble growth and inward drift concentrates solids in the bump, leading to a higher total dust-to-gas mass ratio at this location. For the case with a fragmentation velocity of 10 m s^{-1}, this leads to a total enhancement of 14.5× the initial ϵ_0, shown as $f_{\rm CO}(Z_{\rm sub}/R = 0)$ in Figure 4.6. While higher fragmentation velocities lead to larger pebbles, the greater concentration of solids in the pressure bump also increases the mass of small dust, with the "tail" of the mass distribution towards smaller grains resulting in significant dust mass above 30 K even for the case with no additional vertical stirring ($f_\alpha = 1$).

The maximum enhancement to dust in the upper disk, and thus enhancement in CO gas, would occur from efficient inward drift of pebbles from the outer disk followed by fragmentation in the bump. We note that fragmentation in the pressure bump exterior to a giant planet is expected to be enhanced, due to increased relative velocities in the spiral arms (J. Drążkowska et al., 2019; L. E. J. Eriksson et al., 2024). Additional vertical stirring as a result of planetary meridional flows, as expected from 3D simulations (J. Bi et al., 2021; J. Szulágyi et al., 2022), will act to further increase the delivery of volatile ice above the CO snow surface.

The ingredients for the DRIVE mechanism are expected to be present regardless of where the planet forms. The detailed implications for the composition, including the C/O, of the planet will depend on its formation location relative to the various snow lines that would exist throughout the disk. For example, CO_2 may also sublimate off the lofted grains considered here, but due to its higher binding energy, will only do so for those grains that reach temperatures in excess of ∼50 K.

This would lead to a lower enhancement in CO_2 than CO because of the former's higher snow surface. Were the planet forming just outside the midplane CO_2 snow line, however, the planet may receive an enrichment in CO_2, while the CO would be present at roughly solar abundance as its snow line is located much further out in the disk and drifting pebbles would be absent of CO ice. If appreciable CO_2 is accreted along with CO, this would push the C/O of the planetary atmosphere below unity, possibly explaining C/O ratios near solar in wide-separation giant planet atmospheres (E. A. Bergin et al., 2024; E. Nasedkin et al., 2024).

Here we highlight the importance of the 2D snow *surface*, rather than focus on the midplane snowline. Previous studies have highlighted the "cold finger" effect, where dust growth and settling can deplete volatiles from the surface layer of the disk, enriching the midplane (R. Meijerink et al., 2009; S. Krijt et al., 2016; E. R. Van Clepper et al., 2022). In the presence of a giant planet, however, the dust pile-up will lead to frequent collisions and fragmentation, replenishing the supply of small grains exterior to the planet. These small grains cycle between the midplane and upper regions of the disk on 10 kyr timescales (less than the diffusive mixing time), carrying their volatile ice mantle with them. Here, grains sublimate their volatiles into the gas phase, creating a volatile rich gas environment above the snow surface. Given the giant planet accretes gas from above one scale height, this volatile rich gas will be readily accreted into the atmosphere of the giant planet.

4.4.4 Caveats to the model

The magnitude of the volatile delivery onto the planet will depend in detail on the production of fine dust from pebbles and the heating of that dust, which itself depends on the interplay between grain growth, fragmentation, transport, and heating in 3D. Modeling these processes together, however, is a computationally expensive task and will depend on many factors, including the disk mass, viscosity, accretion rate, and pebble flux. Here, we examine some of the assumptions and limitations of the modeling work presented here.

First, we assume that sublimated volatiles above the snow surface are accreted onto the planet. Hydrodynamic models of cooling giant planet atmospheres show that meridional flows are primarily recycling flows, with the majority of gas returning to the disk (H. Kurokawa & T. Tanigawa, 2018; A. P. Bailey & Z. Zhu, 2024). Nonetheless, any gas that is accreted onto the planet will come from the surface regions of the disk, which will be enhanced in volatiles as a result of the DRIVE mechanism. While only a small fraction of disk gas may ultimately be incorporated into the giant planet atmosphere, any disk gas that is incorporated will have an enhanced metallicity. Additionally, we emphasize the *recycling* nature of the DRIVE effect. In the case where volatile enriched gas is not accreted onto the planet or adsorbs onto another grain, that grain may be then cycle to the upper disk, desorbing volatiles into the gas phase again. While the overall metallicity enhancement onto the planet may require a detailed understanding of the gas accretion onto giant planets, the DRIVE mechanism presented here predicts that disk gas available for accretion should be enriched in volatiles above the snow surface by a factor of up to 3× solar.

We also examine our dust population assumptions from the 1D DustPy model presented in Section 4.4.1. In 2D, for example, when small solids are lofted they will collide with other small solids, resulting in growth via sweep-up. S. Krijt & F. J. Ciesla (2016) studied dust growth and settling in a 1D vertical slice of an axisymmetric disk in the absence of a planet. They showed that even for high dust-to-gas ratios up to 0.1, as would be expected in the pressure bump exterior to the planet, small dust grains can still reach heights up to the gas scale height before growing and settling back to the midplane. W. Misener et al. (2019) expanded this to a 2D disk ($R-Z$) including growth, fragmentation, settling, and drift, and showed similar results, with small grains typically reaching 1-2 gas scale heights in the disk shortly after a collision before growing and settling again. Here, though, we again emphasize the role of the meridional flows, which will serve to further increase the dust scale height, as shown here and in other work (J. Bi et al., 2021; J. Szulágyi et al., 2022). Thus, we expect even in the case of dust-sweep up at altitude, small grains should be able to deliver volatiles to the warm atmosphere of the disk.

These 3D models of dust transport around giant planet not only show that dust is puffed up at the edges, but also that small dust grains can be accreted onto the planet (J. Szulágyi et al., 2022; E. R. Van Clepper et al., 2025b) and that a dust envelope (or disk) may be expected around the embedded planet (J. Bi et al., 2021; L. Krapp et al., 2022). However, in the surface regions of the disk and in the gap near the planet, radiative transfer models predict that both temperatures and UV irradiation should be higher than elsewhere in the disk. (F. Alarcón et al., 2020; F. Alarcón & E. A. Bergin, 2024). Thus, except for the in the pressure bump where the grain may be recycled back into the DRIVE mechanism, the recondensation of sublimated volatiles onto grains is unlikely.

Next, we consider how this effect might operate at other snowlines throughout the disk. For grains to be heated as they are lofted in the disk, this requires the gas temperature to be lower at the midplane and higher at the surface of the disk. While this is true for disks where heating is primarily a result of irradiation, viscous heating at the midplane can also provide a source of heat. Viscous heating depends on the mass accretion rate and disk mass (N. Calvet et al., 1994), and as a result is more dominant in the inner disk where midplane densities are highest. As such, DRIVE should be most apparent in the outer disk, where the surface of the disk is hotter than the midplane. "Cold" snow surfaces, such as the CO and CO_2 sublimation fronts, are thus most likely to undergo this process of grain lofting and sublimation, while "hotter" snowlines, like the H_2O snowline or "soot line" (location of refractory carbon sublimation, M. E. Kress et al., 2010; J.-E. Lee et al., 2010; J. Li et al., 2021), are more likely to have colder disk surfaces, and thus may not be as susceptible to thermal desorption at the surface of the disk. Enhanced UV radiation at the surface of the disk, however, may drive grain chemistry including desorption in these regions (N. F. W. Ligterink et al., 2024). UV-driven photo desorption may lead to sublimation of even water ice, further increasing the metallicity and decreasing C/O of the disk gas.

Finally, as dust grains are the primary transport mechanism for volatiles in the DRIVE model, grain surface chemistry will play an important role setting the gas-phase volatile abundances. Irradiation, for example, may dissociate CO into atomic C and O, resulting in the production of secondary ice species with different binding energies (see, e.g., J. B. Bergner & F. Ciesla, 2021; N. F. W. Ligterink et al., 2024; A. J. Cridland et al., 2025). If the resulting primary C- and O-bearing have drastically different binding energies from one another (or from CO) then this may effect the resulting metallicity and C/O of volatiles sublimated from the grains and ultimately the planetary atmosphere. This will, however, depend on the relative timescales involved between grain surface and gas phase chemistry and optical depth of the dust, and should be studied in more detail using dynamic chemical models.

4.5 Comparison with other mechanisms

We present the DRIVE mechanism as an additional means by which giant planet atmospheres may become enriched in volatile species. While the different mechanisms of giant planet atmosphere enrichment are not mutually exclusive from one another, each may be dominant in different disk conditions and leave distinct traces of that formation pathway on the formed planet. In this section, we briefly summarize some such models and differences with our model presented here.

4.5.1 Pebble drift across snowlines

The process here is similar to the enrichment of volatiles at snowlines as a result of pebble drift (K. I. Öberg & E. A. Bergin, 2016; R. A. Booth et al., 2017; K. Zhang et al., 2020), although these models require the planet form interior to the snowline, while the DRIVE model presented here allows for planet to incorporate these volatile even when forming outside of the midplane snowline. Enrichment via pebble drift across snowlines requires large pebbles to drift past midplane snowlines, enhancing the abundance of a given volatile species and imprinting an atmospheric C/O based on the sublimated ices. Here, we enhance the gas-phase with volatile species via the vertical lofting of small grains above the snow surface. Additionally, the pebble drift model of enhancement would predict that CO should be enhanced in the inner disk as CO-rich pebbles drift across the CO snowline. Disk observations, however, have shown that CO is depleted rather than enhanced interior to the CO snowline (K. Zhang et al., 2019).

4.5.2 Planetesimal Accretion

Another way to enhance the metallicity of the atmosphere of giant planets is via accretion and ablation of planetesimals. If these planetesimals originate in the outer disk, then they may be volatile rich (S. Atreya et al., 1999). Jupiter, for example, may have formed in the outer disk, beyond the N_2 snowline, accreting C, N, and O from icy planetesimals (A. D. Bosman et al., 2019; K. I. Öberg & R. Wordsworth, 2019), before migrating to its current day location. This inward migration may further act to shepherd planetesimals onto the planet, enriching the envelope of closer in exoplanets (S. Shibata et al., 2020, 2022) and Jupiter (S. Shibata & R. Helled, 2022) if it migrated in from the outer disk. If these planetesimals retain all volatiles during their accretion, then this may lead to decreased C/O of the planetary atmosphere closer to solar values. This assumes there are ample planetesimals in the disk to be accreted, however dynamical models show scattering, rather than accretion, may dominate interactions between planets and planetesimals (L. E. J. Eriksson et al., 2022).

An important aspect of the DRIVE model is the separation of volatiles from their refractory carriers, resulting in preferential accretion of volatiles over solid dust grains. This refractory-to-volatile ratio in the atmospheres of planets is expected to differ depending on the mechanism of enrichment (J. D. Lothringer, 2021). Thus this refractory-to-volatile ratio may help to differentiate between planetesimal accretion, pebble accretion, and the DRIVE mechanism . The DRIVE model presented here provides a novel way to transport volatile carbon and oxygen from the outer disk into the atmosphere of an accreting giant planet, providing a new mechanism to set the C/O and metallicity of giant planet atmospheres separate distinct from planetesimal accretion models.

4.5.3 Heating from the planetary embryo

We emphasize that DRIVE does not require solids to filter through the gap, nor pass within the envelope of the embedded planet. Previous studies have shown that pressure traps may be "leaky" and small particles may filter from the outer disk to the inner disk (C. P. Dullemond et al., 2018; P. Weber et al., 2018; T. Haugbølle et al., 2019; S. M. Stammler et al., 2023; E. M. Price et al., 2025; E. R. Van Clepper et al., 2025b). In doing so, they may pass by the luminous, embedded planet (H. J. Petrovic et al., 2024), heating those grains and sublimating ice back to the disk (M. N. Barnett & F. J. Ciesla, 2022; H. Jiang et al., 2023; Y. Wang et al., 2023; A. J. Cridland et al., 2025). Additionally, in 3D, accreted grains tend to pass near the planet following the gas accretion flow, which transports grains near the surface of the disk (J. Szulágyi et al., 2022; H. J. Petrovic et al., 2024; E. R. Van Clepper et al., 2025b). As a result, even when grains are accreted onto the planet, some amount of thermal processing, including sublimation of the ice mantle, is likely to occur during this accretion phase. In the DRIVE mechanism presented here, solids are heated by irradiation from the host star at the atmosphere of the disk rather than from the planet itself, and thus is not dependent on the amount of solid mass that may pass the growing the planet. In this way, the DRIVE mechanism does not depend on the "leakiness" of the gap, and is expected to function in either strong or weak pressure bumps.

4.6 Conclusion

In this work, we present a novel method to enrich the atmospheres of cold giant planets with volatiles, increasing their bulk metallicity. This "Dust Recycling and Icy Volatile Enhancement" (DRIVE) effect relies on the following disk processes to occur:

1. Dust and pebbles are concentrated at the local pressure maxima exterior to the gap carved by a giant planet due to inward drift of icy pebbles from the outer disk.

2. Small dust is created via pebble fragmentation, which is transported upwards through diffusion and advection via the meridional flows created by the planet and exposed to higher temperatures at the surface of the disk, resulting in the sublimation of volatiles into the gas phase.

3. The giant planet accretes gas from above one scale height in the disk, which has been enriched in volatiles sublimated from the small dust.

All of these are expected via the current understanding of giant planet formation, and combined will enrich giant planet atmospheres with volatiles, even after the planet has reached the pebble isolation mass and outside the midplane snowline. Similar to how radial drift can enrich volatile abundances interior to midplane snowlines, we expect that this combined fragmentation and lofting should increase volatile abundances above the snow surface as well. While some of the sublimated volatiles may diffuse downward and re-freeze onto grain surfaces, these grains will continue to cycle back to the upper region of the disk, sublimating volatiles again. For the example considered here, this concentration of dust in the pressure bump may lead to enhancements of up to 3× Solar abundance of CO above the snow surface. This late stage metallicity enhancement in the accretion of giant planets may explain the recently shown relationship between mass and metallicity, indicating a super-solar metallicity in even the most massive giant planets (Y. Chachan et al., 2025).

Under the DRIVE mechanism, we expect wide separation giant planets to become enriched in volatile C and O, increasing measured metallicity in their atmospheres. This effect may explain the observed mismatch between gas-phase composition of disks and atmospheric composition of cold giant planets, which are currently difficult to explain using either pebble or planetesimal accretion models (E. A. Bergin et al., 2024; E. Nasedkin et al., 2024; W. O. Balmer et al., 2025). Additionally, DRIVE provides a novel way to separate volatile ice from refractory carriers. Thus, bulk metallicity measurements of exoplanets inferred from single molecular abundances may not reflect this partitioning, and refractory-to-volatile ratios may be key in understanding giant planet formation history (J. D. Lothringer, 2021; J. D. Lothringer et al., 2025). Jupiter's enhanced metallicity, for example, is largely based on the enhancement of volatile species, including noble gasses, carbon, nitrogen, and oxygen (see, S. K. Atreya et al., 2020, and references therein). Understanding the relative composition of refractory elements will be key to understanding Jupiter's bulk metallicity and differentiating possible origin scenarios.

While we have explored the dust growth and fragmentation, disk hydrodynamics, radiative transfer, and particle dynamics separately here, there are important feedback mechanisms that may affect the magnitude of the DRIVE effect. The chemistry of the disk is sensitive to the small dust, which is the primary carrier of volatiles, which may act to further alter the C/O and metallicity of the gas near the growing planet. This dust, however, is intricately linked to the gas dynamics, which is in turn driven by interactions with the embedded planet. This small dust also serves as the primary source of opacity in the disk, feeding back on the thermal structure and UV driven chemistry in the disk. Better understanding the evolution of dust in a disk containing an embedded planet will provide many future avenues of research with implications for the chemistry and dynamics of disks and the planets that form within.

CHAPTER 5
CONCLUSION AND FUTURE WORK

Throughout this work, it is clear that planet growth feeds back onto the chemistry of the disk in ways that must be accounted for when modelling PPD evolution and planet formation. In Chapter 2, I showed that dust grain growth can have dramatic effects on the gas phase chemistry of the disk, both by sequestering oxygen-rich ices and reducing the UV opacity, driving photo-chemistry closer to the midplane. While this may affect what is observable in the gas phase of disks around other stars, the pebbles – that is the solid feedstock of planetesimals – incorporate the integrated composition of solids throughout their lifetimes. In the models presented here, dust growth is most efficient early when small dust abundance is high. Because of this, pebbles largely inherit the composition of the early protostellar cloud. This points to a disconnect between the observed gas phase of the disk and the composition of planetesimals forming within. This important effect had not previously been appreciated in chemical models, where it is common to simulate static disks over the lifetime of the disk and assume planetesimals reflect the composition of the solids after evolution. Rather, the composition of planetesimals, including meteorites in our solar system, reflect the *evolving* composition throughout the lifetime of the disk.

From the results of this work, we have argued for an inherited oxygen isotopic composition from the protosolar cloud, rather than processing in the solar nebula to explain the observed oxygen isotope composition of meteorites (F. J. Ciesla et al., 2026). This is because dust is the primary source of opacity for UV radiation, and so an increase in UV-driven chemistry is necessarily tied to a decrease in the small dust abundance.

However, if dust grains undergo episodes of growth and fragmentation then this may provide an avenue for photo-processed gas phase molecules to freeze out onto grains. A cycle of grain growth and fragmentation would replenish small dust grains, providing a grain surface sink for gas that has been processed after the initial dust settling and growth phase. One possible mechanism for this fragmentation in disks may be the spiral arms created by embedded giant planets, which can increase local relative velocities between solids making fragmentation collisions more likely (e.g. L. E. J. Eriksson et al., 2024). This is an exciting avenue of research and points to the importance of modeling dust growth and fragmentation consistently with the gas-phase chemistry in protoplanetary disks.

In Chapter 3, I presented the results of combined hydrodynamic and Monte Carlo particle tracking simulations. I showed that the ability of Jupiter to act as a barrier to inward drift is dependent on the planet mass, disk viscosity, and the size distribution of dust grains. Unlike simple 1D models which predict a complete halt of dust grain drift above the pebble isolation mass of the planet, I showed that small dust grains are not only able to filter past the planet, but in fact accretionary meridional flows increase the inward transport of dust grains compared to lower planet masses. Such filtering may be critical for understanding the selective transport of chondrules and refractory inclusions between NC and CC reservoirs, which show evidence for both inwards and outwards transport. The results of this chapter conclusively show not only that an early jovian embryo can facilitate *both* inwards and outwards transport across the gap, but also can selectively filter small CAIs from the outer disk to the inner disk, matching observed trends in NC and CC parent bodies (E. T. Dunham et al., 2023).

Using the mass evolution of Jupiter as a proxy for time in the solar nebula, these results may be used in future studies to more directly match filtering of specific parent body components with formation ages of meteorite parent bodies (see, e.g., recent work by N. Gurrutxaga et al., 2026). While this chapter is primarily focused on the growth and evolution of Jupiter in the solar nebula, these results can be generalized for giant planet formation in extrasolar disks, and have direct applications for constraining recent observations of possibly leaky gaps in PPDs (A. Banzatti et al., 2025; N. T. Kurtovic et al., 2025; A. Sierra et al., 2025).

Following on these results, in Chapter 4 I modeled the transport of small dust grains in a pressure bump outside of a giant planet near the CO snowline. Here, I showed that dust circulates between the optically thick midplane and more chemically active surface of the disk. This dust recycling and icy volatile enhancement (DRIVE) effect enhances volatiles above their snow surfaces where they may be accreted by the giant planet. Recently, E. A. Bergin et al. (2024) highlighted the fact that disk observations have shown that the outer disk appears to be highly reducing with C/O ratios much greater than unity, and depleted in carbon and oxygen, indicating a subsolar metallicity. Despite these observations, the atmospheres of wide-separation giant planets, which presumably formed in the outer disk, have lower C/O ratios and a range of metallicities. In fact, a recent reanalysis of giant exoplanet atmospheres has shown that even the most massive exoplanets have metallicities much higher than would be predicted if they were accreting pure nebular gas, as is expected from the core accretion hypothesis (Y. Chachan et al., 2025; J. W. Xuan et al., 2026). This newly identified DRIVE effect may explain this observed mismatch between wide-separation giant planet atmospheres and PPD gas compositions in the outer disk.

It is clear from this collection of work, that growing planets feedback onto the chemistry of the disk in many ways, from the earliest growth of dust grains into larger pebbles, through the feedback of giant planets stirring solids and altering their own chemical environment. The holistic approach to planet formation dynamics and chemistry put forward in this thesis is a necessary step for better connecting planets to their formation environment. In the following sections, I highlight two particularly exciting avenues for further research that highlight the interplay between dust dynamics, growing planets, and chemistry.

5.1 Constraining Leakiness in Planet-Induced Dust Traps

While there has been recent work pointing to the fact that some dust traps are leaky (P. Weber et al., 2018; T. Haugbølle et al., 2019; S. M. Stammler et al., 2023, and work presented here in Chapter 3), it is still a major question of *which* traps might be leaky, and *how much material* is expected to filter past a planet. Although the Solar System was separated early into distinct NC and CC reservoirs, at the same time there is evidence for mixing of CAIs and chondrules throughout the solar nebula (as discussed in Chapters 1 and 3). This degree of mixing is inherently tied to the growth of the giant planets, but connecting meteorite formation to the timing of Jupiter's formation depends on understanding the growth, fragmentation, and transport of these meteorite components and their eventual parent bodies.

As recently showed by A. Houge et al. (2026), the degree of leakiness from planet induced dust traps depends not only on disk and planet parameters, but also on the growth and fragmentation of dust in the pressure bump exterior to the planet. While this has been modeled using 1D grain growth simulations, these fail to account for the 3D structure and flows induced by an embedded planet. I have shown that understanding this gas advection is necessary for accurate modeling of dust transport across gaps and must be accounted for in dust coagulation models.

Understanding this interplay between dust and embedded planets may also provide another avenue to identify embedded exoplanets in extrasolar disks. The recent AGE-PRO survey, which examined dust masses for disk populations at various ages, showed that while some pressure bumps may be effective barriers to dust drift and transport, other are consistent with “weak” trapping, indicating some degree of leakiness across dust traps (N. T. Kurtovic et al., 2025). If the presence of a sufficiently massive planet increases the leakiness of traps, as indicated by results in Chapter 3 in this work, then identification of these substructures may hint that they are indeed caused by giant planets. Otherwise, alternative ring and gap formation mechanisms (e.g. gravitational instability, (magneto-)hydrodynamic effects, or alternative dust processes; see J. Bae et al., 2023) may be favored.

5.2 Chemical Processing in Dust Rings and Gaps

Throughout this thesis, I have shown the importance of understanding the interplay between dynamics and chemistry as it relates to the process of planet formation. In light of this, it is natural to ask how these leaky gaps may feed back onto the composition of the disk. This processing may occur during the transport of dust grains through the gap or via circulation in the pressure bump, similar to the DRIVE effect discussed in Chapter 4.

Currently, water vapor is used as a proxy for pebble drift across gaps, with water emission from the inner disk assumed to come from water rich pebbles migrating from the colder outer disk carrying water-ice to the warm inner disk where sublimation may be observed (A. Banzatti et al., 2025; S. Krijt et al., 2025). This assumes, however, that water bearing grains remain relatively unaltered, despite temperatures and irradiation drastically increasing in the gap (F. Alarcón et al., 2020; F. Alarcón & E. A. Bergin, 2024). While static chemical models predict active chemistry in these substructures as a result of these different conditions (e.g. F. Alarcón et al., 2020), dust grains crossing the gap tend to do so quickly (Chapter 3, this thesis) and thus may not be exposed to these conditions long enough for a chemical imprint to be made. A comprehensive study of the processing of solids in these gaps is necessary to constrain these models of volatile ice transport throughout the disk.

In addition to processing in the gap, dust grain circulation in the pressure bump can also expose dust grains to the surface of the disk, where temperatures and radiation fields are higher and chemistry is expected to be more active. In Chapter 4, I discuss how this may lead to ice sublimation and enrichment of volatiles in the atmosphere of giant planets. However, such process may have a variety of chemical effects, resulting in the sublimation and processing of various volatiles in the disk, or the formation of more complex molecules, including organic matter, which have been observed in meteorite and asteroid samples and may serve as an important source of organic carbon for the early Earth (J. F. Kerridge, 1993; C. M. O'D. Alexander et al., 2017; H. Naraoka et al., 2023; D. P. Glavin et al., 2025).

Pressure bumps have been theorized as an ideal location in PPDs for the formation of organic molecules as small grains circulate between the midplane and disk surface, transporting simple ices to irradiated zones, resulting in the formation of complex organic molecules (COMs) (N. van der Marel et al., 2021; N. F. W. Ligterink et al., 2024; N. van der Marel et al., 2026). Laboratory experiments have shown that under UV irradiation mixtures of simple ISM ices can produce complex molecules, including amino acids and carbohydrates (e.g. W. Hagen et al., 1979; G. M. Muñoz Caro et al., 2002; L. I. Tenelanda-Osorio et al., 2022; C. C. Sarver et al., 2026). However, modeling efforts to connect this formation to specific locations in PPDs, such as pressure bumps, have relied on simple 1D approximations and have not accounted for the additional 3D stirring expected from giant planets.

Previously, F. J. Ciesla & S. A. Sandford (2012) showed that even in a disk not containing a giant planet, micron-sized dust particles can experience sufficient photon fluxes for macromolecular formation from interstellar ices. This is due purely to turbulent diffusion driving these small dust grains near the surface of the disk, where UV photon flux is highest. However, as shown in Chapters 3 and 4 here, planetary flows can puff up dust in pressure traps, further exposing these grains to additional UV photons, increasing the efficiency of COM formation on dust grain surfaces. This formation pathway for COMs in pressure bumps relies on temperatures remaining low enough for volatile ices (e.g. CO, H_2O, NH_3) to remain on the grain surfaces. If grains are exposed to increased temperatures, or sufficiently high UV fluxes to result in photo-desorption, then COM formation may be inhibited rather than facilitated in these pileups.

Understanding these important effects for the formation and transport of complex molecules requires a more detailed understanding of the combined chemistry and dynamics in protoplanetary disks, and how these processes evolve over the lifetime of the disk. In this thesis I have shown that the act of planet formation feeds back in non-trivial ways to the global disk structure, both in the distribution and composition of the solids and gas. Recent results from cosmochemistry, astrochemistry, and (exo-)planetary science have shown that planet formation is a complex, prolonged process. To better connect planets to their formation histories and environments, models accounting for these feedbacks between planets, chemistry, and dynamics must be considered.

APPENDIX A
CANDY CHEMICAL MODEL AND MODEL SENSITIVITY

A.1 Description of Chemical Model

Our chemical model is built on top of the `astrochem` numerical solver, with added gas phase reactions including self-shielding and excited H_2. Gas-grain reaction rates are calculated following R. Visser et al. (2009) such that the desorption and hydrogenation rates for each species are limited by the species abundance in the ice and the number of monolayers allowed to desorb from the grain. Hydrogenation is limited to the reactions listed in Table A.1 as in R. Visser et al. (2009). These adjustments make our complete chemical solver more similar to the DALI code S. Bruderer et al. (2012) while maintaining the ease of use of the `astrochem` solver.

A.1.1 Gas phase reactions

The majority of gas phase reactions follow directly from the UMIST database (D. McElroy et al., 2013), from which the α, β, and γ coefficients for all reactions are taken. For reactions involving two gas species, the reaction rate constant, k is given by the formula

$$k = \alpha \left(\frac{T}{300\ \mathrm{K}} \right)^{\beta} \exp\left(\frac{-\gamma}{T} \right)\ \mathrm{cm^3 s^{-1}}. \tag{A.1}$$

Reactions involving cosmic rays have a rate coefficient given by

$$k = \alpha \frac{\zeta}{\zeta_0} \frac{\gamma}{1-\omega} \left(\frac{T}{300\ \mathrm{K}} \right)^{\beta}\ \mathrm{s^{-1}} \tag{A.2}$$

where ζ is the cosmic ray ionization rate and $\zeta_0 = 1.3 \times 10^{-17}$ is taken as the standard ionization rate. The FUV dust albedo, ω is assumed to be equal to 0.5 for all cosmic-ray reactions.

C	→	CH	→	CH_2	→	CH_3	→	CH_4
N	→	NH	→	NH_2	→	NH_3		
O	→	OH	→	H_2O				
S	→	HS	→	H_2S				

Table A.1: Hydrogenation reactions included in the network

Modifications to the UMIST reaction rate library involve self-shielding and excited H_2 reactions. All reactions involving UV photons take the form

$$k = \Theta \alpha \chi \exp\left(-\gamma A_v\right)\ \mathrm{s}^{-1} \tag{A.3}$$

where χ is the unattenuated UV intensity and $A_v = \tau_{UV}/3.02$ is the visual extinction. The shielding factor, Θ, is equal to one for all reactions except for photodissociation of CO and H_2. For these shielded reactions, the column densities of CO and H_2 above the given location is calculated and the self-shielding factor is determined from R. Visser et al. (2009) for CO dissociation and B. T. Draine & F. Bertoldi (1996) for H_2.

Excited gas phase hydrogen reactions involve reactions with H_2 that has been vibrationally excited by UV radiation. This vibrational excitation allows the H_2 molecules to overcome reaction barriers of otherwise endothermic reactions. Although H_2 can be excited into a number of vibrational states, we follow R. Visser et al. (2018) and consider a separate species of H_2 excited to a weighted average vibrational pseudo-level of $\nu = 6$ or $E/k = 30163$ K, and spontaneous decay rate of 2×10^{-7} s^{-1}. The rate of H_2 excitation is a combination of excitations from UV pumping, collisions with H_2 and H, and temperature. Similarly, the de-excitation rate is a combination of spontaneous decay, FUV pumping, and collisions. The rate of collisions, q, is given by the formula

$$\log\left(\frac{q}{\mathrm{cm}^3\mathrm{s}^{-1}}\right) = a + \frac{b}{t} + \frac{c}{t^2} \tag{A.4}$$

where $t = 1 + T/(1000\ \mathrm{K})$ and the coefficients a, b, and c, are fit from J. Le Bourlot et al. (1999) for both H_2-H and H_2-H_2 collisions. The rate of excitation then is given by

$$k_{ex} = 10k_{\mathrm{diss}} + (q_{(H_2-H)}n_H + q_{(H_2-H_2)}n_{H_2})\exp\left(\frac{-30163\ \mathrm{K}}{T}\right)\ \mathrm{s}^{-1} \tag{A.5}$$

where k_{diss} is the rate of UV dissociation of H_2. Similarly the rate of de-excitation is given by

$$k_{dex} = 10k_{\mathrm{diss}} + (q_{(H_2-H)}n_H + q_{(H_2-H_2)}n_{H_2}) + 2 \times 10^{-7}\ \mathrm{s}^{-1}. \tag{A.6}$$

Reactions between excited H_2 and other gas phase species follow a modified version of equation

A.1 to account for the vibrational energy of the excited H_2 molecule

$$k = \alpha \left(\frac{T}{300\ \mathrm{K}}\right)^{\beta} \exp\left(\frac{-(\gamma - 30163)}{T}\right)\ \mathrm{cm^3 s^{-1}}. \tag{A.7}$$

A.1.2 Gas-grain reactions

Gas-grain reactions for our modified network include freeze-out, thermal desorption, photodesorption, and hydrogentation. We follow the reaction rates of R. Visser et al. (2011), however we allow for desorption of two monolayers at a time from the grain surface, doubling the number of binding sites available for desorption and hydrogenation reactions. Our reaction rates for thermal desorption, photodesorption, and hydrogentation follow equations (4), (6), and (7) of R. Visser et al. (2011) respectively. In our model, however, the total number of binding sites per grain is given by

$$N_b = 4\pi a_{gr}^2 N_{ss} N_{des} \tag{A.8}$$

where a_{gr} is the grain radius, $N_{ss} = 8 \times 10^{14}\ \mathrm{cm^{-2}}$ is the number of binding sites per unit grain surface, and $N_{des} = 2$ is the number of layers allowed to desorb. Binding energies of ice species are taken from the UMIST12 database (D. McElroy et al., 2013).

A.2 Sensitivity to physical parameters

A.2.1 CO depletion

While depletion of CO outside of the snowline is a robust outcome of our model, the extent of the depletion depends on physical parameters of the disk, such as the turbulence, α, pebble growth rate, a (see Eq. 2.11), and location of pebble formation h_{form}. The dependence of CO depletion on α is discussed in Section 2.5, and we elaborate on the dependence of a and h_{form} here. Figure A.1 shows the dependence of CO depletion on a and h_{form} for α values of 10^{-3} and 10^{-4}.

The consequences of slower growth are shown by the dark purple dashed line in Figure A.1 as we increase the dust growth timescale, a, by an order of magnitude. As expected, slower dust growth leads to less loss of CO around the midplane. Further, the slower growth leaves the disk more optically thick to penetrating radiation, resulting in a diminished level of photoprocessing in

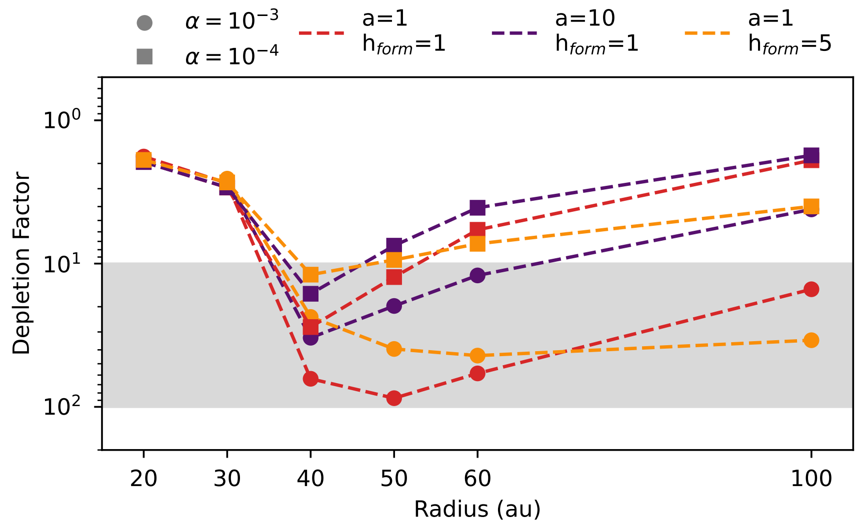

Figure A.1: Depletion of carbon monoxide in the warm molecular layer (as in Figure 2.8) for various model values of turbulence (α), pebble growth rate (a), and pebble formation region (h_{form}). Observed depletion factors of 10-100× below ISM values are indicated by the grey region as in Figure 2.8.

the upper layers of the disk.

To ensure that the details of depletion are not dependent on our choice of where we allowed pebbles to form, we also carried out a simulation where pebbles formed throughout the entire column of the disk (h$_{form}$=5, Figure A.1, orange line). In the cold outer disk regions CO remains frozen up to high elevations, so CO depletion is more efficient in this case. By contrast, around the radial snowline location (40 au) the CO snow surface is closer to the midplane, so forming pebbles at higher elevations does not enhance CO depletion. In fact, the removal of dust grains bare of CO ice at the upper layers of the disk decreases the amount of CO that is eventually depleted via pebble growth.

A.2.2 C/O ratios

Figure A.2 summarizes the column-averaged C/O ratios for different volatile components in the fiducial model. Given the that the physical conditions in a disk will be critical in setting the chemical evolution that occurs, we next explore whether changes to disk conditions may allow for higher C/O ratios to be reached than found here. We focus primarily on the conditions around 30

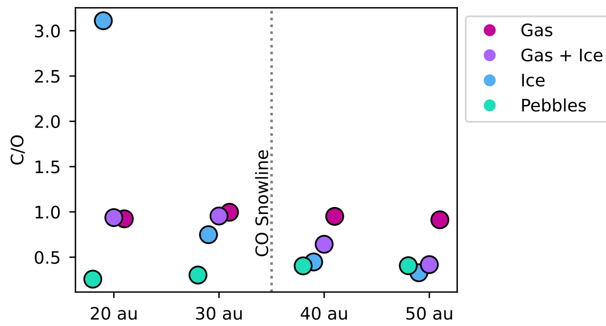

Figure A.2: Column averaged C/O ratios at 20, 30, 40, and 50 au. In general, the C/O ratios in the upper regions of the disk are the same as the bulk "Gas + Ice" ratio, while the gaseous C/O is dominated by gas phase CO at the midplane.

au as this is where the highest C/O ratios were found in our model, but note most observations at millimeter wavelengths are not sensitive to regions within the CO snowline. Nonetheless, our goal is to find what conditions allow high C/O ratios to develop in the most favorable region of the disk. We present the column averaged gas, ice, and total (gas + ice) C/O ratios and note that in the upper layers of the disk dust grains are largely devoid of icy mantles, and the conditions there are set by the gas.

Cosmic-ray ionization

Cosmic rays are important drivers of chemistry in the outer regions of protoplanetary disks. The effects of different cosmic ray ionization rates on C/O ratios are shown in Figure A.3, which again plots the column averaged C/O ratios for the gas, ice, total (gas+ice), and pebbles at 30 au, assuming different cosmic ray ionization rates. As the ionization rate increases, the C/O ratio of the pebbles increases slightly. This is because the secondary carbon products are available at earlier times, allowing them to be incorporated into forming pebbles. The lower ionization rates lead to slower chemistry, and the products of cosmic-ray driven reactions are formed after pebble growth has peaked.

At higher ionization rates, the removal of secondary carbon products via pebble growth leaves the remaining total column with a smaller C/O ratio. The total C/O value is very close to the gas value for the lowest ionization rate, and to the ice value for the highest ionization rate, as high ionization rates drive reactions that preferentially remove elements from gaseous molecules

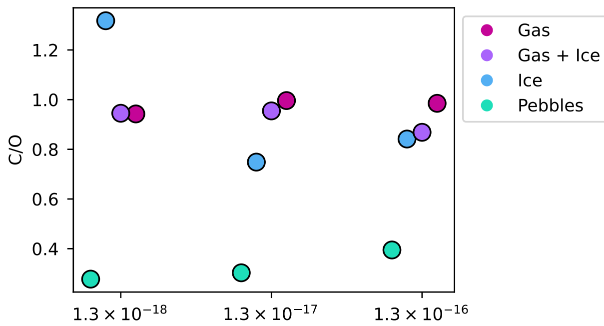

Figure A.3: Column averaged C/O ratios after 1 Myr at 30 au for differing cosmic ray ionization rates in s^{-1}. Although we achieve C/O>1 for the lowest ionization rate, the abundance of ice species is very low, and the combined gas and ice C/O remains below unity.

and incorporating them into less volatile ices. However, the total C/O ratio varies by only ~10% over a range spanning three orders of magnitude in the ionization rate, suggesting that the resulting ratio is not highly sensitive to this parameter.

UV radiation

The amount of photoprocessing in the PDL is set, in part, by the intensity of the UV radiation field. We varied the ambient field from $\chi = 5$ and 500 Draine units, representing a factor of 10 decrease and increase from the fiducial $\chi = 50$. The results are shown in Fig A.4, which again shows the C/O ratio among the different volatile components in the column at the end of the simulations. The differences are relatively small, particularly for the pebbles and gas. Thus, the incident UV field does not strongly impact the composition of material incorporated into planetesimals at the midplane. Indeed, the midplane is largely protected from UV radiation, and most of the pebble mass forms before photoprocessed material is mixed down to the midplane.

Growth & dynamics

As discussed above, disk chemical evolution is also controlled by the amount of dust present and the level of mixing, as dust grain abundances set the level to which photons can penetrate inside of the disk and the available sites for gas-grain chemistry to occur. As such, we altered the dust growth time scale and level of turbulence to evaluate how they impacted the C/O ratios. Figure A.5 shows the C/O ratios for α values of 10^{-3} and 10^{-4}, and growth timescale parameters of $a = 1$ (rapid)

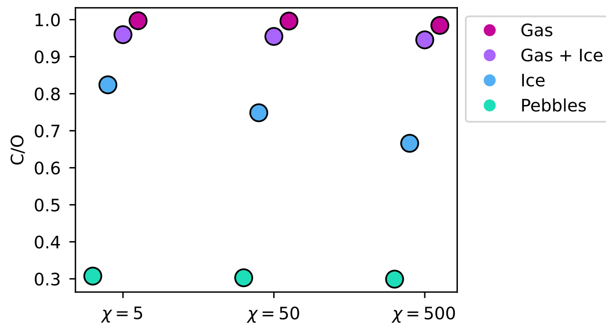

Figure A.4: C/O ratios after 1 Myr evolution with UV fields at 5, 50, and 500 times interstellar value in Draine units

and $a = 10$ (slower).

Increasing the growth timescale (a in equation 2.11) slows the removal of small dust from the column. This has the effect of 1) slowing the removal of oxygen via ice sequestration, and 2) slowing dust depletion and thus inhibiting photoprocessing in the PDL. These two effects together keep the gas C/O ratio near unity as CO remains abundant in the column. Meanwhile, the slow removal of oxygen rich ices means that the C/O ratio in the ice is lower, and that the ice remains a more significant component of the total volatile budget in the column. This is reflected in the lower total (gas + ice) C/O ratio of the a=10 case.

Decreasing the the level of turbulence from 10^{-3} to 10^{-4} slows the diffusion of material from the upper regions of the disk to the pebble forming midplane. Because small grains are less efficiently mixed downwards, optical depths remain high in upper regions of the disk. Additionally, H_2O on these grains is not carried downward as quickly to the pebble forming region, resulting in less removal of H_2O and, by extension, oxygen. These effects combine to reduce the total C/O ratio in the disk at 1 Myr compared to the α=10^{-3} case, with gas, ice, and bulk C/O ratios below unity.

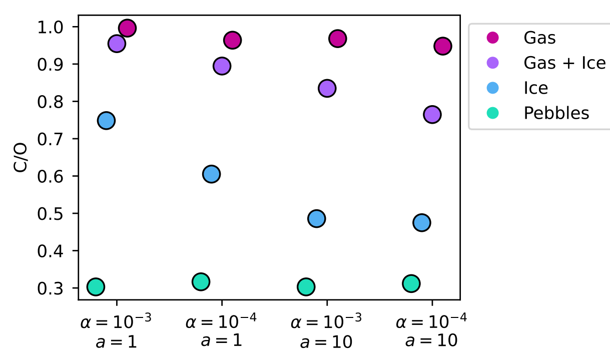

Figure A.5: C/O values for different alpha and growth timescale parameters of the disk. Decreasing alpha and increasing the growth timescale both have the net effect of lower the C/O ratio at 1 Myr of evolution.

APPENDIX B
FARGO SIMULATIONS

B.1 HD Disk Structure

The modeled disk has the surface density and scale height relation as given in Section 3.3.1, with surface density power-law slope $b = -1$, aspect ratio $A = H/R_0 = 0.05$, and flaring index $\gamma = 1/4$. Initially, the disk is axisymmetric (and thus independent of azimuthal angle ϕ) and in hydrostatic equilibrium. The density of each cell at radius r and polar angle θ is given by

$$\rho(r, \theta) = \frac{\Sigma_0}{\sqrt{2\pi}} \frac{1}{R_0 A} \left(\frac{r}{R_0} \right)^{-\xi} \sin(\theta)^{-\xi-\beta} \exp \left[\left(1 - \sin(\theta)^{-2\gamma}\right) / 2\gamma h^2 \right] \tag{B.1}$$

where

$$\xi = b + 1 + \gamma \tag{B.2}$$

$$\beta = 1 - 2\gamma \tag{B.3}$$

$$h = \frac{H}{r} = A \left(\frac{r}{R_0} \right)^{\gamma} \tag{B.4}$$

The FARGO3D setup file can be provided upon request.

REFERENCES

Aikawa, Y., & Herbst, E. 2001, "Two-dimensional Distributions and Column Densities of Gaseous Molecules in Protoplanetary Disks: II. Deuterated Species and UV Shielding by Ambient Clouds," *Astronomy & Astrophysics*, **371**, 1107, doi: 10.1051/0004-6361:20010416

Alarcón, F., & Bergin, E. A. 2024, "Thermal Structure and Millimeter Emission from a Protoplanetary Disk with Embedded Protoplanets from Radiative Transfer Modeling," *The Astrophysical Journal*, **967**, 144, doi: 10.3847/1538-4357/ad3d57

Alarcón, F., Teague, R., Zhang, K., Bergin, E. A., & Barraza-Alfaro, M. 2020, "Chemical Evolution in a Protoplanetary Disk within Planet Carved Gaps and Dust Rings," *The Astrophysical Journal*, **905**, 68, doi: 10.3847/1538-4357/abc1d6

Alexander, C. M. O'D., Cody, G., De Gregorio, B., Nittler, L., & Stroud, R. 2017, "The Nature, Origin and Modification of Insoluble Organic Matter in Chondrites, the Major Source of Earth's C and N," *Geochemistry*, **77**, 227, doi: 10.1016/j.chemer.2017.01.007

ALMA Partnership, Brogan, C. L., Pérez, L. M., et al. 2015, "The 2014 ALMA Long Baseline Campaign: First Results from High Angular Resolution Observations Toward the HL Tau Region," *The Astrophysical Journal*, **808**, L3, doi: 10.1088/2041-8205/808/1/L3

Andama, G., Ndugu, N., Anguma, S. K., & Jurua, E. 2022, "The Role of Density Perturbation on Planet Formation by Pebble Accretion," *Monthly Notices of the Royal Astronomical Society*, **512**, 5278, doi: 10.1093/mnras/stac772

Anderson, D. E., Bergin, E. A., Blake, G. A., et al. 2017, "Destruction of Refractory Carbon in Protoplanetary Disks," *The Astrophysical Journal*, **845**, 13, doi: 10.3847/1538-4357/aa7da1

Andrews, S. M., Huang, J., Pérez, L. M., et al. 2018, "The Disk Substructures at High Angular Resolution Project (DSHARP). I. Motivation, Sample, Calibration, and Overview," *The Astrophysical Journal*, **869**, L41, doi: 10.3847/2041-8213/aaf741

Armitage, P. J. 2017, "Lecture Notes on the Formation and Early Evolution of Planetary Systems," *arXiv:astro-ph/0701485*. http://arxiv.org/abs/astro-ph/0701485

Atreya, S., Wong, M., Owen, T., et al. 1999, "A Comparison of the Atmospheres of Jupiter and Saturn: Deep Atmospheric Composition, Cloud Structure, Vertical Mixing, and Origin," *Planetary and Space Science*, **47**, 1243, doi: 10.1016/S0032-0633(99)00047-1

Atreya, S. K., Hofstadter, M. H., In, J. H., et al. 2020, "Deep Atmosphere Composition, Structure, Origin, and Exploration, with Particular Focus on Critical in situ Science at the Icy Giants," *Space Science Reviews*, **216**, 18, doi: 10.1007/s11214-020-0640-8

Bae, J., Isella, A., Zhu, Z., et al. 2023, "Structured Distributions of Gas and Solids in Protoplanetary Disks," in Astronomical society of the pacific conference series, Vol. 534, Protostars and planets VII, ed. S. Inutsuka, Y. Aikawa, T. Muto, K. Tomida, & M. Tamura, 423, doi: 10.48550/arXiv.2210.13314

Bae, J., & Zhu, Z. 2018, "Planet-driven Spiral Arms in Protoplanetary Disks. I. Formation Mechanism," *The Astrophysical Journal*, **859**, 118, doi: 10.3847/1538-4357/aabf8c

Bae, J., Zhu, Z., & Hartmann, L. 2017, "On the Formation of Multiple Concentric Rings and Gaps in Protoplanetary Disks," *The Astrophysical Journal*, **850**, 201, doi: 10.3847/1538-4357/aa9705

Bailey, A. P., & Zhu, Z. 2024, "Growing Planet Envelopes in Spite of Recycling Flows," *Monthly Notices of the Royal Astronomical Society*, **534**, 2953, doi: 10.1093/mnras/stae2250

Balmer, W. O., Kammerer, J., Pueyo, L., et al. 2025, "JWST-TST High Contrast: Living on the Wedge, or, NIRCam Bar Coronagraphy Reveals CO_2 in the HR 8799 and 51 Eri Exoplanets' Atmospheres," *The Astronomical Journal*, **169**, 209, doi: 10.3847/1538-3881/adb1c6

Banzatti, A., Salyk, C., Pontoppidan, K. M., et al. 2025, "Water in Protoplanetary Disks with JWST-MIRI: Spectral Excitation Atlas and Radial Distribution from Temperature Diagnostic Diagrams and Doppler Mapping," *The Astronomical Journal*, **169**, 165, doi: 10.3847/1538-3881/ada962

Barbato, D., Sozzetti, A., Desidera, S., et al. 2018, "Exploring the Realm of Scaled Solar System Analogues with HARPS," *Astronomy & Astrophysics*, **615**, A175, doi: 10.1051/0004-6361/201832791

Barge, P., & Sommeria, J. 1995, "Did Planet Formation Begin Inside Persistent Gaseous Vortices?" *Astronomy & Astrophysics*, **395**, L1

Barnett, M. N., & Ciesla, F. J. 2022, "Thermal Processing of Solids Encountering a Young Jovian Core," *The Astrophysical Journal*, **925**, 141, doi: 10.3847/1538-4357/ac4417

Benítez-Llambay, P., & Masset, F. S. 2016, "FARGO3D: A New GPU-Oriented MHD Code," *The Astrophysical Journal Supplement Series*, **223**, 11, doi: 10.3847/0067-0049/223/1/11

Bergin, E. A. 2009, "The Chemical Evolution of Protoplanetary Disks," *arXiv:0908.3708 [astro-ph]*. http://arxiv.org/abs/0908.3708

Bergin, E. A. 2016, "Hydrocarbon Emission Rings in Protoplanetary Disks Induced by Dust Evolution," *The Astrophysical Journal*, **831**, 101

Bergin, E. A., Booth, R. A., Colmenares, M. J., & Ilee, J. D. 2024, "C/O Ratios and the Formation of Wide-separation Exoplanets," *The Astrophysical Journal Letters*, **969**, L21, doi: 10.3847/2041-8213/ad5839

Bergner, J. B., & Ciesla, F. 2021, "Ice Inheritance in Dynamical Disk Models," *The Astrophysical Journal*, **919**, 45, doi: 10.3847/1538-4357/ac0fd7

Bergner, J. B., Öberg, K. I., Bergin, E. A., et al. 2020, "An Evolutionary Study of Volatile Chemistry in Protoplanetary Disks," *The Astrophysical Journal*, **898**, 97, doi: 10.3847/1538-4357/ab9e71

Bergner, J. B., Arulanantham, N., Dartois, E., et al. 2026, "JWST Edge-on Disk Ice (JEDIce): Program Overview and Ice Survey Results," *The Astrophysical Journal*, **1002**, 17, doi: 10.3847/1538-4357/ae5961

Bergner, J. B., Öberg, K. I., Bergin, E. A., et al. 2019, "A Survey of C_2 H, HCN, and C^{18} O in Protoplanetary Disks," *The Astrophysical Journal*, **876**, 25, doi: 10.3847/1538-4357/ab141e

Bi, J., Lin, M.-K., & Dong, R. 2021, "Puffed-up Edges of Planet-opened Gaps in Protoplanetary Disks. I. Hydrodynamic Simulations," *The Astrophysical Journal*, **912**, 107, doi: 10.3847/1538-4357/abef6b

Binkert, F., Szulágyi, J., & Birnstiel, T. 2023, "Three-dimensional Dust Stirring by a Giant Planet Embedded in a Protoplanetary Disc," *Monthly Notices of the Royal Astronomical Society*, **523**, 55, doi: 10.1093/mnras/stad1405

Birnstiel, T. 2024, "Dust Growth and Evolution in Protoplanetary Disks," *Annual Review of Astronomy and Astrophysics*, **62**, 157, doi: 10.1146/annurev-astro-071221-052705

Birnstiel, T., Klahr, H., & Ercolano, B. 2012, "A Simple Model for the Evolution of the Dust Population in Protoplanetary Disks," *Astronomy & Astrophysics*, **539**, A148, doi: 10.1051/0004-6361/201118136

Birnstiel, T., Ormel, C. W., & Dullemond, C. P. 2011, "Dust Size Distributions In Coagulation/Fragmentation Equilibrium: Numerical Solutions and Analytical Fits," *Astronomy & Astrophysics*, **525**, A11, doi: 10.1051/0004-6361/201015228

Bischoff, A., & Keil, K. 1983, "Ca–Al-rich Chondrules and Inclusions in Ordinary Chondrites," *Nature*, **303**, 588, doi: 10.1038/303588a0

Bitsch, B., Izidoro, A., Johansen, A., et al. 2019, "Formation of Planetary Systems by Pebble Accretion and Migration: Growth of Gas Giants," *Astronomy & Astrophysics*, **623**, A88, doi: 10.1051/0004-6361/201834489

Bitsch, B., Morbidelli, A., Johansen, A., et al. 2018, "Pebble-isolation Mass: Scaling Law and Implications for the Formation of Super-Earths and Gas Giants," *Astronomy & Astrophysics*, **612**, A30, doi: 10.1051/0004-6361/201731931

Bizzarro, M., Johansen, A., & Dorn, C. 2025, "The Cosmochemistry of Planetary Systems," *Nature Reviews Chemistry*, doi: 10.1038/s41570-025-00711-9

Bockelée-Morvan, D., Lis, D. C., Wink, J. E., et al. 2000, "New Molecules Found in Comet C/1995 O1 (Hale-Bopp). Investigating the Link Between Cometary and Interstellar Material," *Astronomy and Astrophysics*, **353**, 1101

Boogert, A. C. A., Gerakines, P. A., & Whittet, D. C. B. 2015, "Observations of the Icy Universe.," *Annual Review of Astronomy and Astrophysics*, **53**, 541, doi: 10.1146/annurev-astro-082214-122348

Booth, R. A., Clarke, C. J., Madhusudhan, N., & Ilee, J. D. 2017, "Chemical Enrichment of Giant Planets and Discs Due to Pebble Drift," *Monthly Notices of the Royal Astronomical Society*, **469**, 3994, doi: 10.1093/mnras/stx1103

Booth, R. A., & Ilee, J. D. 2019, "Planet-forming Material in a Protoplanetary Disc: The Interplay Between Chemical Evolution and Pebble Drift," *Monthly Notices of the Royal Astronomical Society*, **487**, 3998, doi: 10.1093/mnras/stz1488

Bosman, A. D., Alarcón, F., Zhang, K., & Bergin, E. A. 2021a, "Destruction of Refractory Carbon Grains Drives the Final Stage of Protoplanetary Disk Chemistry," *The Astrophysical Journal*, **910**, 3, doi: 10.3847/1538-4357/abe127

Bosman, A. D., Cridland, A. J., & Miguel, Y. 2019, "Jupiter Formed as a Pebble Pile Around the N_2 Ice Line," *Astronomy & Astrophysics*, **632**, L11, doi: 10.1051/0004-6361/201936827

Bosman, A. D., van Dishoeck, E. F., & Walsh, C. 2018, "CO Destruction in Protoplanetary Disk Midplanes: Inside Versus Outside the CO Snow Surface," *Astronomy & Astrophysics*, **618**, A182, doi: 10.1051/0004-6361/201833497

Bosman, A. D., Alarcón, F., Bergin, E. A., et al. 2021b, "Molecules with ALMA at Planet-forming Scales (MAPS). VII. Substellar O/H and C/H and Superstellar C/O in Planet-feeding Gas," *The Astrophysical Journal Supplement Series*, **257**, 7, doi: 10.3847/1538-4365/ac1435

Boss, A. P. 1997, "Giant Planet Formation by Gravitational Instability," *Science*, **276**, 1836, doi: 10.1126/science.276.5320.1836

Boss, A. P. 2017, "The Effect of Protoplanetary Disk Cooling Times on the Formation of Gas Giant Planets by Gravitational Instability," *The Astrophysical Journal*, **836**, 53, doi: 10.3847/1538-4357/836/1/53

Boss, A. P. 2019, "The Effect of the Approach to Gas Disk Gravitational Instability on the Rapid Formation of Gas Giant Planets," *The Astrophysical Journal*, **884**, 56, doi: 10.3847/1538-4357/ab40a4

Brasser, R. 2020, "The Partitioning of the Inner and Outer Solar System by a Structured Protoplanetary Disk," *Nature Astronomy*, **4**, 12

Brennecka, G. A., Burkhardt, C., Budde, G., et al. 2020, "Astronomical Context of Solar System Formation from Molybdenum Isotopes in Meteorite Inclusions," *Science*, **370**, 837, doi: 10.1126/science.aaz8482

Bruderer, S., van Dishoeck, E. F., Doty, S. D., & Herczeg, G. J. 2012, "The Warm Gas Atmosphere of the HD 100546 Disk Seen by *Herschel*: Evidence of a Gas-rich, Carbon-poor Atmosphere?" *Astronomy & Astrophysics*, **541**, A91, doi: 10.1051/0004-6361/201118218

Bryan, M. L., Knutson, H. A., Lee, E. J., et al. 2019, "An Excess of Jupiter Analogs in Super-Earth Systems," *The Astronomical Journal*, **157**, 52, doi: 10.3847/1538-3881/aaf57f

Bryan, M. L., & Lee, E. J. 2024, "Friends Not Foes: Strong Correlation between Inner Super- Earths and Outer Gas Giants," *The Astrophysical Journal Letters*, **968**, L25, doi: 10.3847/2041-8213/ad5013

Budde, G., Burkhardt, C., Brennecka, G. A., et al. 2016, "Molybdenum Isotopic Evidence for the Origin of Chondrules and a Distinct Genetic Heritage of Carbonaceous and Non-carbonaceous Meteorites," *Earth and Planetary Science Letters*, **454**, 293, doi: 10.1016/j.epsl.2016.09.020

Calvet, N., Hartmann, L., Kenyon, S. J., & Whitney, B. A. 1994, "Flat Spectrum T Tauri Stars: The Case for Infall," *The Astrophysical Journal*, **434**, 330, doi: 10.1086/174731

Carrera, D., Simon, J. B., Li, R., Kretke, K. A., & Klahr, H. 2021, "Protoplanetary Disk Rings as Sites for Planetesimal Formation," *The Astronomical Journal*, **161**, 96, doi: 10.3847/1538-3881/abd4d9

Chachan, Y., Fortney, J. J., Ohno, K., Thorngren, D., & Murray-Clay, R. 2025, "Revising the Giant Planet Mass–Metallicity Relation: Deciphering the Formation Sequence of Giant Planets," *The Astrophysical Journal*, **994**, 43, doi: 10.3847/1538-4357/ae0cbf

Chambers, J. 2017, "Steamworlds: Atmospheric Structure and Critical Mass of Planets Accreting Icy Pebbles," *The Astrophysical Journal*, **849**, 30, doi: 10.3847/1538-4357/aa91d0

Chambers, J. 2021, "Rapid Formation of Jupiter and Wide-orbit Exoplanets in Disks with Pressure Bumps," *The Astrophysical Journal*, **914**, 102, doi: 10.3847/1538-4357/abfaa4

Chiang, E. I., & Goldreich, P. 1997, "Spectral Energy Distributions of T Tauri Stars with Passive Circumstellar Disks," *The Astrophysical Journal*, **490**, 368, doi: 10.1086/304869

Ciesla, F., & Cuzzi, J. 2006, "The Evolution of the Water Distribution in a Viscous Protoplanetary Disk," *Icarus*, **181**, 178, doi: 10.1016/j.icarus.2005.11.009

Ciesla, F. J. 2007, "Outward Transport of High-Temperature Materials Around the Midplane of the Solar Nebula," *Science*, **318**, 613, doi: 10.1126/science.1147273

Ciesla, F. J. 2010, "Residence Times of Particles in Diffusive Protoplanetary Disk Environments. I. Vertical Motions," *The Astrophysical Journal*, **723**, 514, doi: 10.1088/0004-637X/723/1/514

Ciesla, F. J. 2011, "Residence Times of Particles in Diffusive Protoplanetary Disk Environments. II. Radial Motions and Applications to Dust Annealing," *The Astrophysical Journal*, **740**, 9, doi: 10.1088/0004-637X/740/1/9

Ciesla, F. J., & Sandford, S. A. 2012, "Organic Synthesis via Irradiation and Warming of Ice Grains in the Solar Nebula," *Science*, **336**, 452, doi: 10.1126/science.1217291

Ciesla, F. J., Van Clepper, E., Bergner, J., & Bergin, E. 2026, "Oxygen Isotope Constraints on the Importance of Photochemical Processing in Protoplanetary Disks," *The Astronomical Journal*, **171**, 113, doi: 10.3847/1538-3881/ae260e

Clayton, R. N. 2002, "Self-Shielding in the Solar Nebula," *Nature*, **415**, 860, doi: 10.1038/415860b

Cleeves, L. I., Öberg, K. I., Wilner, D. J., et al. 2018, "Constraining Gas-phase Carbon, Oxygen, and Nitrogen in the IM Lup Protoplanetary Disk," *The Astrophysical Journal*, **865**, 155, doi: 10.3847/1538-4357/aade96

Connelly, J. N., Bizzarro, M., Krot, A. N., et al. 2012, "The Absolute Chronology and Thermal Processing of Solids in the Solar Protoplanetary Disk," *Science*, **338**, 651, doi: 10.1126/science.1226919

Cridland, A. J., Lega, E., & Benisty, M. 2025, "Gas Dynamics Around a Jupiter-mass Planet: II. Chemical Evolution of Circumplanetary Material," *Astronomy & Astrophysics*, **693**, A86, doi: 10.1051/0004-6361/202451140

Currie, T., Biller, B., Lagrange, A., et al. 2023, "Direct Imaging and Spectroscopy of Extrasolar Planets," in Astronomical Society of the Pacific Conference Series, Vol. 534, Protostars and Planets VII, ed. S. Inutsuka, Y. Aikawa, T. Muto, K. Tomida, & M. Tamura, 799, doi: 10.48550/arXiv.2205.05696

Cuzzi, J. N., Davis, S. S., & Dobrovolskis, A. R. 2003, "Blowing in the Wind. II. Creation and Redistribution of Refractory Inclusions in a Turbulent Protoplanetary Nebula," *Icarus*, **166**, 385, doi: 10.1016/j.icarus.2003.08.016

Cuzzi, J. N., & Zahnle, K. J. 2004, "Material Enhancement in Protoplanetary Nebulae by Particle Drift through Evaporation Fronts," *The Astrophysical Journal*, **614**, 490, doi: 10.1086/423611

Danti, C., Bitsch, B., & Mah, J. 2023, "Composition of Giant Planets: The Roles of Pebbles and Planetesimals," *Astronomy & Astrophysics*, **679**, L7, doi: 10.1051/0004-6361/202347501

Dartois, E., Dutrey, A., & Guilloteau, S. 2003, "Structure of the DM Tau Outer Disk: Probing the Verticalkinetic Temperature Gradient," *Astronomy & Astrophysics*, **399**, 773, doi: 10.1051/0004-6361:20021638

Davis, A., & Richter, F. 2007, "Condensation and Evaporation of Solar System Materials," in Treatise on Geochemistry (Elsevier), 1–31, doi: 10.1016/B0-08-043751-6/01067-7

Davis, A. M. 2022, "Short-Lived Nuclides in the Early Solar System: Abundances , Origins, and Applications," *Annual Review of Nuclear and Particle Science*, **72**, 339, doi: 10.1146/annurev-nucl-010722-074615

De Val-Borro, M., Artymowicz, P., D'Angelo, G., & Peplinski, A. 2007, "Vortex Generation in Protoplanetary Disks with an Embedded Giant Planet," *Astronomy & Astrophysics*, **471**, 1043, doi: 10.1051/0004-6361:20077169

Desch, S. J., Kalyaan, A., & Alexander, C. M. O'D. 2018, "The Effect of Jupiter's Formation on the Distribution of Refractory Elements and Inclusions in Meteorites," *The Astrophysical Journal Supplement Series*, **238**, 11, doi: 10.3847/1538-4365/aad95f

Doi, K. 2021, "Estimate on Dust Scale Height from the ALMA Dust Continuum Image of the HD 163296 Protoplanetary Disk," *The Astrophysical Journal*

Draine, B. T. 1978, "Photoelectric Heating of Interstellar Gas," *The Astrophysical Journal Supplement Series*, **36**, 595, doi: 10.1086/190513

Draine, B. T., & Bertoldi, F. 1996, "Structure of Stationary Photodissociation Fronts," *The Astrophysical Journal*, **468**, 269, doi: 10.1086/177689

Drążkowska, J., Bitsch, B., Lambrechts, M., et al. 2023, "Planet Formation Theory in the Era of ALMA and Kepler: from Pebbles to Exoplanets," in Astronomical Society of the Pacific Conference Series, Vol. 534, Protostars and Planets VII, ed. S. Inutsuka, Y. Aikawa, T. Muto, K. Tomida, & M. Tamura, 717, doi: 10.48550/arXiv.2203.09759

Drążkowska, J., & Alibert, Y. 2017, "Planetesimal Formation Starts at the Snow Line," *Astronomy & Astrophysics*, **608**, A92, doi: 10.1051/0004-6361/201731491

Drążkowska, J., Li, S., Birnstiel, T., Stammler, S. M., & Li, H. 2019, "Including Dust Coagulation in Hydrodynamic Models of Protoplanetary Disks: Dust Evolution in the Vicinity of a Jupiter-mass Planet," *The Astrophysical Journal*, **885**, 91, doi: 10.3847/1538-4357/ab46b7

Drążkowska, J., Stammler, S. M., & Birnstiel, T. 2021, "How Dust Fragmentation May Be Beneficial to Planetary Growth by Pebble Accretion," *Astronomy & Astrophysics*, **647**, A15, doi: 10.1051/0004-6361/202039925

Du, F., Bergin, E. A., & Hogerheijde, M. R. 2015, "Volatile Depletion in the TW Hydrae Disk Atmosphere," *The Astrophysical Journal*, **807**, L32, doi: 10.1088/2041-8205/807/2/L32

Duffell, P. C. 2015, "A Simple Analytical Model for Gaps in Protoplanetary Disks ," *The Astrophysical Journal*, **807**, L11, doi: 10.1088/2041-8205/807/1/L11

Duffell, P. C. 2020, "An Empirically Derived Formula for the Shape of Planet-induced Gaps in Protoplanetary Disks," *The Astrophysical Journal*, **889**, 16, doi: 10.3847/1538-4357/ab5b0f

Duffell, P. C., Haiman, Z., MacFadyen, A. I., D'Orazio, D. J., & Farris, B. D. 2014, "The Migration of Gap-Opening Planets Is Not Locked to Viscous Disk Evolution," *The Astrophysical Journal*, **792**, L10, doi: 10.1088/2041-8205/792/1/L10

Dullemond, C. P., Juhasz, A., Pohl, A., et al. 2012, RADMC-3D, https://ascl.net/1202.015

Dullemond, C. P., Birnstiel, T., Huang, J., et al. 2018, "The Disk Substructures at High Angular Resolution Project (DSHARP). VI. Dust Trapping in Thin-ringed Protoplanetary Disks," *The Astrophysical Journal Letters*, **869**, L46, doi: 10.3847/2041-8213/aaf742

Dunham, E. T., Sheikh, A., Opara, D., et al. 2023, "Calcium–aluminum-rich Inclusions in Non-carbonaceous Chondrites: Abundances, Sizes, and Mineralogy," *Meteoritics & Planetary Science*, **58**, 643, doi: 10.1111/maps.13975

Dürmann, C., & Kley, W. 2015, "Migration of Massive Planets in Accreting Disks," *Astronomy & Astrophysics*, **574**, A52, doi: 10.1051/0004-6361/201424837

E. Siciliano Rego, N. Dauphas, & T. Hopp. 2025, "Consolidating the Isotopic Trichotomy of Planetary Materials with New Evidence," *Geochemical Perspectives Letters*, **37**, 7, doi: 10.7185/geochemlet.2538

Ebert, S., Nagashima, K., Krot, A. N., et al. 2024, "Early Generation of a Refractory Inclusions-enriched H-chondritic Parent Body: A Safe Harbor For Ca, Al-rich Inclusions," *Earth and Planetary Science Letters*, **646**, 119010, doi: 10.1016/j.epsl.2024.119010

Ebert, S., Render, J., Brennecka, G. A., et al. 2018, "Ti Isotopic Evidence for a non-CAI Refractory Component in the Inner Solar System," *Earth and Planetary Science Letters*, **498**, 257, doi: 10.1016/j.epsl.2018.06.040

Eistrup, C., Walsh, C., & Van Dishoeck, E. F. 2017, "Chemical Evolution in Planet-forming Regions. Impact on Volatile Abundances and C/O Ratios of Planet-building Material," *Proceedings of the International Astronomical Union*, **13**, 69, doi: 10.1017/S1743921317009802

Eriksson, L. E. J., Johansen, A., & Liu, B. 2020, "Pebble Drift and Planetesimal Formation in Protoplanetary Discs with Embedded Planets," *Astronomy & Astrophysics*, **635**, A110, doi: 10.1051/0004-6361/201937037

Eriksson, L. E. J., Ronnet, T., Johansen, A., et al. 2022, "A Low Accretion Efficiency of Planetesimals Formed at Planetary Gap Edges," *Astronomy & Astrophysics*, **661**, A73, doi: 10.1051/0004-6361/202142391

Eriksson, L. E. J., Yang, C.-C., & Armitage, P. J. 2024, "Particle Fragmentation Inside Planet-induced Spiral Waves," *Monthly Notices of the Royal Astronomical Society: Letters*, slae110, doi: 10.1093/mnrasl/slae110

Favre, C., Cleeves, L. I., Bergin, E. A., Qi, C., & Blake, G. A. 2013, "A Significantly Low CO Abundance Toward The TW Hya Protoplanetary Disk: A Path to Active Carbon Chemistry?" *The Astrophysical Journal*, **776**, L38, doi: 10.1088/2041-8205/776/2/L38

Fayolle, E. C., Balfe, J., Loomis, R., et al. 2016, "N_2 and CO Desorption Energies from Water Ice," *The Astrophysical Journal Letters*, **816**, L28, doi: 10.3847/2041-8205/816/2/L28

Fedele, D., Tazzari, M., Booth, R., et al. 2018, "ALMA Continuum Observations Of The Protoplanetary Disk AS 209: Evidence of Multiple Gaps Opened by a Single Planet," *Astronomy & Astrophysics*, **610**, A24, doi: 10.1051/0004-6361/201731978

Flaherty, K., Hughes, A. M., Simon, J. B., et al. 2020, "Measuring Turbulent Motion in Planet-forming Disks with ALMA : A Detection around DM Tau and Nondetections around MWC 480 and V4046 Sgr," *The Astrophysical Journal*, **895**, 109, doi: 10.3847/1538-4357/ab8cc5

Flaherty, K., Hughes, A. M., Simon, J. B., et al. 2024, "Evidence for Non-zero Turbulence in the Protoplanetary Disc Around IM Lup," *Monthly Notices of the Royal Astronomical Society*, **532**, 363, doi: 10.1093/mnras/stae1480

Flaherty, K. M., Hughes, A. M., Rose, S. C., et al. 2017, "A Three-dimensional View of Turbulence: Constraints on Turbulent Motions in the HD 163296 Protoplanetary Disk Using DCO $^+$," *The Astrophysical Journal*, **843**, 150, doi: 10.3847/1538-4357/aa79f9

Flores-Rivera, L., Lambrechts, M., Gavino, S., et al. 2025, "UV Processing of Icy Pebbles in the Outer Parts of VSI-turbulent Disks," *Astronomy & Astrophysics*, **693**, A281, doi: 10.1051/0004-6361/202452933

Fung, J., & Chiang, E. 2016, "Gap Opening in 3D: Single-Planet Gaps," *The Astrophysical Journal*, **832**, 105, doi: 10.3847/0004-637X/832/2/105

Furuya, K., & Aikawa, Y. 2014, "Reprocessing of Ices in Turbulent Protoplanetary Disks: Carbon and Nitrogen Chemistry," *The Astrophysical Journal*, **790**, 97, doi: 10.1088/0004-637X/790/2/97

Furuya, K., Aikawa, Y., Nomura, H., Hersant, F., & Wakelam, V. 2013, "Water in Protoplanetary Disks: Deuteration and Turbulent Mixing," *The Astrophysical Journal*, **779**, 11, doi: 10.1088/0004-637X/779/1/11

Gerber, S., Burkhardt, C., Budde, G., Metzler, K., & Kleine, T. 2017, "Mixing and Transport of Dust in the Early Solar Nebula as Inferred from Titanium Isotope Variations among Chondrules," *The Astrophysical Journal*, **841**, L17, doi: 10.3847/2041-8213/aa72a2

Glavin, D. P., Dworkin, J. P., Alexander, C. M. O'D., et al. 2025, "Abundant Ammonia and Nitrogen-rich Soluble Organic Matter in Samples from Asteroid (101955) Bennu," *Nature Astronomy*, **9**, 199, doi: 10.1038/s41550-024-02472-9

Gurrutxaga, N., Drążkowska, J., Vaikundaraman, V., & Kleine, T. 2026, "Carbonaceous Chondrites Provide Evidence for Late-Stage Planetesimal Formation in a Pressure Bump," *The Astrophysical Journal*, **1003**, 132, doi: 10.3847/1538-4357/ae6104

Guzmán, V. V., Bergner, J. B., Law, C. J., et al. 2021, "Molecules with ALMA at Planet-forming Scales (MAPS). VI. Distribution of the Small Organics HCN, C_2 H, and H_2 CO," *The Astrophysical Journal Supplement Series*, **257**, 6, doi: 10.3847/1538-4365/ac1440

Güttler, C., Blum, J., Zsom, A., Ormel, C. W., & Dullemond, C. P. 2010, "The Outcome of Protoplanetary Dust Growth: Pebbles, Boulders, or Planetesimals?: I. Mapping the Zoo of Laboratory Collision Experiments," *Astronomy and Astrophysics*, **513**, A56, doi: 10.1051/0004-6361/200912852

Hagen, W., Allamandola, L. J., & Greenberg, J. M. 1979, "Interstellar Molecule Formation in Grain Mantles: The Laboratory Analog Experiments, Results and Implications," *Astrophysics and Space Science*, **65**, 215, doi: 10.1007/BF00643502

Haisch, Jr., K. E., Lada, E. A., & Lada, C. J. 2001, "Disk Frequencies and Lifetimes in Young Clusters," *The Astrophysical Journal*, **553**, L153, doi: 10.1086/320685

Hammer, M., Kratter, K. M., & Lin, M.-K. 2017, "Slowly-growing Gap-opening Planets Trigger Weaker Vortices," *Monthly Notices of the Royal Astronomical Society*, **466**, 3533, doi: 10.1093/mnras/stw3000

Hasegawa, T. I., Herbst, E., & Leukng, C. M. 1992, "Models of Gas-Grain Chemistry in Dense Interstellar Clouds with Complex Organic Molecules," *The Astrophysical Journal Supplement Series*, **82**, 167, doi: 10.1086/191713

Haugbølle, T., Weber, P., Wielandt, D. P., et al. 2019, "Probing the Protosolar Disk Using Dust Filtering at Gaps in the Early Solar System," *The Astronomical Journal*, **158**, 55, doi: 10.3847/1538-3881/ab1591

Helled, R., Stevenson, D. J., Lunine, J. I., et al. 2022, "Revelations on Jupiter's formation, evolution and interior: Challenges from Juno results," *Icarus*, **378**, 114937, doi: 10.1016/j.icarus.2022.114937

Henning, T., Semenov, D., St. Guilloteau, et al. 2010, "Chemistry in Disks. III. Photochemistry and X-Ray Driven Chemistry Probed by the Ethynyl Radical (CCH) in DM Tau, LkCa 15, and MWC 480," *The Astrophysical Journal*, **714**, 1511, doi: 10.1088/0004-637X/714/2/1511

Hewins, R. H., Connolly, H. C., Lofgren, G. E., & Libourel, G. 2005, "Experimental Constraints on Chondrule Formation," in Astronomical Society of the Pacific Conference Series, Vol. 341, Chondrites and the Protoplanetary Disk (Astronomical Society of the Pacific), 286

Hinton, R. W., & Bischoff, A. 1984, "Ion Microprobe Magnesium Isotope Analysis of Plagioclase and Hibonite from Ordinary Chondrites," *Nature*, **308**, 169, doi: 10.1038/308169a0

Hopp, T., Dauphas, N., Abe, Y., et al. 2022, "Ryugu's Nucleosynthetic Heritage from the Outskirts of the Solar System," *Science Advances*, **8**, eadd8141, doi: 10.1126/sciadv.add8141

Houge, A., Johansen, A., Banzatti, A., & Grant, S. 2026, "How Leaky? A Large Parameter Study of Leaky Dust Traps to Quantify the Transport of Pebbles and Ice in Protoplanetary Discs," *Astronomy & Astrophysics*, **710**, A79, doi: 10.1051/0004-6361/202659705

Hsu, C.-C., Wang, J. J., Blake, G. A., et al. 2024, "PDS 70b Shows Stellar-like Carbon-to-oxygen Ratio," *The Astrophysical Journal Letters*, **977**, L47, doi: 10.3847/2041-8213/ad95e8

Inaba, S., & Barge, P. 2006, "Dusty Vortices in Protoplanetary Disks," *The Astrophysical Journal*, **649**, 415, doi: 10.1086/506427

Izidoro, A., Dasgupta, R., Raymond, S. N., et al. 2021, "Planetesimal Rings as the Cause of the Solar System's Planetary Architecture," *Nature Astronomy*, doi: 10.1038/s41550-021-01557-z

Izquierdo, A. F., Facchini, S., Rosotti, G. P., Van Dishoeck, E. F., & Testi, L. 2022, "A New Planet Candidate Detected in a Dust Gap of the Disk around HD 163296 through Localized Kinematic Signatures: An Observational Validation of the discminer," *The Astrophysical Journal*, **928**, 2, doi: 10.3847/1538-4357/ac474d

Jiang, H., Wang, Y., Ormel, C. W., Krijt, S., & Dong, R. 2023, "Chemical Footprints of Giant Planet Formation: Role of Planet Accretion in Shaping the C/O Ratio of Protoplanetary Disks," *Astronomy & Astrophysics*, **678**, A33, doi: 10.1051/0004-6361/202346637

Johansen, A., Oishi, J. S., Low, M.-M. M., et al. 2007, "Rapid Planetesimal Formation in Turbulent Circumstellar Disks," *Nature*, **448**, 1022, doi: 10.1038/nature06086

JWST Transiting Exoplanet Community Early Release Science Team, Ahrer, E.-M., Alderson, L., et al. 2023, "Identification of Carbon Dioxide in an Exoplanet Atmosphere," *Nature*, **614**, 649, doi: 10.1038/s41586-022-05269-w

Kama, M., Bruderer, S., van Dishoeck, E. F., et al. 2016, "Volatile-carbon Locking and Release in Protoplanetary Disks: A Study of TW Hya and HD 100546," *Astronomy & Astrophysics*, **592**, A83, doi: 10.1051/0004-6361/201526991

Kamp, I., Thi, W.-F., Woitke, P., et al. 2017, "Consistent Dust and Gas Models for Protoplanetary Disks: II. Chemical Networks and Rates," *Astronomy & Astrophysics*, **607**, A41, doi: 10.1051/0004-6361/201730388

Kanagawa, K. D., Muto, T., Tanaka, H., et al. 2016, "Mass Constraint for a Planet in a Protoplanetary Disk from the Gap Width," *Publications of the Astronomical Society of Japan*, **68**

Kanagawa, K. D., Tanaka, H., Muto, T., Tanigawa, T., & Takeuchi, T. 2015, "Formation of a Disc Gap Induced by a Planet: Effect of the Deviation from Keplerian Disc Rotation," *Monthly Notices of the Royal Astronomical Society*, **448**, 994, doi: 10.1093/mnras/stv025

Kerridge, J. F. 1993, "Origins of Organic Matter in Meteorites," *Antarctic Meteorite Research*, **6**, 293

Kita, N. T., & Ushikubo, T. 2012, "Evolution of Protoplanetary Disk Inferred From^{26} Al Chronology of Individual Chondrules," *Meteoritics & Planetary Science*, **47**, 1108, doi: 10.1111/j.1945-5100.2011.01264.x

Kleine, T., Budde, G., Burkhardt, C., et al. 2020, "The Non-Carbonaceous–Carbonaceous Meteorite Dichotomy," *Space Science Reviews*, **216**, 55, doi: 10.1007/s11214-020-00675-w

Kley, W. 1999, "Mass Flow and Accretion through Gaps in Accretion Discs," *Monthly Notices of the Royal Astronomical Society*, **303**, 696, doi: 10.1046/j.1365-8711.1999.02198.x

Kley, W., D'Angelo, G., & Henning, T. 2001, "Three-dimensional Simulations of a Planet Embedded in a Protoplanetary Disk," *The Astrophysical Journal*, **547**, 457, doi: 10.1086/318345

Krapp, L., Kratter, K. M., & Youdin, A. N. 2022, "The 3D Dust and Opacity Distribution of Protoplanets in Multifluid Global Simulations," *The Astrophysical Journal*, **928**, 156, doi: 10.3847/1538-4357/ac5899

Krapp, L., Kratter, K. M., Youdin, A. N., et al. 2024, "A Thermodynamic Criterion for the Formation of Circumplanetary Disks," *The Astrophysical Journal*, **973**, 153, doi: 10.3847/1538-4357/ad644a

Kress, M. E., Tielens, A. G., & Frenklach, M. 2010, "The 'Soot Line': Destruction of Presolar Polycyclic Aromatic Hydrocarbons in the Terrestrial Planet-forming Region of Disks," *Advances in Space Research*, **46**, 44, doi: 10.1016/j.asr.2010.02.004

Krieger, A., Klahr, H., David Melon Fuksman, J., & Wolf, S. 2025, "Monte Carlo Post-processing for Radiation Hydro Simulations of Accreting Planets in Protoplanetary Disks," *Astronomy & Astrophysics*, doi: 10.1051/0004-6361/202451780

Krijt, S., Bosman, A. D., Zhang, K., et al. 2020, "CO Depletion in Protoplanetary Disks: A Unified Picture Combining Physical Sequestration and Chemical Processing," *The Astrophysical Journal*, **899**, 134, doi: 10.3847/1538-4357/aba75d

Krijt, S., & Ciesla, F. J. 2016, "Dust Diffusion and Settling in the Presence of Collisions: Trapping (sub)micron Grains in the Midplane," *The Astrophysical Journal*, **822**, 111, doi: 10.3847/0004-637X/822/2/111

Krijt, S., Ciesla, F. J., & Bergin, E. A. 2016, "Tracing Water Vapor and Ice During Dust Growth," *The Astrophysical Journal*, **833**, 285, doi: 10.3847/1538-4357/833/2/285

Krijt, S., Kama, M., McClure, M., et al. 2023, "Chemical Habitability: Supply and Retention of Life's Essential Elements During Planet Formation," in Astronomical Society of the Pacific Conference Series, Vol. 534, Protostars and Planets VII, ed. S. Inutsuka, Y. Aikawa, T. Muto, K. Tomida, & M. Tamura, 1031, doi: 10.48550/arXiv.2203.10056

Krijt, S., Schwarz, K. R., Bergin, E. A., & Ciesla, F. J. 2018, "Transport of CO in Protoplanetary Disks: Consequences of Pebble Formation, Settling, and Radial Drift," *The Astrophysical Journal*, **864**, 78, doi: 10.3847/1538-4357/aad69b

Krijt, S., Banzatti, A., Zhang, K., et al. 2025, "Cosmic Cascades: How Disk Substructure Regulates the Flow of Water to Inner Planetary Systems," *The Astrophysical Journal Letters*, **990**, L72, doi: 10.3847/2041-8213/adfbe3

Krot, A., Amelin, Y., Bland, P., et al. 2009, "Origin and Chronology of Chondritic Components: A Review," *Geochimica et Cosmochimica Acta*, **73**, 4963, doi: 10.1016/j.gca.2008.09.039

Krot, A. N., Nagashima, K., Ciesla, F. J., et al. 2010, "Oxygen Isotopic Composition of the Sun and Mean Oxygen Isotopic Composition of the Protosolar Silicate Dust: Evidence from Refractory Inclusions," *The Astrophysical Journal*, **713**, 1159, doi: 10.1088/0004-637X/713/2/1159

Kruijer, T. S., Burkhardt, C., Budde, G., & Kleine, T. 2017, "Age of Jupiter Inferred from the Distinct Genetics and Formation Times of Meteorites," *Proceedings of the National Academy of Sciences*, **114**, 6712, doi: 10.1073/pnas.1704461114

Kruijer, T. S., Kleine, T., & Borg, L. E. 2020, "The Great Isotopic Dichotomy of the Early Solar System," *Nature Astronomy*, **4**, 32, doi: 10.1038/s41550-019-0959-9

Kruijer, T. S., Touboul, M., Fischer-Gödde, M., et al. 2014, "Protracted Core Formation and Rapid Accretion of Protoplanets," *Science*, **344**, 1150, doi: 10.1126/science.1251766

Kurokawa, H., & Tanigawa, T. 2018, "Suppression of Atmospheric Recycling of Planets Embedded in a Protoplanetary Disc by Buoyancy Barrier," *Monthly Notices of the Royal Astronomical Society*, **479**, 635, doi: 10.1093/mnras/sty1498

Kurtovic, N. T., Gárate, M., Pinilla, P., et al. 2025, "The ALMA Survey of Gas Evolution of PROtoplanetary Disks (AGE-PRO). VI. Comparison of Dust Evolution Models to AGE-PRO Observations," *The Astrophysical Journal*, **989**, 6, doi: 10.3847/1538-4357/add1d0

Lambrechts, M., & Johansen, A. 2014, "Forming the Cores of Giant Planets from the Radial Pebble Flux in Protoplanetary Discs," *Astronomy & Astrophysics*, **572**, A107, doi: 10.1051/0004-6361/201424343

Lambrechts, M., Johansen, A., & Morbidelli, A. 2014, "Separating Gas-giant and Ice-giant Planets by Halting Pebble Accretion," *Astronomy & Astrophysics*, **572**, A35, doi: 10.1051/0004-6361/201423814

Lambrechts, M., Morbidelli, A., Jacobson, S. A., et al. 2019, "Formation of Planetary Systems by Pebble Accretion and Migration: How the Radial Pebble Flux Determines a Terrestrial-planet or Super- Earth Growth Mode," *Astronomy & Astrophysics*, **627**, A83, doi: 10.1051/0004-6361/201834229

Lau, T. C. H., Birnstiel, T., Drążkowska, J., & Stammler, S. M. 2024, "Sequential Giant Planet Formation Initiated by Disc Substructure," *Astronomy & Astrophysics*, **688**, A22, doi: 10.1051/0004-6361/202450464

Lau, T. C. H., Drążkowska, J., Stammler, S. M., Birnstiel, T., & Dullemond, C. P. 2022, "Rapid Formation of Massive Planetary Cores in a Pressure Bump," *Astronomy & Astrophysics*, **668**, A170, doi: 10.1051/0004-6361/202244864

Law, C. J., Loomis, R. A., Teague, R., et al. 2021, "Molecules with ALMA at Planet-forming Scales (MAPS). III. Characteristics of Radial Chemical Substructures," *The Astrophysical Journal Supplement Series*, **257**, 3, doi: 10.3847/1538-4365/ac1434

Le Bourlot, J., Pineau des Forêts, G., & Flower, D. R. 1999, “The Cooling of Astrophysical Media by H2,” *Monthly Notices of the Royal Astronomical Society*, **305**, 802, doi: 10.1046/j.1365-8711.1999.02497.x

Le Gal, R., Öberg, K. I., Teague, R., et al. 2021, “Molecules with ALMA at Planet-forming Scales (MAPS). XII. Inferring the C/O and S/H Ratios in Protoplanetary Disks with Sulfur Molecules,” *The Astrophysical Journal Supplement Series*, **257**, 12, doi: 10.3847/1538-4365/ac2583

Lee, J.-E., Bergin, E. A., & Lyons, J. R. 2008, “Oxygen Isotope Anomalies of the Sun and the Original Environment of the Solar System,” *Meteoritics & Planetary Science*, **43**, 1351, doi: 10.1111/j.1945-5100.2008.tb00702.x

Lee, J.-E., Bergin, E. A., & Nomura, H. 2010, “The Solar Nebula on Fire: A Solution to the Carbon Deficit in the Inner Solar System,” *The Astrophysical Journal*, **710**, L21, doi: 10.1088/2041-8205/710/1/L21

Lega, E., Benisty, M., Cridland, A., et al. 2024, “Gas Dynamics Around a Jupiter-mass Planet: I. Influence of Protoplanetary Disk Properties,” *Astronomy & Astrophysics*, **690**, A183, doi: 10.1051/0004-6361/202450899

Li, C., Ingersoll, A., Bolton, S., et al. 2020, “The Water Abundance in Jupiter’s Equatorial Zone,” *Nature Astronomy*, **4**, 609, doi: 10.1038/s41550-020-1009-3

Li, J., Bergin, E. A., Blake, G. A., Ciesla, F. J., & Hirschmann, M. M. 2021, “Earth’s Carbon Deficit Caused by Early Loss Through Irreversible Sublimation,” *Science Advances*, **7**, eabd3632, doi: 10.1126/sciadv.abd3632

Lichtenberg, T., Drążkowska, J., Schönbächler, M., Golabek, G., & Hands, T. 2021, “Bifurcation of Planetary Building Blocks During Solar System Formation,” *Science*, **371**, 365

Ligterink, N. F. W., Pinilla, P., Van Der Marel, N., et al. 2024, “The Rapid Formation of Macromolecules in Irradiated Ice of Protoplanetary Disk Dust Traps,” *Nature Astronomy*, doi: 10.1038/s41550-024-02334-4

Liu, B., Johansen, A., Lambrechts, M., Bizzarro, M., & Haugbølle, T. 2022, “Natural Separation of Two Primordial Planetary Reservoirs in an Expanding Solar Protoplanetary Disk,” *Science Advances*, **8**, eabm3045, doi: 10.1126/sciadv.abm3045

Liu, B., & Ormel, C. W. 2018, “Catching Drifting Pebbles: I. Enhanced Pebble Accretion Efficiencies for Eccentric Planets,” *Astronomy & Astrophysics*, **615**, A138, doi: 10.1051/0004-6361/201732307

Lothringer, J. D. 2021, “A New Window into Planet Formation and Migration: Refractory-to-Volatile Elemental Ratios in Ultra-hot Jupiters,” *The Astrophysical Journal*

Lothringer, J. D., Bennett, K. A., Sing, D. K., et al. 2025, Refractory and Volatile Species in the UV-to-IR Transmission Spectrum of Ultra-hot Jupiter WASP-178b with HST and JWST , doi: 10.3847/1538-3881/adc117

Lynden-Bell, D., & Pringle, J. E. 1974, “The Evolution of Viscous Discs and the Origin of the Nebular Variables,” *Monthly Notices of the Royal Astronomical Society*, **168**, 603, doi: 10.1093/mnras/168.3.603

Lyons, J. R., & Young, E. D. 2005, "CO Self-shielding as the Origin of Oxygen Isotope Anomalies in the Early Solar Nebula," *Nature*, **435**, 317, doi: 10.1038/nature03557

MacPherson, G., Kita, N., Ushikubo, T., Bullock, E., & Davis, A. 2012, "Well-Resolved Variations in the Formation Ages for Ca–Al-rich Inclusions in the Early Solar System," *Earth and Planetary Science Letters*, **331–332**, 43, doi: 10.1016/j.epsl.2012.03.010

MacPherson, G. J., Simon, S. B., Davis, A. M., Grossman, L., & Krot, A. N. 2005, "Calcium-aluminum-rich Inclusions: Major Unanswered Questions," in Astronomical Society of the Pacific Conference Series, Vol. 341, Chondrites and the Protoplanetary Disk, ed. A. N. Krot, E. R. D. Scott, & B. Reipurth, 225

Madhusudhan, N. 2019, "Exoplanetary Atmospheres: Key Insights, Challenges, and Prospects," *Annual Review of Astronomy and Astrophysics*, **57**, 617, doi: 10.1146/annurev-astro-081817-051846

Maeda, N., Ohtsuki, K., Suetsugu, R., et al. 2024, "Delivery of Dust Particles from Protoplanetary Disks onto Circumplanetary Disks of Giant Planets," *The Astrophysical Journal*, **968**, 62, doi: 10.3847/1538-4357/ad4035

Mamajek, E. E., Usuda, T., Tamura, M., & Ishii, M. 2009, "Initial Conditions of Planet Formation: Lifetimes of Primordial Disks," in AIP Conference Proceedings (Kailua-Kona (Hawaii): AIP), 3–10, doi: 10.1063/1.3215910

Maret, S., & Bergin, E. A. 2015, "Astrochem: Abundances of Chemical Species in the Interstellar Medium", Astrophysics Source Code Library, record ascl:1507.010. http://ascl.net/1507.010

Masset, F. 2000, "FARGO: A Fast Eulerian Transport Algorithm for Differentiallyrotating Disks," *Astronomy and Astrophysics Supplement Series*, **141**, 165, doi: 10.1051/aas:2000116

Mathis, J. S., Rumpl, W., & Nordsieck, K. H. 1977, "The Size Distribution of Interstellar Grains," *The Astrophysical Journal*, **217**, 425, doi: 10.1086/155591

Mayor, M., & Queloz, D. 1995, "A Jupiter-mass Companion to a Solar-Type Star," *Nature*, **378**, 355, doi: 10.1038/378355a0

McElroy, D., Walsh, C., Markwick, A. J., et al. 2013, "The UMIST Database for Astrochemistry 2012," *Astronomy & Astrophysics*, **550**, A36, doi: 10.1051/0004-6361/201220465

McKeegan, K. D., Kallio, A. P. A., Heber, V. S., et al. 2011, "The Oxygen Isotopic Composition of the Sun Inferred from Captured Solar Wind," *Science*, **332**, 1528, doi: 10.1126/science.1204636

Meijerink, R., Pontoppidan, K. M., Blake, G. A., Poelman, D. R., & Dullemond, C. P. 2009, "Radiative Transfer Models of Mid-Infrared H_2 O Lines in the Planet-Forming Region of Circumstellar Disks," *The Astrophysical Journal*, **704**, 1471, doi: 10.1088/0004-637X/704/2/1471

Miotello, A., Van Dishoeck, E. F., Williams, J. P., et al. 2017, "Lupus Disks with Faint CO Isotopologues: Low Gas/Dust or High Carbon Depletion?" *Astronomy & Astrophysics*, **599**, A113, doi: 10.1051/0004-6361/201629556

Miotello, A., Facchini, S., Van Dishoeck, E. F., et al. 2019, "Bright C_2 H Emission in Protoplanetary Discs in Lupus: High Volatile C/O > 1 Ratios," *Astronomy & Astrophysics*, **631**, A69, doi: 10.1051/0004-6361/201935441

Misener, W., Krijt, S., & Ciesla, F. J. 2019, "Tracking Dust Grains during Transport and Growth in Protoplanetary Disks," *The Astrophysical Journal*, **885**, 118, doi: 10.3847/1538-4357/ab4a13

Monga, N., & Desch, S. 2014, "External Photoevaporation of the Solar Nebula: Jupiter's Noble Gas Enrichments," *The Astrophysical Journal*, **798**, 9, doi: 10.1088/0004-637X/798/1/9

Morbidelli, A., Baillié, K., Batygin, K., et al. 2021, "Contemporary Formation of Early Solar System Planetesimals at Two Distinct Radial Locations," *Nature Astronomy*, **6**, 72, doi: 10.1038/s41550-021-01517-7

Morbidelli, A., Batygin, K., & Lega, E. 2023, "In Situ Enrichment in Heavy Elements of Hot Jupiters," *Astronomy & Astrophysics*, **675**, A75, doi: 10.1051/0004-6361/202346868

Morbidelli, A., Szulágyi, J., Crida, A., et al. 2014, "Meridional Circulation of Gas into Gaps Opened by Giant Planets in Three-dimensional Low-viscosity Disks," *Icarus*, **232**, 266, doi: 10.1016/j.icarus.2014.01.010

Mousis, O., Ronnet, T., & Lunine, J. I. 2019, "Jupiter's Formation in the Vicinity of the Amorphous Ice Snowline," *The Astrophysical Journal*, **875**, 9, doi: 10.3847/1538-4357/ab0a72

Muñoz Caro, G. M., Meierhenrich, U. J., Schutte, W. A., et al. 2002, "Amino Acids from Ultraviolet Irradiation of Interstellar Ice Analogues," *Nature*, **416**, 403, doi: 10.1038/416403a

Mulders, G. D., Drążkowska, J., Van Der Marel, N., Ciesla, F. J., & Pascucci, I. 2021, "Why Do M Dwarfs Have More Transiting Planets?" *The Astrophysical Journal Letters*, **920**, L1, doi: 10.3847/2041-8213/ac2947

Nanne, J. A., Nimmo, F., Cuzzi, J. N., & Kleine, T. 2019, "Origin of the Non-carbonaceous–carbonaceous Meteorite Dichotomy," *Earth and Planetary Science Letters*, **511**, 44, doi: 10.1016/j.epsl.2019.01.027

Naraoka, H., Takano, Y., Dworkin, J. P., et al. 2023, "Soluble Organic Molecules in Samples of the Carbonaceous Asteroid (162173) Ryugu," *Science*, **379**, eabn9033, doi: 10.1126/science.abn9033

Nasedkin, E., Mollière, P., Lacour, S., et al. 2024, "Four-of-a-kind? Comprehensive Atmospheric Characterisation of the HR 8799 Planets with VLTI/GRAVITY," *Astronomy & Astrophysics*, **687**, A298, doi: 10.1051/0004-6361/202449328

Nesvorný, D., Dauphas, N., Vokrouhlický, D., Deienno, R., & Hopp, T. 2024, "Isotopic Trichotomy of Main Belt Asteroids from Implantation of Outer Solar System Planetesimals," *Earth and Planetary Science Letters*, **626**, 118521, doi: 10.1016/j.epsl.2023.118521

Nomura, H., Aikawa, Y., Tsujimoto, M., Nakagawa, Y., & Millar, T. J. 2007, "Molecular Hydrogen Emission from Protoplanetary Disks. II. Effects of X-Ray Irradiation and Dust Evolution," *The Astrophysical Journal*, **661**, 334, doi: 10.1086/513419

Öberg, K. I., Facchini, S., & Anderson, D. E. 2023, "Protoplanetary Disk Chemistry," *Annual Review of Astronomy and Astrophysics*, **61**, 287, doi: 10.1146/annurev-astro-022823-040820

Ormel, C. W., & Liu, B. 2018, "Catching Drifting Pebbles: II. A Stochastic Equation of Motion for Pebbles," *Astronomy & Astrophysics*, **615**, A178, doi: 10.1051/0004-6361/201732562

Paneque-Carreño, T., Izquierdo, A. F., Teague, R., et al. 2024, "High Turbulence in the IM Lup Protoplanetary Disk: Direct Observational Constraints from CN and C_2H Emission," *Astronomy & Astrophysics*, **684**, A174, doi: 10.1051/0004-6361/202347757

Pascucci, I., Beck, T. L., Cabrit, S., et al. 2025, "The Nested Morphology of Disk Winds from Young Stars Revealed by JWST/NIRSpec Observations," *Nature Astronomy*, **9**, 81, doi: 10.1038/s41550-024-02385-7

Perotti, G., Christiaens, V., Henning, T., et al. 2023, "Water in the Terrestrial Planet-forming Zone of the PDS 70 Disk," *Nature*, **620**, 516, doi: 10.1038/s41586-023-06317-9

Petrovic, H. J., Booth, R. A., & Clarke, C. J. 2024, "Material Transport in Protoplanetary Discs with Massive Embedded Planets," *Monthly Notices of the Royal Astronomical Society*, **534**, 2412, doi: 10.1093/mnras/stae2229

Petrovic, H. J., Booth, R. A., & Clarke, C. J. 2024, "Material Transport in Protoplanetary Discs with Massive Embedded Planets," *Monthly Notices of the Royal Astronomical Society*, **534**, 2412, doi: 10.1093/mnras/stae2229

Pinilla, P., Benisty, M., & Birnstiel, T. 2012, "Ring Shaped Dust Accumulation in Transition Disks," *Astronomy & Astrophysics*, **545**, A81, doi: 10.1051/0004-6361/201219315

Pinte, C., Price, D. J., Ménard, F., et al. 2018, "Kinematic Evidence for an Embedded Protoplanet in a Circumstellar Disk," *The Astrophysical Journal*, **860**, L13, doi: 10.3847/2041-8213/aac6dc

Pinte, C., van der Plas, G., Ménard, F., et al. 2019, "Kinematic Detection of a Planet Carving a Gap in a Protoplanetary Disk," *Nature Astronomy*, **3**, 1109, doi: 10.1038/s41550-019-0852-6

Pollack, J. B., Hubickyj, O., Bodenheimer, P., et al. 1996, "Formation of the Giant Planets by Concurrent Accretion of Solids and Gas," *Icarus*, **124**, 62, doi: 10.1006/icar.1996.0190

Price, E. M., Van Clepper, E., & Ciesla, F. J. 2025, "Dynamics of Small, Constant-size Particles in a Protoplanetary Disk with an Embedded Protoplanet," *The Astrophysical Journal*, **979**, 37, doi: 10.3847/1538-4357/ad9f35

Pérez, S., Casassus, S., Baruteau, C., et al. 2019, "Dust Unveils the Formation of a Mini-Neptune Planet in a Protoplanetary Ring," *The Astronomical Journal*, **158**, 15, doi: 10.3847/1538-3881/ab1f88

Rafikov, R. R. 2002, "Planet Migration and Gap Formation by Tidally Induced Shocks," *The Astrophysical Journal*, **572**, 566, doi: 10.1086/340228

Rafikov, R. R. 2005, "Can Giant Planets Form by Direct Gravitational Instability?" *The Astrophysical Journal*, **621**, L69, doi: 10.1086/428899

Raymond, S. N., & Izidoro, A. 2017, "Origin of Water in the Inner Solar System: Planetesimals Scattered Inward during Jupiter and Saturn's Rapid Gas Accretion," *Icarus*, **297**, 134, doi: 10.1016/j.icarus.2017.06.030

Reboussin, L., Wakelam, V., Guilloteau, S., Hersant, F., & Dutrey, A. 2015, "Chemistry in Protoplanetary Disks: The Gas-phase CO/H $_2$ Ratio and the Carbon Reservoir," *Astronomy & Astrophysics*, **579**, A82, doi: 10.1051/0004-6361/201525885

Sakamoto, N., Seto, Y., Itoh, S., et al. 2007, "Remnants of the Early Solar System Water Enriched in Heavy Oxygen Isotopes," *Science*, **317**, 231, doi: 10.1126/science.1142021

Sarver, C. C., Walker, C. E., & Widicus Weaver , S. L. 2026, "Laboratory Investigation of Simultaneous Ultraviolet Photoprocessing and Temperature-Programmed Desorption of Interstellar Ice Analogs," *ACS Earth and Space Chemistry*, **10**, 536, doi: 10.1021/acsearthspacechem.5c00338

Schneider, A. D., & Bitsch, B. 2021a, "How Drifting and Evaporating Pebbles Shape Giant Planets: I. Heavy Element Content and Atmospheric C/O," *Astronomy & Astrophysics*, **654**, A71, doi: 10.1051/0004-6361/202039640

Schneider, A. D., & Bitsch, B. 2021b, "How Drifting and Evaporating Pebbles Shape Giant Planets: II. Volatiles and Refractories in Atmospheres," *Astronomy & Astrophysics*, **654**, A72, doi: 10.1051/0004-6361/202141096

Schrader, D. L., & Davidson, J. 2022, "Prolonged Early Migration of Dust from the Inner Solar System to the Comet-forming Region," *Earth and Planetary Science Letters*, **589**, 117552, doi: 10.1016/j.epsl.2022.117552

Schrader, D. L., Nagashima, K., Davidson, J., et al. 2020, "Outward Migration of Chondrule Fragments in the Early Solar System : O-isotopic Evidence for Rocky Material Crossing the Jupiter Gap?" *Geochimica et Cosmochimica Acta*, **282**, 133, doi: 10.1016/j.gca.2020.05.014

Schwarz, K. R., Bergin, E. A., Cleeves, L. I., et al. 2016, "The Radial Distribution of H2 and CO in TW Hya as Revealed by Resolved ALMA Observations of CO Isotopologues," *The Astrophysical Journal*, **823**, 91, doi: 10.3847/0004-637X/823/2/91

Schwarz, K. R., Bergin, E. A., Cleeves, L. I., et al. 2018, "Unlocking CO Depletion in Protoplanetary Disks. I. The Warm Molecular Layer," *The Astrophysical Journal*, **856**, 85, doi: 10.3847/1538-4357/aaae08

Semenov, D., & Wiebe, D. 2011, "Chemical Evolution of Turbulent Protoplanetary Disks and the Solar Nebula," *The Astrophysical Journal Supplement Series*, **196**, 25, doi: 10.1088/0067-0049/196/2/25

Shakura, N. I., & Sunyaev, R. A. 1973, "Black Holes in Binary Systems. Observational Appearance.," *Astronomy and Astrophysics*, **24**, 337. https://ui.adsabs.harvard.edu/abs/1973A&A....24..337S

Shibata, S., & Helled, R. 2022, "Enrichment of Jupiter's Atmosphere by Late Planetesimal Bombardment," *The Astrophysical Journal Letters*, **926**, L37, doi: 10.3847/2041-8213/ac54b1

Shibata, S., Helled, R., & Ikoma, M. 2020, "The Origin of the High Metallicity of Close-in Giant Exoplanets: Combined Effects of Resonant and Aerodynamic Shepherding," *Astronomy & Astrophysics*, **633**, A33, doi: 10.1051/0004-6361/201936700

Shibata, S., Helled, R., & Ikoma, M. 2022, "The Origin of the High Metallicity of Close-in Giant Exoplanets: II . The Nature of the Sweet Spot for Accretion," *Astronomy & Astrophysics*, **659**, A28, doi: 10.1051/0004-6361/202142180

Sierra, A., Benisty, M., Pinilla, P., et al. 2025, "Leaky Dust Trap in the PDS 70 Disc Revealed by ALMA Band 9 Observations," *Monthly Notices of the Royal Astronomical Society*, **541**, 3101, doi: 10.1093/mnras/staf1164

Stammler, S. M., & Birnstiel, T. 2022, "DustPy: A Python Package for Dust Evolution in Protoplanetary Disks," *The Astrophysical Journal*, **935**, 35, doi: 10.3847/1538-4357/ac7d58

Stammler, S. M., Lichtenberg, T., Drążkowska, J., & Birnstiel, T. 2023, "Leaky Dust Traps: How Fragmentation Impacts Dust Filtering By Planets," *Astronomy & Astrophysics*, **670**, L5, doi: 10.1051/0004-6361/202245512

Szulágyi, J., Binkert, F., & Surville, C. 2022, "Meridional Circulation of Dust and Gas in the Circumstellar Disk: Delivery of Solids onto the Circumplanetary Region," *The Astrophysical Journal*, **924**, 1, doi: 10.3847/1538-4357/ac32d1

Szulágyi, J., Masset, F., Lega, E., et al. 2016, "Circumplanetary Disc or Circumplanetary Envelope?" *Monthly Notices of the Royal Astronomical Society*, **460**, 2853, doi: 10.1093/mnras/stw1160

Szulágyi, J., Morbidelli, A., Crida, A., & Masset, F. 2014, "Accretion of Jupiter-Mass Planets in the Limit of Vanishing Viscosity," *The Astrophysical Journal*, **782**, 65, doi: 10.1088/0004-637X/782/2/65

Tabone, B., Rosotti, G. P., Trapman, L., et al. 2025, "The ALMA Survey of Gas Evolution of PROtoplanetary Disks (AGE-PRO). VII. Testing Accretion Mechanisms from Disk Population Synthesis," *The Astrophysical Journal*, **989**, 7, doi: 10.3847/1538-4357/adc7b1

Tachibana, S., Sawada, H., Okazaki, R., et al. 2022, "Pebbles and Sand on Asteroid (162173) Ryugu: In Situ Observation and Particles Returned to Earth," *Science*, **375**, 1011, doi: 10.1126/science.abj8624

Takeuchi, T., & Lin, D. N. C. 2002, "Radial Flow of Dust Particles in Accretion Disks," *The Astrophysical Journal*, **581**, 1344, doi: 10.1086/344437

Takeuchi, T., Miyama, S. M., & Lin, D. N. C. 1996, "Gap Formation in Protoplanetary Disks," *The Astrophysical Journal*, **460**, 832, doi: 10.1086/177013

Tanigawa, T., Maruta, A., & Machida, M. N. 2014, "Accretion of Solid Materials Onto Circumplanetary Disks from Protoplanetary Disks," *The Astrophysical Journal*, **784**, 109, doi: 10.1088/0004-637X/784/2/109

Teague, R., Bae, J., & Bergin, E. A. 2019, "Meridional Flows in the Disk Around a Young Star," *Nature*, **574**, 378, doi: 10.1038/s41586-019-1642-0

Teague, R., Bae, J., Bergin, E. A., Birnstiel, T., & Foreman-Mackey, D. 2018a, "A Kinematical Detection of Two Embedded Jupiter-mass Planets in HD 163296," *The Astrophysical Journal*, **860**, L12, doi: 10.3847/2041-8213/aac6d7

Teague, R., Henning, T., Guilloteau, S., et al. 2018b, "Temperature, Mass, and Turbulence: A Spatially Resolved Multiband Non-LTE Analysis of CS in TW Hya," *The Astrophysical Journal*, **864**, 133, doi: 10.3847/1538-4357/aad80e

Teague, R., Benisty, M., Facchini, S., et al. 2025, "exoALMA. I. Science Goals, Project Design, and Data Products," *The Astrophysical Journal Letters*, **984**, L6, doi: 10.3847/2041-8213/adc43b

Tenelanda-Osorio, L. I., Bouquet, A., Javelle, T., et al. 2022, "Effect of the UV Dose on the Formation of Complex Organic Molecules in Astrophysical Ices: Irradiation of Methanol Ices at 20 K and 80 K," *Monthly Notices of the Royal Astronomical Society*, **515**, 5009, doi: 10.1093/mnras/stac1932

Thorngren, D. P., Fortney, J. J., Murray-Clay, R. A., & Lopez, E. D. 2016, "The Mass–Metallicity Relation for Giant Planets," *The Astrophysical Journal*, **831**, 64, doi: 10.3847/0004-637X/831/1/64

Toomre, A. 1964, "On the Gravitational Stability of a Disk of Stars," *The Astrophysical Journal*, **139**, 1217, doi: 10.1086/147861

Van Clepper, E. R., Alarcón, F., Bergin, E., & Ciesla, F. J. 2025a, "Dust Recycling and Icy Volatile Enhancement (DRIVE): A Novel Method of Volatile Enrichment in Cold Giant Planets," *The Astrophysical Journal Letters*, **994**, L44, doi: 10.3847/2041-8213/ae1d81

Van Clepper, E. R., Bergner, J. B., Bosman, A. D., Bergin, E., & Ciesla, F. J. 2022, "Chemical Feedback of Pebble Growth: Impacts on CO depletion and C/O ratios," *The Astrophysical Journal*, **927**, 206, doi: 10.3847/1538-4357/ac511b

Van Clepper, E. R., Price, E., & Ciesla, F. J. 2025b, "Three-dimensional Transport of Solids in a Protoplanetary Disk Containing a Growing Giant Planet," *The Astrophysical Journal*, **980**, 201, doi: 10.3847/1538-4357/ada8a4

van der Marel, N., Booth, A. S., Leemker, M., Van Dishoeck, E. F., & Ohashi, S. 2021, "A Major Asymmetric Ice Trap in a Planet-forming Disk: I. Formaldehyde and Methanol," *Astronomy & Astrophysics*, **651**, L5, doi: 10.1051/0004-6361/202141051

van der Marel, N., Ligterink, N. F. W., van der Werf, R., et al. 2026, "Observational Evidence for a Possible Link Between PAH Emission and Dust Trap Locations in Protoplanetary Disks," *Astronomy & Astrophysics*, **706**, A214, doi: 10.1051/0004-6361/202453113

Van Kooten, E., Schiller, M., Moynier, F., et al. 2021, "Hybrid Accretion of Carbonaceous Chondrites by Radial Transport across the Jupiter Barrier," *The Astrophysical Journal*, **910**, 70, doi: 10.3847/1538-4357/abd9c8

Van 'T Hoff, M. L. R., Tobin, J. J., Li, Z.-Y., et al. 2023, "Early Planet Formation in Embedded Disks (eDisk). III. A First High-resolution View of Submillimeter Continuum and Molecular Line Emission toward the Class 0 Protostar L1527 IRS," *The Astrophysical Journal*, **951**, 10, doi: 10.3847/1538-4357/accf87

Villenave, M., Rosotti, G. P., Lambrechts, M., et al. 2025, "Turbulence in Protoplanetary Disks: A Systematic Analysis of Dust Settling in 33 Disks," *Astronomy & Astrophysics*, **697**, A64, doi: 10.1051/0004-6361/202553822

Visser, R., Bruderer, S., Cazzoletti, P., et al. 2018, "Nitrogen Isotope Fractionation in Protoplanetary Disks," *Astronomy & Astrophysics*, **615**, A75, doi: 10.1051/0004-6361/201731898

Visser, R., Doty, S. D., & van Dishoeck, E. F. 2011, "The Chemical History of Molecules in Circumstellar Disks: II. Gas-phase Species," *Astronomy & Astrophysics*, **534**, A132, doi: 10.1051/0004-6361/201117249

Visser, R., van Dishoeck, E. F., & Black, J. H. 2009, "The Photodissociation and Chemistry of CO Isotopologues: Applications to Interstellar Clouds and Circumstellar Disks," *Astronomy & Astrophysics*, **503**, 323, doi: 10.1051/0004-6361/200912129

Walsh, C., Nomura, H., & van Dishoeck, E. 2015, "The Molecular Composition of the Planet-forming Regions of Protoplanetary Disks Across the Luminosity Regime," *Astronomy & Astrophysics*, **582**, A88, doi: 10.1051/0004-6361/201526751

Walsh, K. J., Morbidelli, A., Raymond, S. N., O'Brien, D. P., & Mandell, A. M. 2012, "Populating the Asteroid Belt from Two Parent Source Regions Due to the Migration of Giant Planets-"The Grand Tack"," *Meteoritics & Planetary Science*, **47**, 1941, doi: 10.1111/j.1945-5100.2012.01418.x

Wang, Y., Ormel, C. W., Huang, P., & Kuiper, R. 2023, "Atmospheric Recycling of Volatiles by Pebble-accreting Planets," *Monthly Notices of the Royal Astronomical Society*, **523**, doi: 10.1093/mnras/stad1753

Warren, P. H. 2011, "Stable-isotopic Anomalies and the Accretionary Assemblage of the Earth and Mars: A Subordinate Role for Carbonaceous Chondrites," *Earth and Planetary Science Letters*, **311**, 93, doi: 10.1016/j.epsl.2011.08.047

Weber, P., Benítez-Llambay, P., Gressel, O., Krapp, L., & Pessah, M. E. 2018, "Characterizing the Variable Dust Permeability of Planet-induced Gaps," *The Astrophysical Journal*, **854**, 153, doi: 10.3847/1538-4357/aaab63

Weidenschilling, S. J. 1977, "Aerodynamics of Solid Bodies in the Solar Nebula," *Monthly Notices of the Royal Astronomical Society*, **180**, 57, doi: 10.1093/mnras/180.2.57

Wolszczan, A., & Frail, D. A. 1992, "A Planetary System Around the Millisecond Pulsar PSR1257 + 12," *Nature*, **355**, 145, doi: 10.1038/355145a0

Xuan, J. W., Ruffio, J.-B., Chachan, Y., et al. 2026, "The Compositions of the HR 8799 Planets Reflect Accretion of Both Solids and Metal-enriched Gas," *The Astrophysical Journal*, **1000**, 27, doi: 10.3847/1538-4357/ae448f

Yang, L., & Ciesla, F. J. 2012, "The Effects of Disk Building on the Distributions of Refractory Materials in the Solar Nebula: Refractory Objects Transport in the Solar Nebula," *Meteoritics & Planetary Science*, **47**, 99, doi: 10.1111/j.1945-5100.2011.01315.x

Yokoyama, T., Nagashima, K., Nakai, I., et al. 2023, "Samples Returned from the Asteroid Ryugu are Similar to Ivuna-type Carbonaceous Meteorites," *Science*, **379**, eabn7850, doi: 10.1126/science.abn7850

Youdin, A. N., & Goodman, J. 2005, "Streaming Instabilities in Protoplanetary Disks," *The Astrophysical Journal*, **620**, 459, doi: 10.1086/426895

Youdin, A. N., & Lithwick, Y. 2007, "Particle Stirring in Turbulent Gas Disks: Including Orbital Oscillations," *Icarus*, **192**, 588, doi: 10.1016/j.icarus.2007.07.012

Yurimoto, H., & Kuramoto, K. 2004, "Molecular Cloud Origin for the Oxygen Isotope Heterogeneity in the Solar System," *Science*, **305**, 1763, doi: 10.1126/science.1100989

Zhang, K., Bergin, E. A., Schwarz, K., Krijt, S., & Ciesla, F. 2019, "Systematic Variations of CO Gas Abundance with Radius in Gas-rich Protoplanetary Disks," *The Astrophysical Journal*, **883**, 98, doi: 10.3847/1538-4357/ab38b9

Zhang, K., Bosman, A. D., & Bergin, E. A. 2020, "Excess C/H in Protoplanetary Disk Gas from Icy Pebble Drift Across the CO Snowline," *The Astrophysical Journal Letters*, **891**, L16, doi: 10.3847/2041-8213/ab77ca

Zhang, K., Booth, A. S., Law, C. J., et al. 2021, "Molecules with ALMA at Planet-forming Scales (MAPS). V. CO Gas Distributions," *The Astrophysical Journal Supplement Series*, **257**, 5, doi: 10.3847/1538-4365/ac1580

Zhao, H., Lau, T. C. H., Birnstiel, T., Stammler, S. M., & Drążkowska, J. 2025, "Planetesimal Formation in a Pressure Bump Induced by Infall," *Astronomy & Astrophysics*, **694**, A205, doi: 10.1051/0004-6361/202452941

Zhu, W., & Wu, Y. 2018, "The Super Earth–Cold Jupiter Relations," *The Astronomical Journal*, **156**, 92, doi: 10.3847/1538-3881/aad22a

Zhu, Z., Stone, J. M., Rafikov, R. R., & Bai, X.-n. 2014, "Particle Concentration at Planet-Induced Gap Edges and Vortices. I. Inviscid Three-Dimensional Hydro Disks," *The Astrophysical Journal*, **785**, 122, doi: 10.1088/0004-637X/785/2/122

Zolensky, M. E., Zega, T. J., Yano, H., et al. 2006, "Mineralogy and Petrology of Comet 81P/Wild 2 Nucleus Samples," *Science*, **314**, 1735, doi: 10.1126/science.1135842

Zsom, A., Ormel, C. W., Güttler, C., Blum, J., & Dullemond, C. P. 2010, "The Outcome of Protoplanetary Dust Growth: Pebbles, Boulders, or Planetesimals?: II. Introducing the Bouncing Barrier," *Astronomy and Astrophysics*, **513**, A57, doi: 10.1051/0004-6361/200912976

Öberg, K. I., & Bergin, E. A. 2016, "Excess C/O and C/H in Outer Protoplanetary Disk Gas," *The Astrophysical Journal Letters*, **831**, L19, doi: 10.3847/2041-8205/831/2/L19

Öberg, K. I., Murray-Clay, R., & Bergin, E. A. 2011, "The Effects of Snowlines on C/O in Planetary Atmospheres," *The Astrophysical Journal*, **743**, L16, doi: 10.1088/2041-8205/743/1/L16

Öberg, K. I., & Wordsworth, R. 2019, "Jupiter's Composition Suggests its Core Assembled Exterior to the N_2 Snowline," *The Astronomical Journal*, **158**, 194, doi: 10.3847/1538-3881/ab46a8

Öberg, K. I., Guzmán, V. V., Walsh, C., et al. 2021, "Molecules with ALMA at Planet-forming Scales (MAPS). I. Program Overview and Highlights," *The Astrophysical Journal Supplement Series*, **257**, 1, doi: 10.3847/1538-4365/ac1432